Growth of semi-polar GaN on high index silicon (11h) substrates by metal organic vapor phase epitaxy

Dissertation

zur Erlangung des akademischen Grades

**doctor rerum naturalium
(Dr. rer. nat.)**

genehmigt durch die Fakultät für Naturwissenschaften
der Otto-von-Guericke-Universität Magdeburg

von   Dipl.-Phys. Roghaiyeh Ravash

geb. am 01.09.1975 in Oromiyeh (Iran)

Gutachter   apl. Prof. Dr. Armin Dadgar

Prof. Dr. Ferdinand Scholz

eingereicht am: 24.09.2013

verteidigt am: 13.02.2014

"Life is like riding a bicycle. To keep your balance you must keep moving."

A. Einstein

Abstract

Due to the lack of cheap and large diameter GaN substrates, GaN based devices are usually deposited on heterosubstrates such as sapphire or SiC. These substrates are expensive, and unavailable in diameters above 150 mm. Here Si substrates are a promising alternative to growing GaN structures because of their properties, e.g. low price, availability in large diameters, and high thermal and electrical conductivity.

Up to now, the growth orientation of GaN-based devices is mostly parallel to the c-axis. In wurtzite group-III-nitrides, polarization fields along the c-axis direction reduce the quantum efficiency of optoelectronic devices due to the quantum confined Stark effect (QCSE). Non- or semi-polar growth of GaN structures is a well-known method of avoiding or reducing the polarization field in growth direction. There are several approaches to growing non-c-axis GaN, for example selective area growth technology, which requires several processing steps before metal organic vapor phase epitaxy (MOVPE) growth.

The goal of this thesis was the investigation of the growth and properties of semi-polar GaN structures grown by MOVPE on high index Si substrates to unify a low cost substrate with the beneficial properties of semi-polar layers for light emitters.

Semi-polar GaN deposition was done on different high index silicon substrates, e.g. Si(410) and Si(11h), whereby h=1, 3,...,7. The structure of the Si(11h) surface if h=2, 3,...,7 has a stepped character combined from Si(001) and Si(111) as terrace and step structures. The ratio of these Si(111)/Si(001) terraces and steps depends on the h value and increases from Si(117) towards Si(112).

Experimental results of the impact of AlN seeding layer growth parameters on the GaN crystal orientation depending on different Si surface directions are presented in this work. It was observed that GaN layers can be grown with their different c-axis inclination with respect to the substrate surface normal vector by tuning the AlN seeding layer growth parameters. It was found that a low temperature (LT) (680 °C) AlN seeding layer is required to obtain semi-polar GaN layers, because the high temperature AlN seeding layer results in a c-axis oriented GaN structure. If GaN layers are grown on Si(11h) with h>3, GaN c-axis tilt angles and the number of different crystalline orientations increase when the LT-AlN seeding layer thickness increases. A thick LT-AlN seeding layer leads to the growth of polycrystalline GaN structures high index silicon.

This work presents the first semi-polar growth of single component GaN layers on non-patterned Si(11h), whereby h=2, 3, ...,6, with a thin LT-AlN seeding layer.

It was also found that LT-AlN interlayers are beneficial in reducing or even eliminating basal plane stacking faults of semi-polar GaN layers grown on Si(112) and Si(113).

Finally, semi-polar GaN/InGaN LEDs structures were grown on optimized GaN buffer layers on Si(112) and Si(113).

Abstract (in German)

Aufgrund der fehlenden Verfügbarkeit von kostengünstigen, großflächigen GaN-Substraten werden GaN-basierte Bauelementschichten in der Regel auf Fremdsubstraten wie Saphir und Siliziumkarbid abgeschieden. Diese Substrate sind sehr teuer und nicht in Durchmessern größer als 150 mm verfügbar. Hier bieten Siliziumsubstrate aufgrund ihrer Eigenschaften eine vielversprechende Alternative für das Wachstum von GaN-Strukturen. Dies sind unter anderem die Verfügbarkeit von Wafern in großen Durchmessern zu einem geringen Preis und die hohe thermische und elektrische Leitfähigkeit.

Bisher ist die übliche Wachstumsrichtung von GaN-basierten Bauelementen parallel zur c-Richtung. In wurzitartigen Gruppe-III-Nitriden reduzieren Polarisationsfelder entlang der c-Achse die Leuchteffizienz (Quanteneffizienz) von optoelektronischen Bauelementen aufgrund des QCSE (Quantum Confined Stark Effect). Die Semi- oder un-polare Epitaxie von GaN-Strukturen ist ein Weg zur Unterbindung oder Reduzierung von Polarisationsfeldern in Wachstumsrichtung. Es gibt mehrere Ansätze für das Abscheiden von nicht c-achsenorientiertem GaN, zum Beispiel örtlich selektive Epitaxieverfahren, welche mehrere Prozessierschritte vor der metallorganischen Gasphasenepitaxie (MOVPE) erfordern.

Das Ziel dieser Arbeit war die Untersuchung des semi-polaren Wachstums und der Eigenschaften von Galliumnitrid (GaN) auf hochindizierten Siliziumsubstraten mittels MOVPE.

Semipolares Galliumnitrid wurde auf verschiedenen hochindizierten Si-Substraten wie z.B. Si (410) und Si(11h) mit h=1, 3,...,7 abgeschieden. Die Oberflächen-Struktur von Si(11h) mit h=2, 3,...,7 ist stufenförmig und setzt sich aus Si(001) und Si(111) Terrassen und Stufen zusammen. Das Verhältnis zwischen den Si(111)/Si(001) Stufen und Terrassen ist abhängig vom h-Wert und steigt von Si(117) zu Si(112).

Die experimentellen Ergebnisse des Einflusses der Wachstumsbedingungen der AlN-Keimschicht auf die Orientierung der nachfolgenden GaN-Schicht in Abhängigkeit von der Siliziumoberflächenorientierung werden in dieser Arbeit präsentiert. Es wurde festgestellt, dass GaN-Schichten mit unterschiedlichem c-Achsenkippwinkel in Bezug auf die Oberflächennormale des Substrates durch Variation der Einstellungen für die Abscheidung der AlN-Keimschicht hergestellt werden können. Es zeigte sich, dass diese Schicht bei einer niedrigen Temperatur (LT-AlN) (680 °C) gewachsen werden muss, um semi-polare GaN-Schichten zu erhalten. Höhere Temperaturwerte führen zu c-achsenorientierten GaN-Strukturen. Des Weiteren steigen der c-Achsen-Kippwinkel und die Anzahl anders

orientierter Kristallkomponenten von GaN Strukturen mit zunehmender LT-AlN-Keimschichtdicke, wenn GaN Schichten auf Si(11h) mit h>3 gewachsen werden. Eine dicke LT-AlN-Keimschicht führt daher zum Wachstum von polykristallinen Schichten auf hochindizierten Si-Substraten.

Darüber hinaus wird erstmalig das Wachstum von semi-polaren, Einzelkomponenten GaN Schichten auf nichtstrukturiertem Si(11h) mit Werten für h von 2 bis 6 gezeigt.

Die Eliminierung von Stapelfehlern durch LT-AlN-Zwischenschichten ist ein wichtiges Ergebnis des Wachstums von semi-polarem GaN auf Si(112)- und Si(113)-Substraten. Ihre kristalline Qualität wurde mittels verschiedener Verfahren gemessen.

Zum Abschluss wurden semi-polare GaN/InGaN-LED-Strukturen auf der optimierten Pufferstruktur auf Si(112)- und Si(113)-Substraten abgeschieden.

Acknowledgments

I would like to express my gratitude to all the people who supported and encouraged me. Without them I would never have been able to finish my dissertation.

I would like to express my deepest gratitude to the head of my institute, Prof. Dr. Alois Krost, for giving me this fascinating topic and the opportunity to work in his research group for his excellent guidance and financial support.

I would like to express my gratitude to my supervisor, apl. Prof. Dr. Armin Dadgar for guiding my research for the past several years and helping me to develop my knowledge of the MOVPE growth of the GaN layers. I would in particular like to thank him for kindly accepting to referee this work.

I would like to thank Prof. Dr. Ferdinand Scholz for kindly accepting to referee this work.

I would like to thank Prof. Dr. Jürgen Christen for his kindness in enabling me to use the optical instruments in his research group.

I would like to express my sincere gratitude to Dr. Jürgen Bläsing for his all kind support.

My sincere thanks go to Dr. Thomas Hemple, Dr. Peter Veit, Matthais Wieneke, Antje Rohrbeck, Mathias Müller, Anja Dempewolf, Martin Noltemeyer, and Gorden Schmidt for their measurements, for example SEM, TEM, PL, AFM and CL, and also thanks to Dr. Frank Bertram and Sebastian Metzner for all the useful discussions I enjoyed with them.

I would like to express my sincere gratitude to Annette Diez for her kind assistance in the MOVPE laboratory and for her AFM measurements.

I would like to thank Toni Markurt for his HR-TEM measurements and reports.

I would like to thank Dr. Hilde Hardtdegen, Dr. Abdolreza Kharaghani and seyed Hossein Hosseini for kindly commenting my dissertation.

My sincere thanks go to my all co-workers for a wonderful time and the pleasure of working in Germany.

I also would like to express my gratitude to my dear parents and friends for giving me their great love and their endless support. My great thanks also go to my dear sister, Dipl. Ing. Samira Ravash for her patience and encouragement and especially for taking care of my daughter – and a big thank you also goes to my lovely daughter, Zahra Nasirzadeh Niaragh, with my all heart. My great and sincere thanks also go to my dear husband Dr. Oliver Schulz.

I thank God who gave me the opportunity and courage to work here in OVG-University Magdeburg with all the kind and helpful people I met there.

Roghaiyeh Ravash

Magdeburg, Germany

September 2013

Contents

1 Introduction

Group III-nitrides (InN, GaN, AlN) and their compounds demonstrate excellent material properties for electronic and optoelectronic applications. Their direct band gap from 0.7 eV (InN) through 3.4 eV (GaN) to 6.2 eV (AlN) provides optoelectronic devices, e. g. light emitting diodes (LEDs) and laser diodes (LDs) with the possibility of covering the deep ultraviolet and the visible wavelength spectral range. Furthermore, the wide band gap semiconductor with a high breakdown-field (5.10^6 V/cm) [Levinshtein 2001] has attracted great deal of attention concerning high-temperature [Neudeck 2002], high-power, and high-frequency applications such as high-power transistors (high electron mobility transistors (HEMTs)) and surface acoustic wave (SAW) devices [Müller 2006]. It can also be used for sensors in gaseous or liquid environments because of its chemical stability [Pearton 1999].

Starting early in the 20th century, several reports of light emission from materials due to applied electric fields were published [Round 1907]. By the late 1980s and early 1990s, most optoelectronic researchers were focussing on the GaAs- and InP-based material systems. Metal organic vapor phase epitaxy (MOVPE) of a high quality GaN layer was reported by Amano using a thin AlN buffer layer in 1986 [Amano 1986]. P-type conduction in Mg-doped GaN treated with low-energy electron beam irradiation was also demonstrated by Amano [Amano 1989]. The first InGaN grown on GaN films was reported by Nakamura [Nakamura 1992] and GaN based LEDs with bright and sufficient blue luminescence were developed later [Nakamura 1993, Nikkei 1994, Nakamura 1995a, Nakamura 2000]. Later, superbright pure green InGaN-based LEDs were reported, which had a luminous intensity 100 times higher than conventional green GaP-based LEDs [Nakamura 1995b]. Today, most GaN-based devices are still grown along the c-axis direction and blue GaN-based LEDs show high external quantum efficiencies [Narukawa 2010]. However, long wavelength emitters ($\lambda > 500$ nm) show reduced performance.

In wurtzitic III-nitrides a large spontaneous polarization field is oriented along the hexagonal c-axis. This field originates in the noncentrosymmetry of the wurtzite structure and the high electronegativity of nitrogen in comparison to the cation (Ga, Al, In). In addition, these materials show a strong strain-induced piezoelectric polarization in this crystalline direction enhancing or reducing the total polarization field strength. Particularly in quantum wells the electric field induced separation of electrons and holes reduces the radiative transition probability leading to low internal quantum efficiency with high In contents or for thick (thickness ≥ 3 nm) quantum wells. This effect is known as the quantum confined Stark

effect (QCSE). It is reported that shorter wavelength LDs show better quality than green LDs [Strauss 2011], which is demonstrated on conventional c-plane GaN substrates [Avramescu 2009, Miyoshi 2009].

To reduce the QCSE, non- and semi-polar oriented GaN can be used [Waltereit 2000, Chichibu 2006, Baker 2005]. In 1996, growth of GaN epitaxial layers in the m-plane orientation on m-plane oriented SiC was reported [Hirono 1996]. Better performance of non-polar structures were then achieved on small bulk substrates cut from thick c-plane bulk GaN grown by hydride vapor phase epitaxy (HVPE) [Fujito 2009a, Fujito 2009b].

Because of the high cost and limited size of the GaN substrate, hetero-substrates are required for mass production. In many references [Paskova 2008, Speck 2009, Scholz 2012] one can find several approaches, which are used to improve non-polar epitaxial structures to reduce the QCSE.

Non-polar GaN structures grown on hetero-substrates typically lead to defect formation such as threading dislocations and stacking faults in growth directions, which results in low quantum efficiency of optoelectronic devices [Baker 2006, Ng 2002, Lin 2010]. Different groups attempt several growth methods to reduce these defects. Haskell et al. reported defect reduction in $\left(11\bar{2}0\right)$ a-plane GaN via epitaxial lateral overgrowth (ELO) by hydride vapor-phase epitaxy [Haskell 2003]. The fabrication of MOCVD-grown non-polar a-plane violet InGaN/GaN LEDs using reduced defect lateral epitaxially overgrown a-plane GaN templates have been reported by Chakraborty [Chakraborty 2004].

For commercial production large substrate diameters are necessary, which are not available as GaN homo-substrates. Therefore, the growth of GaN-based devices is usually performed on hetero-substrates such as sapphire or SiC. These substrates are expensive and unavailable in diameters above 150 mm. Silicon can be an alternative for these substrates, because of its low price and availability in large diameters with high thermal and electrical conductivity. In addition, silicon offers the possibility of integrating optoelectronics with Si-based electronics. The most significant problem of GaN structures grown on silicon is the thermal expansion coefficient mismatch (it is 54 % in GaN/Si(111)) [Dadgar 2002] leading to cracking of the layers. In 2000, Dadgar et al. reported a method of avoiding cracks by insertion of low temperature AlN interlayers [Dadgar 2000]. Most GaN layers are grown on Si(111) substrates because of the symmetry matching. Threefold symmetry of the Si(111) surface matches with the sixfold symmetry of the polar GaN surface. However, growth of c-axis oriented GaN layers on different Si surface orientations, for example 4° misoriented Si(001) or Si(110) is also possible [Schu04, Schu06, Dadgar2007, Reiher 2009]. Only

recently, attention has been drawn to higher index Si substrates, e.g., Si(112) and Si(113) [Fulk 2006]. Many high index substrates of Si(11h) type typically show a combination of Si(111) and Si(001) surface bonding configuration [Chadi 1984] which can be useful for III–V materials growth as GaP and GaN [Wright 1982, Yang 2009]. Sawaki et al. were able to grow semi-polar $\left(1\,\overline{1}\,01\right)$ and $\left(11\overline{2}2\right)$ GaN layers on patterned Si(001) and Si(113) substrates respectively by an ELO method which also reduces the stacking faults and threading dislocation density [Sawaki 2009]. Several processing steps prior to growth are required for this technique. Therefore, non-c-axis oriented GaN structures on planar high index Si substrates could be a promising approach for enabling a low cost fabrication of polarization field reduced high efficiency light emitters.

In this work MOVPE-growth of polarization reduced GaN layers on planar Si(11h) substrates has been investigated and will be described.

The focus of this thesis was the investigation of semi-polar GaN structures on non-patterned high index Si(11h) grown by metal organic vapor phase epitaxy. Chapter 2 describes the fundamentals of the materials, the MOVPE growth technique and the characterization techniques which are used in this work. Chapter 3 deals with the impact of the AlN seeding layer growth parameters on the GaN crystal orientation on different Si surface directions. In addition, this chapter introduces the importance of LT-AlN seeding layer growth parameters optimization to obtain a single crystalline semi-polar GaN on Si(112) to Si(116). The results of semi-polar GaN growth on Si(112) and Si(113) are described in chapter 4. Here, stacking fault elimination by insertion of a LT-AlN interlayer has been observed for the first time and is also described in detail. Finally semi-polar GaN LED structures grown on Si(112) and Si(113) are presented in Chapter 5.

2 Fundamentals

The main goal of many material studies is to improve the performance of devices. In c-plane GaN films, which are widely applied in InGaN-based light-emitting diodes, internal electric fields (along the c-direction) have been shown to be detrimental to luminescence efficiency. In such quantum wells, the electric field induces a separation of electrons and holes and causes a reduction of the radiative recombination rate leading to low efficiency for thick quantum wells [Lefebvre 2001] or at high indium content [Li 2013]. Because of this, the search for high efficiency luminescence in the visible spectral range is still a challenging task [Scholz 2012]. The growth of non-c-axis-orientated LED structures is a promising way to achieve a significant enhancement in light emission efficiency by a reduction of the QCSE [Waltereit 2000]. Many groups have focussed on this field over many years, but a large number of optimizations in terms of structural properties, processing and especially substrates is still necessary. Up to now, most of the investigations were performed on small GaN bulk substrates, silicon carbide or sapphire substrates. Silicon is the substrate of choice for the cheap production of GaN-based devices and an integration of optoelectronics with silicon-based electronics. As will be shown in this work, growth on high index silicon substrates is a promising alternative substrate for semi-polar gallium nitride growth. In this chapter, the fundamental properties of GaN, the effect of polarization fields along the c-axis, the QCSE in GaN/InGaN QW and stacking faults are discussed. In addition, the Si substrate and in particular high index Si(11h) and its preparation are described. Finally, the principle of MOVPE and the characterization methods used in this work are briefly explained.

2.1 Properties of group III-nitrides

Group III-nitrides and their alloys can be grown in both wurtzite and zinc blende structures depending on the growth conditions and substrate used [Morkoc 2008]. Commercially available devices typically consist of heterostructures of AlN, GaN, and InN and their ternary alloys of the wurtzite-phase of these materials. The cohesive energy per bond in the wurtzite structure of AlN, GaN, and InN is 2.88 eV, 2.2 eV, and 1.93 eV respectively [Harrison 1980]. The calculated energy difference between the wurtzite and zinc blende lattice (ΔE_{W-ZB}) is -18.41 meV/atom for AlN, -11.44 meV/atom for InN and -9.88 meV/atom for GaN. [Morkoc 2008]. Therefore, the wurtzite form for these three nitrides is energetically preferred and thermodynamically stable.

The wurtzite structure consists of two interpenetrating hexagonal close packed (hcp) lattices. One lattice consists of metal atoms e.g., Ga, Al, In and the other lattice contains nitrogen atoms with an ideal distance between the nitrogen and metal atoms along the c-axis of *uc = 3/8c. c* is the distance between e. g. two Ga atoms or two N atoms along the c-axis and *u* is an internal parameter. A wurtzite structure has a …AaBbAaBb… stacking sequence along the c-direction [0001]. Capital letters illustrate group-III atoms and lower case letters indicate N atoms. Fig 2.1 shows a schematic diagram of a hexagonal wurtzite GaN structure. For a Ga-face GaN structure, the c-direction [0001] is defined by the direction from a Ga atom to its next bonding N atom along the c-axis.
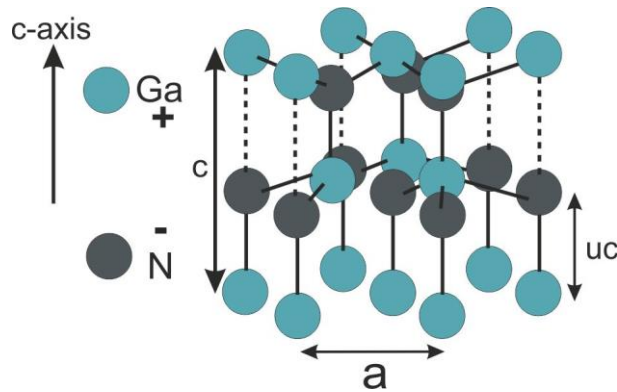
Fig. 2.1: *Schematic illustration of the hexagonal wurtzite GaN structure.*

Table 2.1: *Material properties of GaN and AlN, and InN [Wang 2001, Ambacher 1998, Ambacher 1999, Bernardini 1997].*

Material	a-lattice constant (Å)	c-lattice constant (Å)	c/a (1.633)	P_{sp} (C / m^2)	Decomposition temperature (K) (at 1 bar N$_2$ pressure)
GaN	3.189	5.185	1.626	-0.029	1150
AlN	3.112	4.98	1.601	-0.081	2800
InN	3.537	5.703	1.612	-0.032	630

An ideal wurtzite crystal has a ratio of the lattice constants c (in the perpendicular direction to the basal plane) and a (in the basal plane) of $c/a = \sqrt{\dfrac{1}{u}} = \sqrt{\dfrac{8}{3}} = 1.633$.

In wurtzite group III-nitrides, the experimental values of the $\frac{c}{a}$ ratios are smaller than the ideal values and the non-ideality of the crystal structure increases from GaN to InN to AlN corresponding to the increase in spontaneous polarization (Table 2.1).

Wurtzite group III-nitrides have a direct band gap of 6.2 eV for aluminum nitride, 3.4 eV for gallium nitride and around 0.7 eV for indium nitride at room temperature. Therefore, these semiconductor materials can theoretically cover the whole wavelength range from deep ultraviolet to infrared. Material properties of GaN, AlN, and InN are listed in Table 2.1.

In semiconductor materials, the concentration of intrinsic carriers (n_i) is exponentially dependent on temperature [Pierret 1987, Sze 1981],

$$n_i = \sqrt{(N_C N_V)}\, e^{-E_g \big/ 2kT} \qquad (1)$$

where T is the temperature in K, k the Boltzmann constant ($8.62 \cdot 10^{-5}$ eV/K), and E_g the band gap energy of the semiconductor (eV). The effective electron and hole density of states for the semiconductor (cm^{-3}) are N_C and N_V, respectively. E_g, N_C, and N_V are fundamental crystal properties, which have less temperature dependence than the term $(-E_g \big/ kT)$ in equation 1.
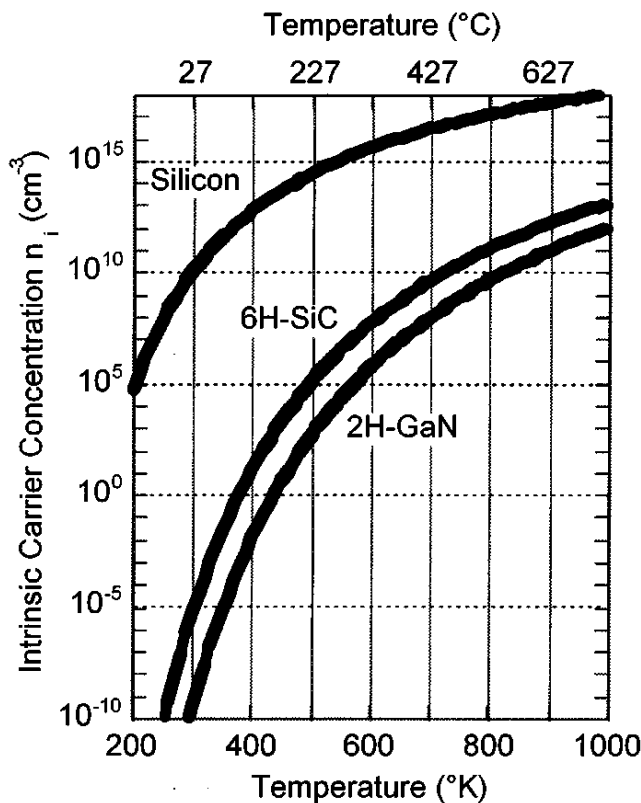

Fig. 2.2: *Semiconductor intrinsic carrier concentration (n_i) versus temperature, for silicon, 6H-SiC, and 2H-GaN. (Based on respective temperature-dependent material properties [Sze 1981, Pearton 1999, Neudeck 2002].*

Fig 2.2 shows n_i of silicon, SiC and 2H-GaN, which is calculated using equation (1). Depending on devices, the lowest doping densities of silicon is usually between 10^{14} and 10^{17} atoms / cm^3. At room temperature, the n_i of silicon (bandgap =1.1 eV) is about 10^{10} atoms / cm^3. If the temperature is increased higher than 300 °C, there may be more intrinsic carriers present than dopant carriers in an assumed silicon device. Thus, the electrical conductivity of lighter doped areas of silicon devices becomes undesirably influenced by intrinsic carriers instead of the designed doping needed for proper electrical operation. As shown in Fig. 2.2, SiC and GaN as wide-bandgap (about 3 eV) semiconductors have much lower intrinsic carrier concentrations than silicon and, thus, do not run into intrinsic carrier conductivity difficulties until much higher temperatures, beyond 600 C. Therefore, group III-nitrides are suitable semiconductor materials for high-temperature applications [Neudeck 2002].

As mentioned above, group III-nitrides (especially AlN and GaN) are crystals with high bonding energies resulting in high melting points and good thermal stability. The strong triple bond of the N_2 molecule (4.9 eV/atom) leads to a decrease in Gibbs free energy ($G = H - S.T$) of the nitride constituents, i.e. metal (Ga, Al, In) atoms and nitrogen atoms.
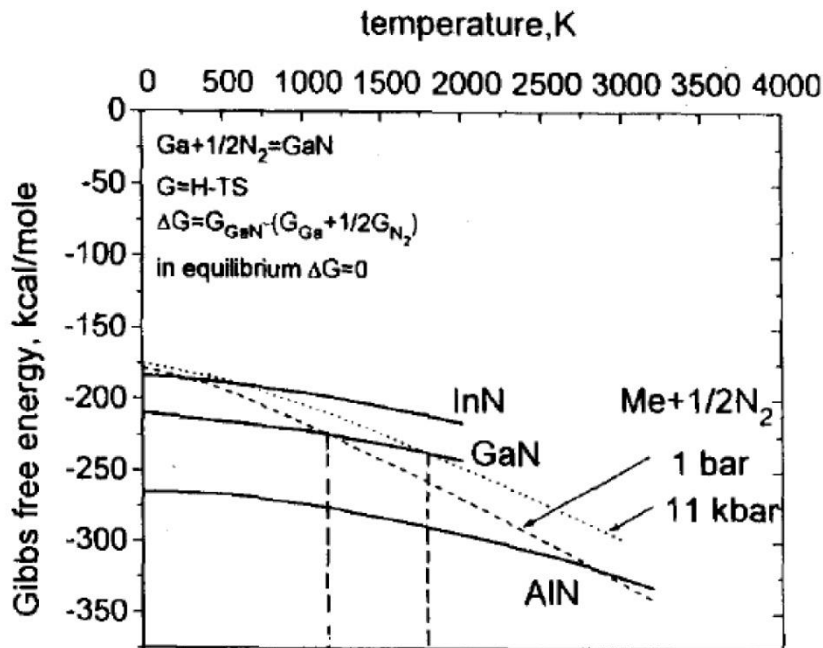

Fig. 2.3: *Gibbs free energy (G) changes with temperature for group III-nitrides and their constituents. The solid lines show G for nitrides at N_2 pressure of 1 bar, the dashed lines show G for their constituents. G for the constituents is the sum of average energy of the metal and the free energy of nitrogen at a pressure of 1 bar and 11 kbar [Porowski 1996].*

Since the free energy of constituents decreases faster with temperature than the free energy of the group III-nitride crystals, the stability of nitrides decreases at high temperatures (due to a high entropy value).

In Fig. 2.3 the temperature dependence of Gibbs free energy for nitrides at N_2 pressure of 1 bar is shown. The free energy of nitrides constituents is very sensitive to N_2 pressure. By increasing the N_2 pressure from 1 bar to 11 kbar, the stability of the nitride crystals increases.

Due to the lack of native GaN substrates, GaN growth is mainly performed on heterosubstrates. In this work semi-polar InGaN/GaN LED structures were grown on optimized GaN buffer layers on Si(11h) substrates.

2.2 Polarization of group III-nitrides and quantum confined Stark effect

In the following section, polarization fields and their influence on the physical properties of group III-nitrides will be described.

In wurtzite group III-nitride structures (in the absence of external electric fields), polarization can be categorized into two types, spontaneous and piezoelectric polarizations.

The spontaneous polarization ($\vec{P}_{SP}$) (polarization at zero strain) differs from zero due to its noncentrosymmetry property. In such structures the high electronegativity of nitrogen in comparison to Ga, Al and In in the metal-nitrogen bond causes a large spontaneous polarization along the c-axis. Its direction is polarity dependent, i.e. it is towards the opposite direction of the c-axis in Ga-face and towards the c-direction in the case of N-face GaN. The calculated values of spontaneous polarization are very large and increase slightly from GaN to InN and significantly in AlN [Bernardini 1997]. Note that there is a spontaneous polarization in an ideal wurtzite crystal because there is no inversion symmetry. This is not due to structural non-ideality [Zoroddu 2001, Bruns 1985]. In the [111]-direction of a zinc blende crystal, comparable to the [0001] direction in wurtzite crystals, no spontaneous polarization field exists due to symmetry.

Piezoelectric polarization ($\vec{P}_{PE}$) is a strain-induced polarization, which, depending on the strain, can point in any direction along the c-axis. It increases with increasing lattice mismatch, e.g. between the active InGaN layer and the GaN barrier. The direction of $\vec{P}_{PE}$ depends on the polarity and strain of group III-nitrides. For instance, in the case of Ga-face nitrides, in a compressively strained InGaN on GaN layer, $\vec{P}_{PE}$ is oriented towards the [0001]-direction. In the case of a tensile strained AlGaN on GaN layer (Ga-face), $\vec{P}_{PE}$ is oriented towards a direction opposite to the [0001]-direction. Therefore, it can be concluded that the

orientation of the spontaneous and piezoelectric polarization is in the same direction if the AlGaN layer grown on GaN is under tensile strain, and in the opposite direction in the case of a compressively strained InGaN on GaN layer.

The piezoelectric tensor of wurtzite group-III nitrides InN, GaN, and AlN has three independent components. Two of these components, e_{31} and e_{33}, measure the piezoelectric polarization, $\vec{P}_{PE}$, induced by strain along the c-axis [Ambacher 1999]. The relevant relationship is

$$\vec{P}_{PE} = e_{33}\varepsilon_z + e_{31}\left(\varepsilon_x + \varepsilon_y\right), \qquad (2)$$

where $\varepsilon_z = \dfrac{c - c_0}{c_0}$ is the strain along the c-axis, and $\varepsilon_x = \varepsilon_y = \dfrac{a - a_0}{a_0}$ is the in-plane strain, which is assumed as an isotropic strain. a_0 and c_0 are equilibrium values of lattice parameters. a and c are the lattice parameters of the strained layer. The relationship between the lattice constants in hexagonal GaN can be written as

$$\frac{c - c_0}{c_0} = -2\frac{C_{13}}{C_{33}}\frac{a - a_0}{a_0}. \qquad (3)$$

Thus, $\vec{P}_{PE}$ becomes

$$\vec{P}_{PE} = 2\frac{a - a_0}{a_0}\left(e_{31} - e_{33}\frac{C_{13}}{C_{33}}\right), \qquad (4)$$

where C_{13} and C_{33} are elastic constants.

Equations 3 and 4 are valid only for small strain values, e.g. between GaN and AlGaN [Ambacher 1998]. For high In or Al content AlInN and InGaN alloys on GaN, nonlinear terms have to be taken into account for the spontaneous and piezoelectric polarization as well as for the elastic constants. More information can be found in [Morkoc 2008].

Spontaneous and strain induced piezoelectric polarizations can govern optical and electrical properties of GaN-based heterostructures. In c-axis oriented GaN structures fixed sheet charges form at heterointerfaces owing to discontinuities in $\vec{P}_{SP}$ and $\vec{P}_{PE}$ between constituent layers. A positive application of these polarization fields is used by high-electron mobility transistors (HEMTs) and field effect transistors (FETs) [Khan 1991, Rajan 2004]. For example, a tensile strained AlGaN layer in c-axis oriented AlGaN/GaN heterostructures leads to the existence of a piezoelectric field in the opposite [0001]-direction. The polarization discontinuity at AlGaN/GaN interface causes a positive fixed sheet charge providing the

source of a two-dimensional electron gas (in the layer with the smaller bandgap close to the interface) when the AlGaN layer has a suitable thickness.

In polar nitride structures, polarization and internal electric fields have been shown to be detrimental to the performance of optoelectronic devices, e.g. LEDs or LDs [Langer 1999, Degushi 1999]. These fields lead to a significant band bending and a pronounced quantum confined Stark effect (QCSE) in c-axis oriented III-nitride quantum well structures for thick quantum wells or high indium contents [Waltereit 2000, Romanov 2006]. As a consequence, electron and hole wave functions are spatially separated [Miller 1984] leading to a reduction in the radiative recombination probability resulting in low efficiencies and a redshift of the emission wavelength. In QWs with higher In concentration, although the emission goes towards a longer wavelength, the overlap of the wave function is reduced because the polarization field increases due to an enhancement of the lattice mismatch (strain) [Feneberg 2007].
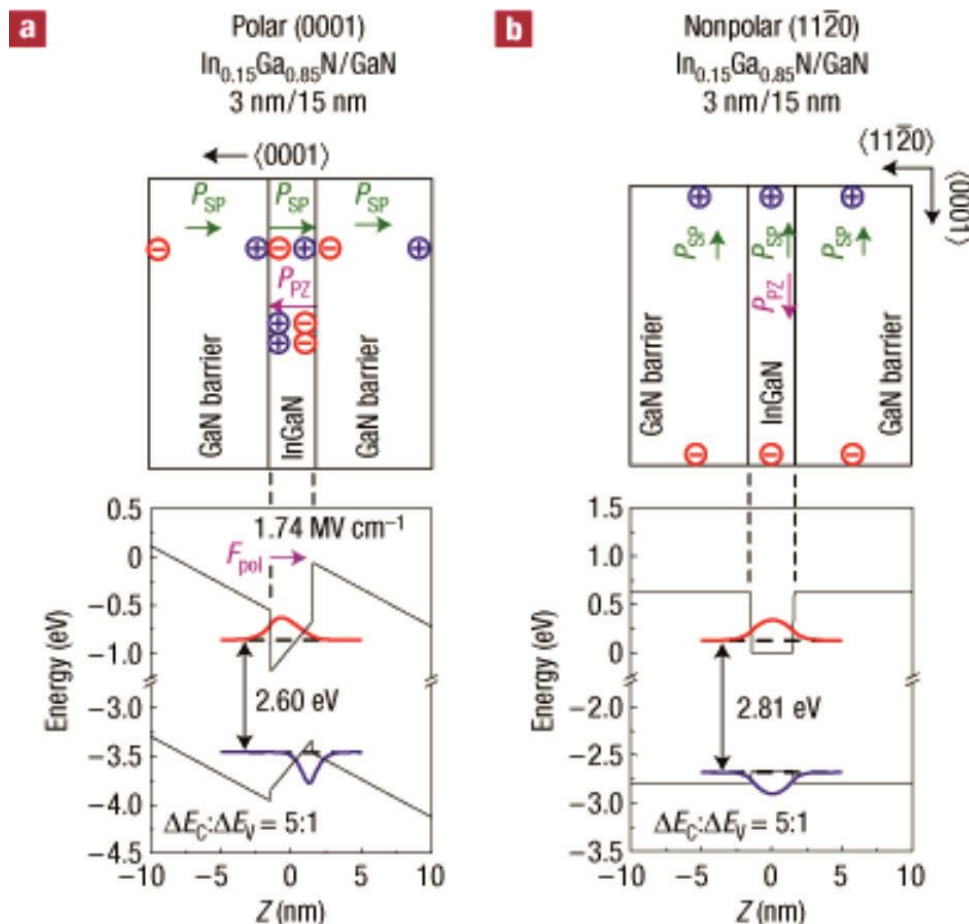

Fig. 2.4: *Showing the direction of the spontaneous and piezoelectric polarizations and F_{pol} and energy band diagram (a) in a polar Ga-face InGaN/GaN QW, (b) in a non-polar InGaN/GaN QW. The direction of the internal polarization field F_{pol} pointed from the top interface to the bottom interface [Chichibu 2006].*

As shown in Fig. 2.4 (a), in a polar wurtzite Ga-faced nitride structure, a spontaneous polarization leads to negative and positive immobile charges at the top and bottom interfaces respectively. $\vec{P}_{SP}$ is oriented towards the opposite direction of the c-axis. Because the InGaN QW is compressively strained, piezoelectric polarization charges (induced by a $\vec{P}_{PE}$ along the c-axis) with an opposite sign to $\vec{P}_{SP}$ also appear at the respective interfaces. Owing to the large lattice mismatch between GaN and InN ($\Delta a/a \sim 11\%$), the total polarization is mostly dominated by $\vec{P}_{PE}$ [Takeuchi 1997, Bernardini 1998], which leads to the internal polarization field (F_{pol}). Thus, a large F_{pol} results in a strong quantum confined Stark effect (QCSE), i.e. the reduction of the electron and hole wave function overlap and emission efficiency. Fig. 2.4 (b) shows that in a hexagonal a-plane InGaN QW, F_{pol} is parallel to the QW plane and the QW shows no QCSE in growth direction [Waltereit 2000]. However, in order to reduce the QCSE and consequently improve the quantum efficiency, the absence of the electric fields in the growth direction is necessary and the main reason for the non-polar GaN layers growth.

In order to reduce the QCSE and consequently improve the quantum efficiency, non-polar or semi-polar group III-nitride structures can be applied. As shown in Fig. 2.5, non-polar GaN planes are a-plane and m-plane. In these growth directions there is no polarization field. The planes between polar- and non-polar planes are called semi-polar planes [Baker 2005].

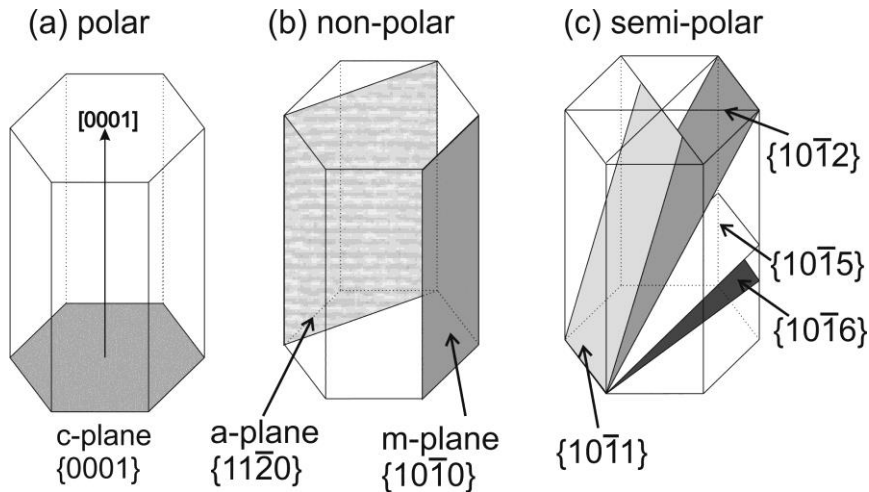**Fig. 2.5:** *GaN planes: (a) polar c-plane, (b) non-polar m-plane and a-plane, (c) semi-polar $\{10\bar{1}l\}$-planes such as $\{10\bar{1}1\}, \{10\bar{1}2\}, \{10\bar{1}5\}, and \{10\bar{1}6\}$ planes. Table 2.2 shows angles β (°) between the GaN $\{0001\}$-plane and GaN $\{10\bar{1}l\}$-planes. Regarding the GaN c-axis tilt angle one can know which GaN plane is grown parallel to Si substrate surface.*

Table 2.2: *Angle β (°) between the GaN $\{0001\}$-plane and GaN $\{10\bar{1}l\}$-planes.*

$\{10\bar{1}l\}$	$\{10\bar{1}1\}$	$\{10\bar{1}2\}$	$\{10\bar{1}3\}$	$\{10\bar{1}4\}$	$\{10\bar{1}5\}$	$\{10\bar{1}6\}$
Angle β (°)	61.96	43.19	32.04	25.14	20.58	17.38

Romanov et al. reported that in a compressively strained $In_xGa_{1-x}N$ quantum well with GaN barriers, the total polarization ($P_{tot, z}$) is a function of the c-axis inclination angle (θ) with respect to the surface normal (Fig. 2.6 (a)). The angle θ (degree) is shown in Fig. 2.6 (b).
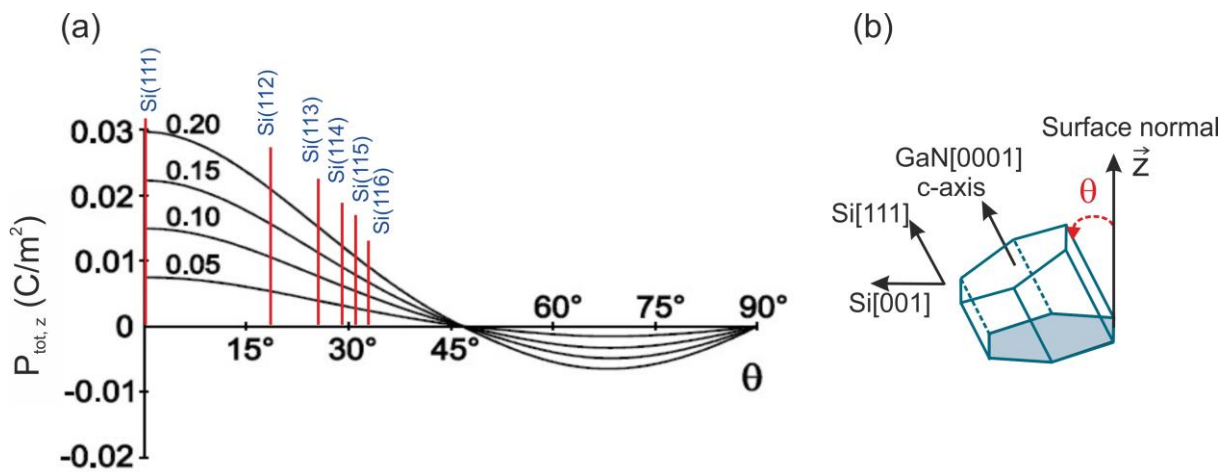

Fig. 2.6: *Polarization dependency of semi-polar layers under biaxial compression, a) the normal component of polarization $P_{tot, z}$ at the layer/template interface for $In_xGa_{1-x}N$ layers on a GaN substrate, for x=5%, 10%, 15%, and 20% (after [Romanov 2006]). b) Angles (θ) show the c-axis inclination angle with respect to the substrate normal. Red lines show positions of experimental values of GaN c-axis-tilt angle grown on Si(11h) [more details are presented in capital 3.2.3].*

The results demonstrate that the total polarization becomes zero, not only for non-polar oriented $In_xGa_{1-x}N$ layers but also for semi-polar layers at an angle θ of about 45°. In addition, $P_{tot, z}$ is reduced for other semi-polar oriented layers [Romanov 2006].

2.3 Non-polar and semi-polar growth

Non- and semi-polar GaN-based optoelectronic device structures have attracted much attention in recent years in order to improve the quantum efficiency of such devices [Paskova 2008]. The best non- or semi-polar GaN layers have been demonstrated on small bulk substrates cut from thick c-plane layers [Yoshizumi 2009]. Therefore, some groups have used bulk non- and semi-polar substrates for $(10\bar{1}0)$ m-plane [Masui 2005] and $(11\bar{2}2)$ plane [Funato 2006] cut from thick hydride-vapour-phase epitaxy (HVPE) boules resulting in higher efficiencies of InGaN/GaN LEDs. These polar GaN wafers grown by HVPE have a thickness of several millimeters [Fujito 2009a]. Thus, the area of such non- or semi-polar GaN substrates is limited by this wafer thickness, i. e. about a few centimeters long and some millimeters wide. Unfortunately, the typical bowing of such wafers causes a slightly bent crystal lattice on the non-polar surface [Scholz 2012]. The first green LED grown on semi-polar bulk substrate was reported by Yoshizumi et al. [Yoshizumi 2009]. Other groups have applied hetero-substrates such as sapphire or SiC and Si for non- and semi-polar GaN growth. This has the benefit of much larger available substrate sizes. On Si substrates, non- or semi-polar GaN templates were obtained using a selective area growth method on patterned foreign substrates [Sawaki 2010]. A GaInN/GaN LED was fabricated on such GaN templates on Si(001) [Chiu 2011]. Scholz reviewed the current state of studies of non- or semi-polar nitride structures and discussed several approaches of realizing respective epitaxial structures [Scholz 2012]. Despite all of these successful methods, there is a significant problem in non-c-polar GaN grown on foreign substrates. Since the materials are often grown on substrates with different lattice parameters from that of the layer, dislocations easily evolve in such layers. Moreover, stacking faults can form at the substrate interface or upon coalescence which are not problematic in c-plane GaN layers [Liu 2005]. Epitaxial lateral overgrowth (ELOG), sometimes also called sidewall lateral epitaxial overgrowth (SLEO) is successfully applied to decrease both the dislocation and stacking fault density [Imer 2006]. ELOG is used to form three-dimensional GaN structures providing (nearly) defect free semi-polar crystal facets [Wunderer 2011]. Other approaches to reduce these defects are in-situ deposited SiN or ex-situ deposited ScN interlayers [Moram 2009, Johnston 2009]. Basal plane stacking faults can be significantly reduced using simple methods such as a low temperature AlN interlayer insertion in GaN layers [Dadgar 2011, Patent Nr. 10 2011 011 043.7, Ravash 2012].

2.4 Si substrates

Silicon is the second most abundant element on earth and always occurs in the form of a compound, often as the oxide (silica). Silicon crystallizes in the diamond structure, which can be described as a combination of two interpenetrating fcc lattices, which are displaced by ¼ of the distance along a body diagonal to each other as shown in Fig. 2.7 (a). The side view along the Si[111] direction and the …AaBbCcAaBbCc… stacking sequence of a close-packing Si structure is shown in Fig. 2.7 (b). Silicon reacts with oxygen and forms a thin layer of SiO_2. Si is favored as a material for integrated circuits because of two properties its possible operation at higher temperatures than germanium and its thin native oxide, which can act as a diffusion barrier, insulating layer, etc. and which protects the silicon surface. Silicon has a great impact on semiconductor device production because of its very high crystalline quality and material properties.
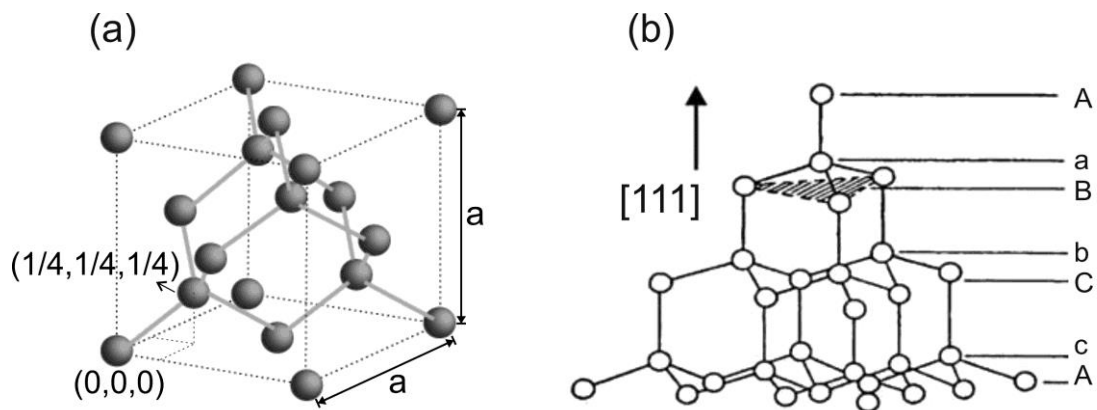

Fig. 2.7: *Crystal structure of Si and the side view along the [111] direction [Omara 1990].*

The growth of III-nitrides such as GaN on silicon has attracted much attention due to a possible integration of optoelectronics with Si-based electronics. Furthermore, silicon can be considered favorably as an alternative substrate, because of its unique properties as well as being inexpensive, it is easily available, and has a large wafer diameter of up to 300 mm.

The (001), (113), (111) and (110) surfaces of silicon are known as primary surfaces which have smaller surface energies in comparison to the surface energies of their vicinal surfaces, i.e. the surfaces with a few degrees off-orientation. These vicinal surfaces have flat primary terraces separated by steps. The result of a compromise between step energies and energies of primary surfaces determines the thermodynamic equilibrium shape of the silicon surfaces.

The angle between the Si(111) and Si(001) planes is 54.7 °. The primary surface Si(113) lies between these planes having an inclination angle of 29.5 ° with respect to the Si(111) surface. The clean Si(113) surface is thermally stable [Eaglesham 1993] having a surface energy which is close to that of Si(111) and Si(001).

The good match of the hexagonal GaN with the three-fold symmetry of Si(111) leads to c-axis orientated growth of GaN on this surface. GaN LEDs on Si(111) have been demonstrated by several groups [Feltin 2001, Dadgar 2002, Dadgar 2003, Zhang 2007]. Some groups have demonstrated c-axis oriented GaN on other Si surface orientations, e.g. on Si(001) [Schulze 2006, Schulze 2007, Schulze 2008], and on Si(110) [Dadgar 2007, Damilano 2008, Reiher 2009]. The most significant problem for the growth of GaN on Si is the thermal expansion coefficient mismatch of GaN and Si leading to cracking of the layers.

2.4.1 Si(11h) structures

Low index Si surfaces such as Si(001) and Si(111), which are commonly used in Si industry, have been intensively investigated so far. Only recently, attention has been drawn to higher index Si substrates, e. g. Si(112) and Si(113) [Fulk 2006]. On Si(113), Tanikawa et al. have demonstrated the growth of polarization reduced $GaN(11\bar{2}2)$ layers by structuring the substrates to form inclined Si(111) planes on which c-axis oriented GaN is grown selectively [Tanikawa 2008]. Semi-polar $GaN(11\bar{2}2)$ layers were selectively grown by metal organic chemical vapor phase epitaxy on structured Si(113) substrate without a SiO_2 mask. It was observed that the number of emission intensity related crystal defects is drastically reduced in the case of selective growth without SiO_2 masks as compared to that obtained with SiO_2 masks [Yang 2009]. Ni et al. reported non-polar m-plane GaN on patterned Si(112) substrates by metal organic chemical vapor deposition [Ni 2009]. However, this technique requires several processing steps before growth, which increase cost and time.

The surface of planar high index silicon, e.g. Si(11h), typically shows a terrace-plus-step morphology. The combination of Si(111) and Si(001) surface bonding configurations in Si(11h) surfaces [Chadi 1984] can be useful for III-V material growth as for GaP and GaN [Steven 1982, Yang 2009]. A determination of the hydrogen-covered Si(112) surface geometry by means of low energy electron diffraction (LEED) has been performed by Kaplan showing a periodically stepped surface with Si(111) terraces [Kaplan 1982].

Because of the impossibility of accurately determining the reconstructions of silicon surfaces under investigated MOVPE conditions, a simple geometrical argument of surface

step structures for high index Si(11h) surfaces is assumed [Ueda 1985]. It is also assumed that the structure of Si(11h) surfaces is combined from Si(001) and Si(111) surface sections as terrace and step structures (Fig. 2.9).
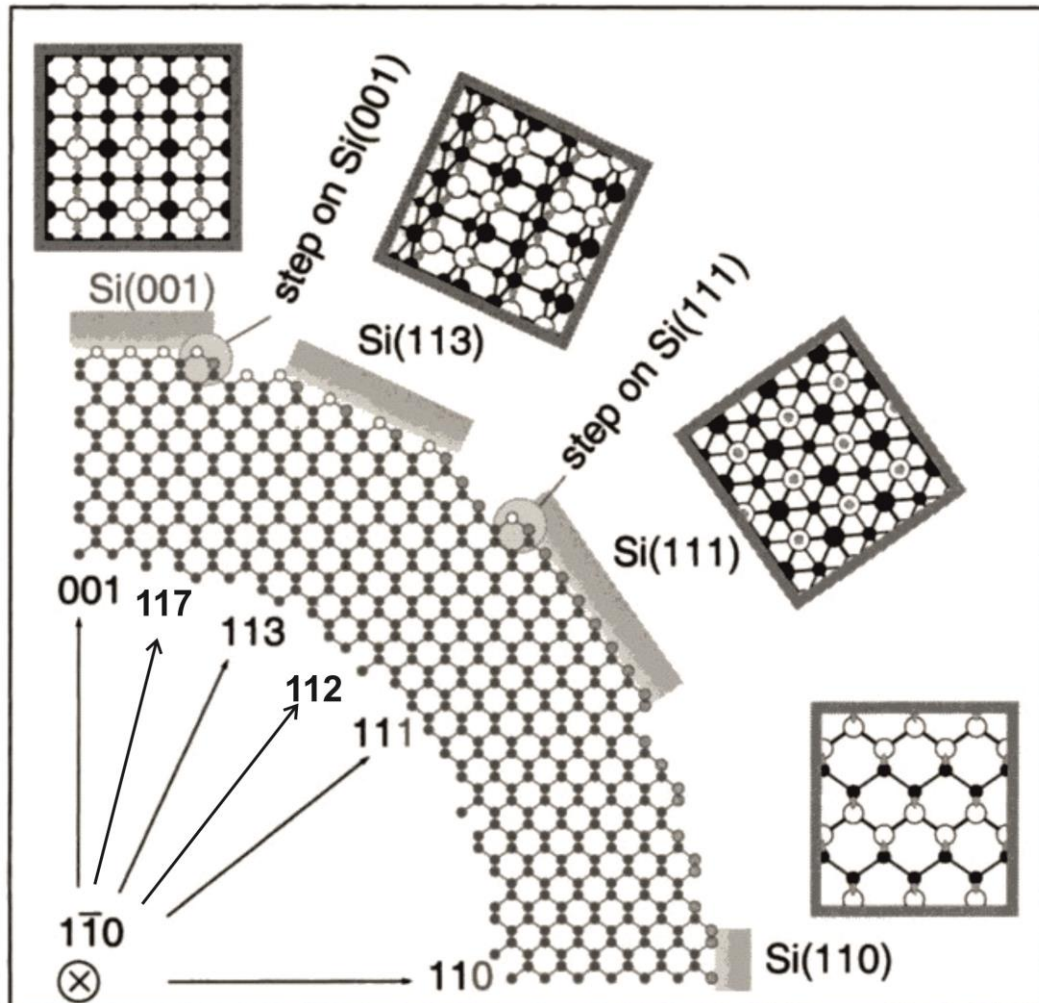

Fig. 2.8: *Several silicon surfaces from Si(001) to Si(110). The top-views of Si(001), Si(113), Si(111) and Si(110) surfaces are depicted from the left to the right [Dabrowski 2000].*

Surfaces of the Si(11h) orientations are the family of silicon surfaces between the Si(001) and Si(111) planes, whereby h is from 2 to 7 (Fig. 2.8). The angles between Si(111) and Si(11h) can be defined by $\cos\alpha = \dfrac{(h+2)}{\sqrt{3(h^2+2)}}$ (Table 2.3) [Dabrowski 2000]. The ratio of these Si(001)/Si(111) planes depends on the value of h and increases from Si(112) towards Si(117). As shown in Fig. 2.8 the Si(113) surface consists of a nearly equal fraction of Si(001) and Si(111) surfaces. More detailed information on the reconstructions of silicon surfaces oriented between Si(001) and Si(111) can be found in [Baski 1997, Berghaus 1987].

As shown in Fig. 2.9, it is expected that the GaN film can most likely grow on the Si(111) facets usually formed on the Si(11h) surface.

Table 2.3: *Si(11h) planes and their angles with Si(111) planes. Si(111) plane fraction of different Si(11h) surfaces [Baski 1997].*

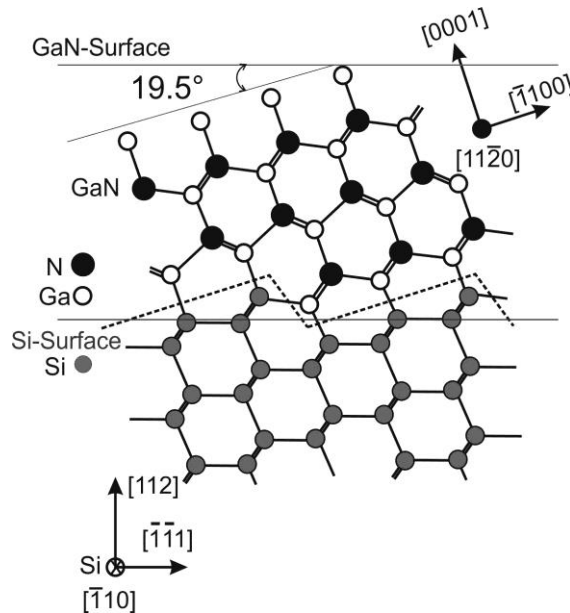| Si(11h)	α (°) = Theoretical Angle between Si(111) and Si(11h)	Si(111)plane fraction of substrate surface
(111)	0°	100%
(112)	19.5°	64%
(113)	29.5°	46%
(114)	35.3°	36%
(115)	38.9°	29%
(116)	41.5°	24%
(117)	43.3°	21%
(001)	54.7°	0%

Fig. 2.9: *Atomic arrangements of a GaN film on bulk-terminated Si(112). The free Si(112) surface consists of twofold-coordinated Si(001) and threefold-coordinated Si(111) as step and terrace surfaces respectively. The ideal Si(112) surface has an angle of 19.5° to the Si(111) surfaces.*

2.4.2 Substrate preparation

Prior to the MOVPE growth process, the silicon substrate should be cleaned in order to obtain a well-defined atomically clean silicon surface without any oxide or other contamination. Some groups use an in-situ cleaning process in the reactor by heating to temperatures above 1000 °C under hydrogen. This method does, however, bear the risk of surface contamination from deposits in the reactor as Ga and Al. Wet chemical etching of silicon is another method of cleaning the Si surface, and was used in this work prior to loading the substrates into the reactor. At first, the substrate was cleaned in isopropanol using an ultrasonic bath to remove dust particles. Subsequently, to remove the organic contaminants the substrate was immersed in a solution of H_2SO_4:H_2O_2:H_2O with a ratio of (3:1:1) for one minute [Grundmann 1991, Itano 1993]. There, the substrate surface will be etched and completely oxidized. Next, the wafer was immersed in HF (5 %) for 30 seconds in order to remove the resulting oxide layers from the surface. After each process, the wafer was rinsed in deionized water until the resistivity of the waste water reached 2 MΩ cm. These processes are repeated twice to remove the contaminants and surface defects from the wafer surface resulting in an oxide-free, hydrogen-terminated silicon surface.

2.5 The principle of metal organic vapor phase epitaxy

All investigated samples in this work were grown by metal organic vapor phase epitaxy (MOVPE) using an AIXTRON AIX 200/4 RF-S single two inch wafer horizontal cold wall reactor. Trimethyl-aluminum (TMAl), Trimethyl-gallium (TMGa), Trimethyl-indium (TMIn) and ammonia (NH_3) were the reactant materials for Al, Ga, In and N respectively. The source materials in MOVPE systems are gaseous precursors such as NH_3, liquids such as TMAl and TMGa, or solids such as TMIn. A separate inlet for metalorganic precursors and ammonia is helpful to minimize the pre-reactions. The group-III precursors are transported by a carrier gas of high purity, H_2 or N_2, from the bubbler to the reactor, where a heated substrate is placed on a rotating SiC coated graphite susceptor. The susceptor is heated by a radio frequency (RF) heating system. The gas-foil rotation of the substrate holder enhances the uniformity of the deposited layers. For reasons of uniform deposition, usually nowadays a low operating pressure (70 to 200 mbar) for carrier gases is preferred [Herman 2004].

In order to control the precise flow rate of the source materials into the reactor, mass flow controllers (MFC) were employed.

If $Q_{p,gas}$ is the gas flow of the gaseous precursor and Q_{tot} the total flow into the reactor, the relationship between the partial pressure of the gaseous precursor $P_{p,gas}$ and the total pressure in the reactor $P_{reactor}$ is given by:

$$P_{p,gas} = \frac{Q_{p,gas}}{Q_{tot}} P_{reactor} \qquad (5)$$

The amount of reactants fed into the reactor is controlled via the vapor pressure of the liquid or solid precursors given by their temperature. Applying a well-controlled temperature bath, the vapor pressure of the precursor has a well regulated value. Thus, bubblers, which were used in MOVPE as delivery systems for liquid or solid precursors, (Fig. 2.10 (a)) were kept in a thermal bath at a constant temperature such as 17 °C and 0 °C for TMAl and TMGa respectively. In a bubbler a carrier gas is bubbled through the reactant and the saturated vapor of the reactant is transported into the reactor. For this case, the partial pressure $P_{p,gas}$ is given by:

$$P_{p,gas} = \frac{Q_{p,liquid}}{Q_{tot}} \cdot \frac{P_{reactor}}{P_{bubbler}} P_{vap}(T) \qquad (6)$$

whereas $Q_{P,liquid}$ is the flow of MO sources through the bubbler, $P_{vap}(T)$ the equilibrium vapor pressure of the liquid, and $P_{bubbler}$ the pressure in the bubbler [Hermann 2004].
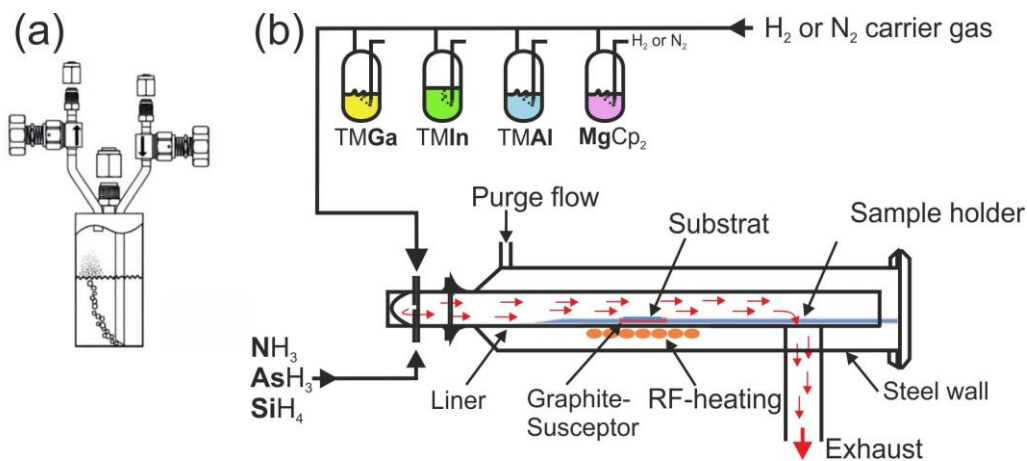

Fig. 2.10: (a) *Cross-section of a bubbler [Herman 2004], (b) schematic illustration of a basic MOVPE system [AHE].*

The MOVPE process is a common technique to grow thin films and shows complex transport phenomena and homogeneous (reaction in the gas phase) as well as heterogeneous (reaction in the gas-solid interface) reactions. As mentioned above, the high-purity source materials are transported to the substrate by a carrier gas. The precursors' molecules decompose due to the high process temperature in the gas phase and pre-react with other precursors and diffuse to the growing surface because of a concentration gradient. There, the surface chemical reaction such as adsorption, surface migration, incorporation, and desorption of the chemical species leads to epitaxial growth. Gaseous by-products can desorb from the surface and diffuse in the carrier gas away from the deposition area towards the reactor exhaust. A schematic illustration of the MOVPE system is shown in Fig. 2.10 (b).
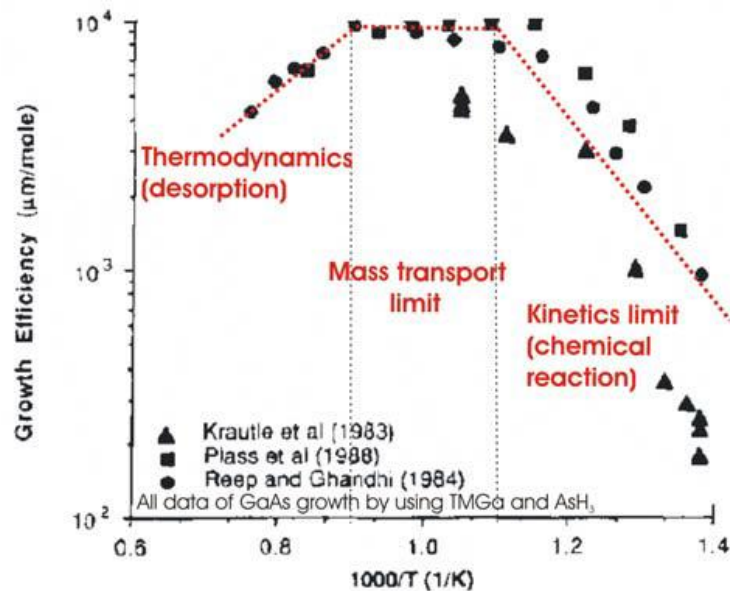

Fig. 2.11: *Temperature dependence of MOVPE growth rate after [Stringfellow 1989].*

The three main regimes of temperature dependence of the growth rate in MOVPE system are shown in Fig. 2.11. At low temperatures the transport is fast and chemical kinetic or surface reactions are slower and limit the growth rate. There, the temperature determines the growth rate. An almost exponential increase in growth rate can be achieved by increasing the temperature. This region is called kinetic limited regime. At higher temperatures the reactions are fast and the mass transport is lower. In this region growth rate is independent of the temperature and called mass transport limited regime. At very high temperatures thermodynamics limits the growth rate which decreases with increasing temperature. In this thermodynamic limited regime gas-phase pyrolysis of the hydrides becomes dominant and solid particles could form without being deposited on the substrate. Here, an enhanced

pre-deposition on the reactor wall or on the susceptor and desorption of the growing species from the surface could be performed.

At the growth temperature of the GaN layer (higher than 1200 K), TMGa reaction with the ammonia can be written as simple following reaction regardless other complex reactions

TMGa (gas) + NH$_3$ (gas) $\rightarrow$ GaN (solid) + 3 CH$_4$ (gas)   (7)
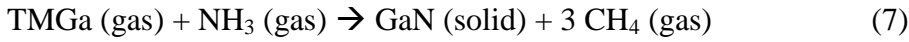
More detailed information about the MOVPE process can be found in reference [Herman 2004].

2.6 Problems in GaN layer grown on Si

The deposited layer quality depends on the lattice mismatch between the layer and the substrates as well as the layer growth parameters. A large lattice mismatch (-16.9 %) [Krost 2002] and thermal expansion coefficient mismatch (54 %) [Krost 2002] between GaN and Si(111) leads to a mismatch, treading dislocations and crack formation in GaN layers. In addition, melt back etching and nitridation of Si substrate surface are other problems when GaN layers are grown on Si.

2.6.1 Seeding layer

GaN growth on heterosubstrates, e.g. Si, needs to start with a nucleation layer, called a seeding layer. The seeding layer plays a significant role in achieving a high quality GaN layer on heterosubstrates minimizing crystal defects, e.g. threading dislocations detrimental for device performance as well as melt-back etching. The latter strong etching effect is a chemical reaction of gallium with silicon at high growth temperatures during GaN deposition, which results in a degradation of the GaN layer and the Si substrate. In extreme cases, the formation of deep holes in Si substrates can happen including SiN and SiGaN alloy formation [Sunkara 2001, Krost 2002, Ishikawa 2008]. The surface and cross sectional images of a melt-back etched sample of GaN grown on Si(113) are shown in Figs. 2.12 (a) and (b), respectively. It was observed that cracking can also initiate melt-back etching. In GaN layer, cracks can occur as a very thick GaN layer is growing or after cooling down to InGaN growth temperatures. An AlN seeding layer is one of the best ways to prevent the melt-back etching reaction. Since the Al-N bonding energy is very high, the formation of metallic aluminum is suppressed during AlN seeding layer growth [Dadgar 2010]. A compact AlN seeding layer having a

smooth surface without pits and cracks helps to protect the Si surface from diffusion of Ga atoms at the Si substrate surface and by this protects the substrate from the melt-back etching reaction. When the AlN seeding layer does not fully cover the Si substrate, it is observed that melt-back etching increases during GaN growth with a high TMGa-flow rate at higher temperatures. Therefore, to protect the melt back etching during GaN grown on Si, the following factors are significant: smooth AlN surface without any craters, pits and cracks; the AlN seeding layer thickness; the growth temperature and thickness of the subsequent GaN layers.

The Al pre-deposition was also performed to avoid SiN formation and an amorphous structure of AlN seeding layer [Dadgar 2000b, Krost 2002]. It is carried out by TMAl pre-flow into the reactor prior to flowing NH3 [Chen 2001, Kwon 2002, Dadgar 2003, Clames 2006].
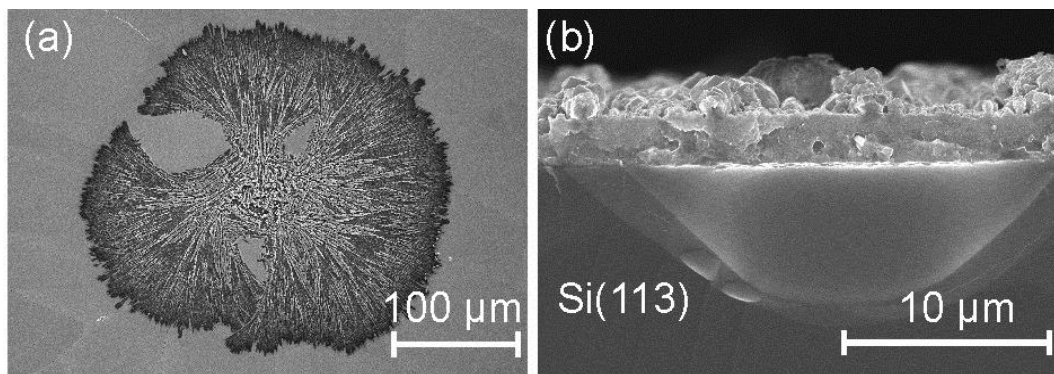

Fig. 2.12: *FE-SEM images of melt-back etching effect (a) top view, (b) cross section.*

2.6.2 Stacking faults

Stacking faults, which are one of the main types of two-dimensional defects in epitaxial group III nitrides, occur if the normal periodic sequence of layers is changed. Stacking faults occur on the basal-plane and are then called basal-plane stacking faults (BSFs). Stacking faults occurring on planes other than basal-planes are called prismatic stacking faults (PSFs) [Drum 1965].

On a-plane GaN grown on a 4H-SiC substrate with an AlN buffer layer, it was observed that the basal and prismatic stacking faults together with Frank ($\vec{b} = \frac{1}{2}\langle 0002 \rangle$) and

Shockley $\vec{b}=1/3\langle 10\bar{1}0\rangle$ partial dislocations were the main defects in GaN layers [Zakharov 2005].

BSFs in wurtzitic structures can be considered as planar defects, which form a local cubic…AaBbCc… stacking sequence in the ideal hexagonal …AaBbAaBb… stacking sequence in the [0001] direction. Four different forms of BSFs can be distinguished and are shown in Fig. 2.13: (a) intrinsic I_1-type BSF with …AaBbCcBbCc… stacking sequence, which has the lowest formation energy [Stampfl 1998]. Such a fault is bound by a Frank-Shockley dislocation with Burgers-vector $\vec{b}=1/6\langle 20\bar{2}3\rangle$. This vector has a $\frac{1}{2}\langle 0002\rangle$ component and a $1/3\langle 10\bar{1}0\rangle$ component (Appendix Fig 3).
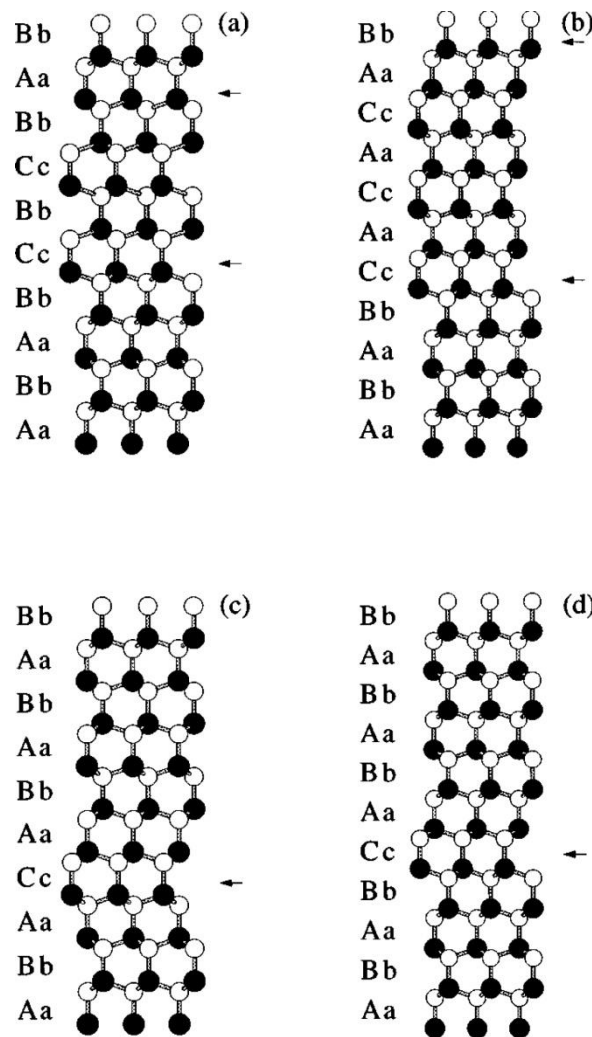

Fig. 2.13: *Types of stacking faults. (a) I_1-type BSF, (b) I_2-type BSF, (c) I_3-type BSF, (d) E-type BSF. White and black circles indicate anions and cations, respectively. Arrows show the stacking fault position [Stampfl 1998].*

(b) Intrinsic I_2-type BSFs (…AaBbCcAaCc…), which can be formed by a $1/3\langle 1\bar{1}00\rangle$ shear of one part of a crystal regarding the other part. This fault has the next lowest formation energy [Stampfl 1998]. This BSF is bound by a perfect dislocation with a Burgers-vector $\vec{b} = 1/3\langle 11\bar{2}0\rangle$, which is energetically more favorable for dissociating into two Shockley partial dislocations with Burgers-vector $\vec{b} = 1/3\langle 1\bar{1}00\rangle$.

(c) Intrinsic I_3-type BSFs (…AaBbAaCcAaBb…) stacking faults in which one of the Aa or Bb layers has a "wrong" occupation in the Cc position. This type of fault has the second-lowest formation energy and was theoretically presented by Stampfl and Van de Walle [Stampfl 1998].

A stacking fault is called intrinsic if the two different lattice patterns are continued up to the fault surface [Drum 1964]. But in the case of extrinsic stacking faults an extra layer is inserted.

(d) Extrinsic stacking faults (also called E-type) [Hull 1984]. These stacking faults occur if an extra Cc layer is inserted in the midst of the normal stacking sequence (…AaBbCcAaBb…). This E-tpye fault has high formation energy and is bound by Frank partials with Burgers-vector $\frac{1}{2}\langle 0002\rangle$ [Zakharov 2005].

Stacking faults formation energies per unit cell area are given in Table 2.4. Please see reference [Stampfl 1998] for more details about energies calculation.

Table 2.4: *Stacking faults formation energies per unit cell area (in meV) [Stampfl 1998].*

	Type I	Type II	Type III	Extrinsic
GaN	10	24	19	38
InN	19	44	36	65
AlN	49	103	97	150

2.7 X-ray measurements

X-ray diffraction measurement is a nondestructive method for sample investigation giving fast and precise information. Here, the basic principles of X-ray radiation and diffractometers are summarized. X-rays are transverse electromagnetic radiation and have approximately the same velocity as visible light in a vacuum. X-rays consist of much shorter

wavelengths namely from 0.001 nm to 10 nm. X-radiation is called Röntgen radiation, after Wilhelm Conrad Röntgen, who is generally credited as its discoverer, and he called it X-rays representing an unknown type of radiation.

A typical simple diffractometer comprises an X-ray tube, in some cases a monochromator to choose the wavelength, slits to adjust the shape of the beam, a sample holder, a detector and a goniometer to adjust sample and detector positions. More information can be found in [Spieß 2005, Klug 1974].

2.7.1 Scattering of X-ray radiation

Interaction of X-ray radiation with the lattice in a crystal leads to a scattering process. Elastic scattering results when there is no change in wavelength of the incident beam and scattered radiation, in which certain geometrical conditions i.e. Bragg law in other words Laue equations, are satisfied.

Bragg's Law

W. L. Bragg explained X-ray diffraction effects considering a "reflection" analogy in 1912. He considered a selective reflection from a stack of parallel (hkl) atomic planes with a constant interplanar spacing d_{hkl}. If this crystal is irradiated by a monochromatic X-ray radiation of wavelength λ, in terms of Bragg the phenomenon is not a surface reflection, as with ordinary light. Since the X-ray radiation is high-energy radiation, it also penetrates into the crystal (a depth of several million layers) before being significantly absorbed. In the case of a constructive interference, all planes in the series that are not too deep in the crystal will be involved in the reflection. Fig. 2.14 (a) shows these Bragg's consideration and analytical derivation of the Bragg equation. If the path difference of the reflected beam 1 and 2 is a whole number of wavelength λ, Bragg's condition occurs,

$$CB + BD = n \cdot \lambda. \qquad (8)$$

By simple trigonometry it can be written:

$$2 \, d_{hkl} \sin \theta_{hkl} = n \cdot \lambda \qquad (9)$$

where *n* is an integer number and θ_{hkl} is the Bragg angle (angle between the incident beam and lattice plane surface).

d_{hkl} for a hexagonal crystal system with Miller indices hkl is given by:

$$d_{hkl} = \frac{1}{\sqrt{\dfrac{4}{3}\left(\dfrac{h^2 + hk + k^2}{a^2}\right) + \dfrac{l^2}{c^2}}} \qquad (10)$$

where *a* and *c* are the a-plane and c-plane lattice constants, respectively.
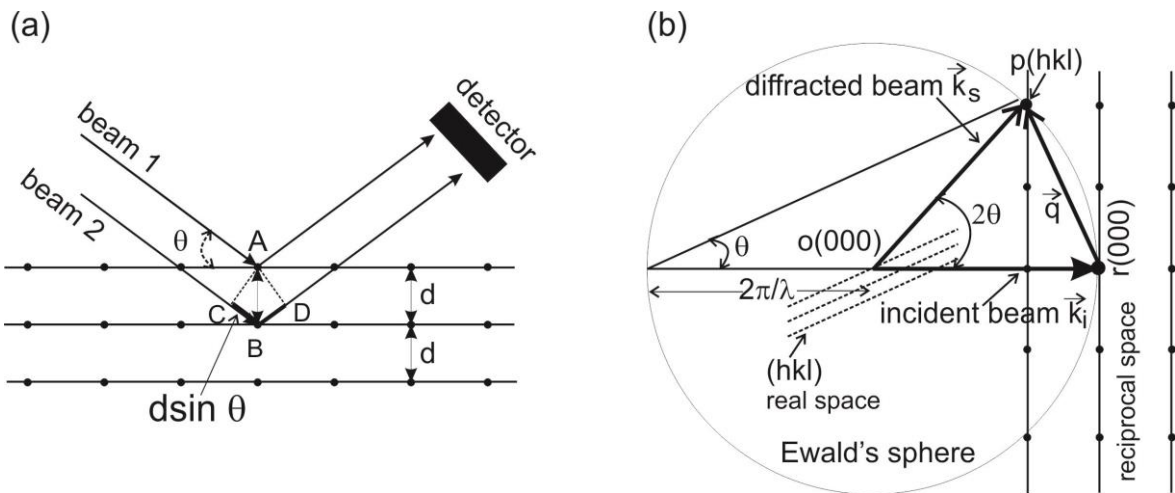

Fig. 2.14: *Geometry of the (a) Bragg reflection analogy, whereas Bragg's law is a construction in real space and (b) Ewald's geometric model.*

Equation 9 is a fundamental equation of X-ray diffraction and is known as Bragg's law. Laue equation can be interpreted in a vector form.

If $\vec{k}_i = \dfrac{2\pi}{\lambda_i}$, $\vec{k}_s = \dfrac{2\pi}{\lambda_s}$ are the wave vectors of the incident and diffracted beams, respectively, (in the case of elastic scattering $\rightarrow \lambda_i = \lambda_s \rightarrow \left|\vec{k}_i\right| = \left|\vec{k}_s\right|$), referring to the **Max von Laue interpretation** it can be written:

$$\vec{k}_s - \vec{k}_i = \vec{q}, \quad \vec{q} = \vec{K}, \qquad (11)$$

$\vec{q}$ is the scattering vector lying in the scattering plane perpendicular to (hkl)lattice planes as it divides the angle between incident and diffracted beams into two equal angles. $\vec{K}$ as a reciprocal lattice vector is a normal vector to the set of (hkl)lattice planes and $\left|\vec{K}\right| = 2\pi / d_{(hkl)}$.

A reciprocal space is an imaginary lattice of points that can be built from the real lattice place with $\vec{a}$, $\vec{b}$ and $\vec{c}$ as primitive translation vectors. Each point in a reciprocal space bears a reciprocal relation to a lattice plane in real space. The point (hkl) in the reciprocal space represents (hkl) plane in real space. The point (hkl) lies on the "normal vector" from the origin to the (hkl) plane and its distance from the origin is $\left|\vec{K}\right| = 2\pi / d_{(hkl)}$.

Fig. 2.14 (b) shows the description of Ewald's sphere, which is a geometric construction in reciprocal space. In general, in $\vec{k}_s - \vec{k}_i = \vec{q}$ equation, $\vec{q}$ can be considered as a vector belonging to Ewald's sphere with a radius of $2\pi/\lambda$. The sphere is centered at a point o(000) where crystal is situated and defined by the vector $-\vec{k}_i$. Note that the point r(000) is an origin of the reciprocal space and the $\vec{k}_i$ incident beam terminates on r(000), which at first can be arbitrarily selected. If a reciprocal point such as p(hkl), lies on the spherical surface, a scattered beam $\vec{k}_s$ is produced being the crystal plane in Bragg's position. $\vec{k}_s$ starts in the center of the sphere and passes through the point p(hkl).

2.7.2 Methods of X-ray diffraction measurements

In order to learn more about the fine structure of a sample, we can use several methods of X-ray diffraction experiments. One can obtain the significant information using X-ray diffraction experiments. It is clear that one experiment cannot deliver all the information with high accuracy. It is already known that accuracy and time are often diametrically opposed. Therefore it is extremely important to know the questions. That means what kind of information is desired. Then one can select both the measuring arrangement and measurement strategy.

The characterization of epitaxial layers is a crucial prerequisite for the optimization of growth parameters. Therefore, basic properties such as the crystallite orientations, their lattice parameters, mosaicity of crystal and its overall disorder, as observed in the peak widths have to be determined with reasonable accuracy. Lower mosaicity indicates better ordered crystals and hence better diffraction.

There are two important measuring geometries corresponding to the orientation of the (reflecting) lattice planes with the sample surface: symmetrical and asymmetrical scattering geometries. In symmetrical geometries the lattice planes are parallel to the sample surface. In the case of asymmetrical geometry the lattice planes are tilted by an angle φ with respect to the sample surface as shown in Fig. 2.15 (a). $\vec{k}_i$ and $\vec{k}_s$ show the incident and reflected wave vectors respectively. The $\vec{o}$ and $\vec{n}$ vectors show the surface normal and the "normal vectors" of lattice planes, respectively. $\omega_- = \vartheta - \varphi$ and $\omega_+ = \vartheta + \varphi$, where ϑ is the Bragg angle. In order to determine the structural properties of a sample depending on scattering geometry, one can use several scans in the reciprocal space as shown Fig. 2.15 (b). For θ/2θ scans, the X-ray tube is fixed, the sample moves by angle θ and at the same time the detector moves by angle 2θ. In this geometry the scattering vector $\vec{q}$ stays constant during the measuring perpendicular to the lattice planes. Using this technique, through changing of the absolute value of $\vec{q}$, a distribution of spacing of the lattice planes can be measured. Therefore the lattice constants can be determined.

In order to determine the crystal quality, e. g. tilt and twist, the ω-scans can be performed. In this geometry, the detectors positions are fixed while the sample is rotated by the ω–axis of the diffractometer. During the measurement, the angle between the incident beam and reflected beam (angle 2θ) is constant. Through alteration of $\vec{q}$ direction a distribution of the direction of lattice planes can be measured showing tilt or twist of crystallites depending on whether investigated planes are parallel or perpendicular to the sample surface.
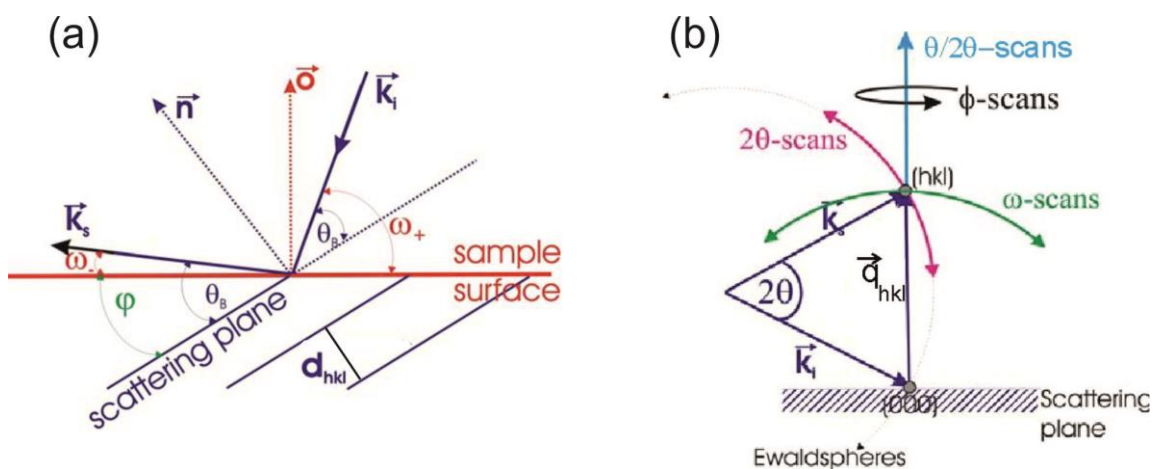

Fig. 2.15: *Schematic diagram (a) of the scattering geometry [Krost 1996], (b) of the measuring geometry of several scans [Reiher 2008].*

Since the crystal orientations of the most investigated samples in this work were unclear, **the Bragg Brentano measurement** was the best method of characterizing the samples. The quantitative analysis of the crystal orientation was investigated by X-ray $\theta/2\theta$ scans over a large angular range by means of a Siemens D5000 diffractometer in Bragg-Brentano geometry, whereas here a Cu ($K_{\alpha1} + K_{\alpha2}$) source with a variable aperture system and single graphite (0002) secondary monochromator was used. This arrangement is a focusing geometry, where the incident beams focusing point, the detector focusing point, and the sample surface lie on a focusing circle. As shown in Fig. 2.16, the focus of the X-ray tube and the detector lies on a goniometer circle, where the sample surface is located on its center. Here one can detect only diffractions from atomic planes in the crystal structure that are nearly parallel to the sample surface. The divergent incident beam leads to the scattering intensity increasing, because most crystallites with small values of tilt can contribute to the scattering.
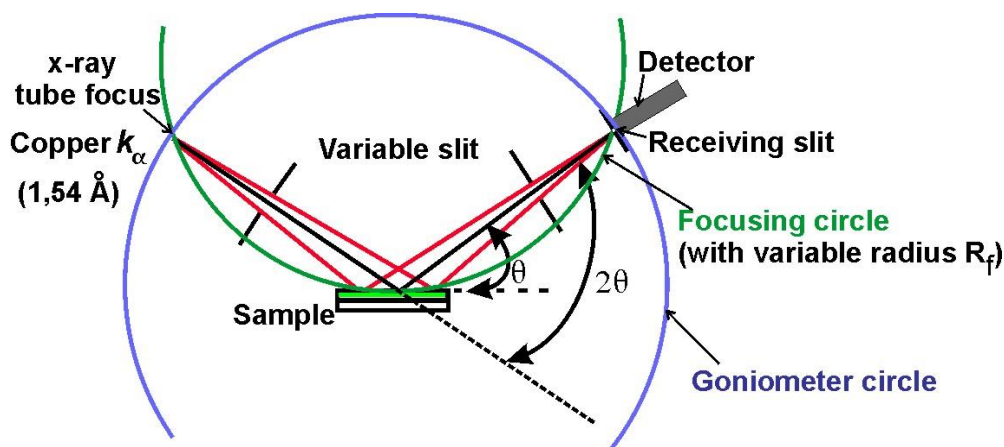

Fig. 2.16: *Schematic illustration of the Bragg Brentano geometry.*

X-ray pole figure measurement is a method of determining the crystallite texture, i. e. the orientation distribution over the whole half sphere. Here, measurements were performed by means of a URD6 + TZ6 diffractometer at the fixed scattering angles (2θ) related to a constant d spacing of lattice plans. The measurements consist of a series of φ-scans whereas φ is the angle of in-plane rotation around the center of the sample at different ψ-tilt angles as shown in Fig. 2.17 (b). The schematic diagram of an Eulerian cradle which can have a precise control of the tilt (ψ) and the rotation (φ) of the sample is shown in Fig. 2.17 (a). Pole figure measurement shows the number of texture components and their orientation with respect to the sample surface.
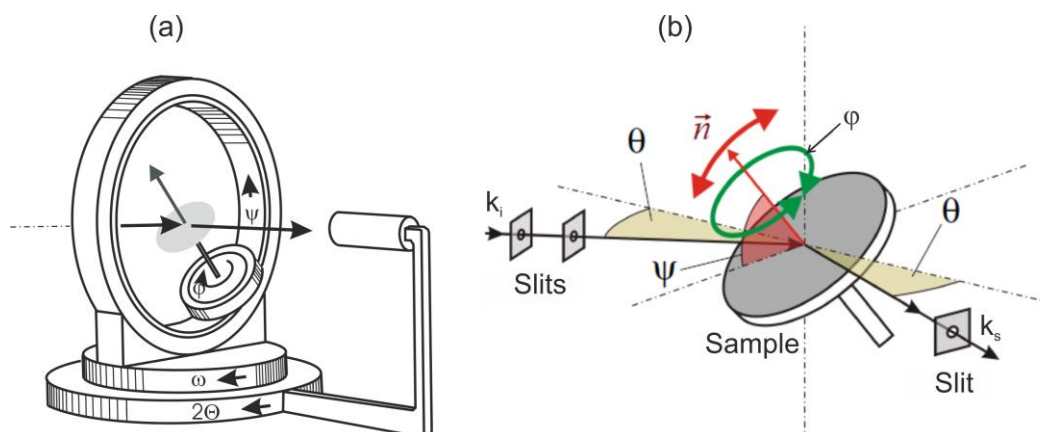
Fig. 2.17: *Schematic illustration of (a) Eulerian cradle, (b) a symmetric measuring of a pole figure showing relevant angles [Reiher 2008].*

Grazing incidence in-plane diffraction (GIID) is a method of measuring and characterizing the lattice planes, which are located perpendicular to the sample surface. Figs. 2.18 (a) and (b) show the top- and side-view of the measurement setup. Measurements were performed by means of a URD6 (Seifert FPM) diffractometer. The soller collimators are located in front of the X-ray tube and detector which parallelizes an X-ray beam resulting in a low axial divergence. The soller collimator consists of a series of highly absorbing metal plates. A grazing incident beam illuminates the sample surface with an incidence angle (α), which is smaller than the critical angle (0.3° to 0.4°) [Reiher 2008]) resulting in total reflection, because the refractive index of X-ray beams is smaller than 1 for all materials. The scattering beam is also observed at the same grazing angle as the incident beam (Fig. 2.18 (c)). Using this technique, the in-plane structure in the near surface region can be studied. $\theta/2\theta$-scans and ω–scans of the scattering planes can deliver the lattice constant of these planes and their in-plane rotation (twist) respectively.
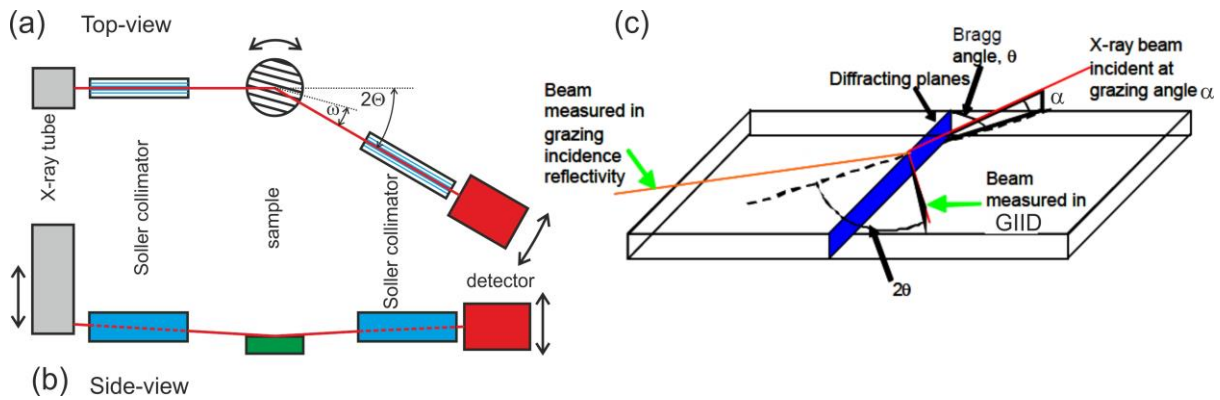
Fig. 2.18: *Schematic illustration of a measuring setup of GIID (a) top-view, (b) side-view [Wieneke 2008]. (c) Illustration of path of an incidence beam when it illuminates the surface at an angle smaller than the critical angle [Tanner 2004].*

Reciprocal space map (RSM) is an X-ray diffraction technique for determining the structural properties of thin film such as strain and relaxation. RSM is a two-dimensional measuring of the surrounding area of a scattering reflex in a reciprocal space. Using a position sensitive detector (PSD) for each ω-scan a series of 2θ–scans (from θ_1 to θ_2) can be detected. Measurements were performed by means of a URD6 (Seifert FPM) diffractometer with a PSD detector as shown in Fig. 2.19.
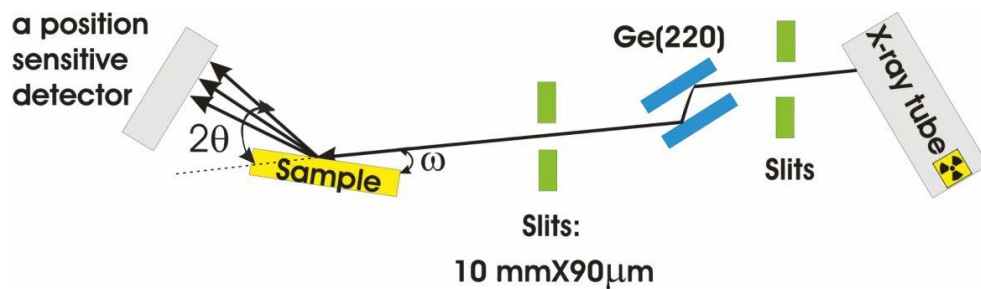

Fig. 2.19: *Schematic diagram of a Seifert URD6 diffractometer with a position sensitive detector [Saengkaew 2010].*

2.8 Other characterization techniques

Many important experimental methods of determining the properties of semiconductor materials are based on the interaction of these materials with photons or electrons. One can receive the structural information by means of the particular particle flux at the detector after reaction. In addition, specific material properties were examined in order to enable a targeted

layer optimization for the particular application. To determine the optical properties of layers, photo- and cathodeluminescence spectroscopy is performed. Additionally, scanning- and transmission electron microcopy are excellent investigation methods of determining the real structure of the samples e.g. surface and interface morphology.

2.8.1 Photo- and cathodoluminescence

Photoluminescence (PL) and cathodoluminescence (CL) measurements are important methods of determining the optical properties of semiconductor materials. In PL spectroscopy, electrons of a sample are excited by photons to a higher energy level state. In semiconductors, corresponding to an electron transition from the valence band into the conduction band, the electron–hole pair is generated and after a very short time (a few nanoseconds) they return to a lower energy state which is called recombination. A radiative recombination is accompanied by the emission of a photon. A non-radiative recombination process can also occur. Therefore the wavelength (energy) of the emission peak can determine several terms, e.g. the donor bond excitons (D^0,X)-, BSF-, PSF-, and donor-accepter-pair (DAP)-emissions, whereas the three latter terms characterize the defect emissions. A helium cryostat is applied to adjust the temperature in the range from 4 to 300 K. In CL-spectroscopy electrons are excited by an electron beam. For more information of the PL- and the CL-measurements and their system setup, refer to [Ivchenko 2005] and [Bertram 1999]. In chapters 3, 4 and 5 top-view and cross section images on investigated samples are shown and discussed.

2.8.2 Field emission-scanning electron microscopy

Scanning electron microcopy (SEM) is a direct method of determining the surface morphology and interface. This is most widely applied method. The most common detection mode in SEM is secondary electron imaging. Since low energy electrons are used in SEM and the free path of such electrons is a few atomic layers, SEM is useful for surface research. In field emission-scanning electron microscopy (FE-SEM) an electron beam is emitted using the cold emission guns applying a high electric field, but in typical SEM, an electron beam is emitted from an electron emitter equipped with a tungsten filament cathode using a thermionic mechanism. In this work, a Hitachi S4800 FE-SEM was used to determine sample surface morphology and the cross-section images showing layer thickness.

2.8.3 Transmission electron microscopy

Transmission electron microscopy (TEM) allows the direct imaging of structures by means of the electrons which are accelerated by a high voltage source (200 kV). The electrons are transmitted through a very thin specimen. The sample preparation steps are very time-consuming, resulting in an ultra-thin sample which is transparent to electron beam. TEM provides a high spatial resolution depending on the wavelength of electrons related to the acceleration voltage. Due to a high spatial resolution, characterization of structure in an atomic dimension is possible. Using TEM, one can characterize some structural defects such as stacking faults and dislocations in the crystal lattice in terms of their type, distribution and density.

Using CL measurements of prepared TEM samples within a scanning transmission electron microscope (STEM), the very high spatial resolution of the STEM can be used which produces a direct correlation between local luminescence and sample morphology. More details about STEM-CL can be found in reference [Gordon 2011]. In this work, investigation of the structural details related to their optical properties was performed by STEM-CL measurements and is shown in chapter 4.

3 Evaluation of Si substrate orientation for semi-polar GaN growth

In this chapter, results of investigations on the semi-polar GaN structures grown on different oriented Si substrates are presented. The chapter starts with a review of the results of MOVPE grown GaN on Si(100) and its off-oriented substrates, which were grown by F. Reiher [Reiher 2008]. These results motivated the usage of high index silicon substrates (Si(h10) and Si(11h)) for semi-polar GaN growth in this work. Afterwards, the impact of the AlN seeding layer growth parameters on the crystalline orientation of GaN on different Si substrates is presented.

3.1 Review of GaN grown on Si(100) and off-oriented Si(100)

F. Schulze et al. showed that when using a 40 nm thin low temperature (LT) AlN seeding layer (680 °C) followed by a threefold high temperature (HT)-GaN / LT-AlN interlayer, the GaN crystallites on exactly oriented Si(100) substrates are almost oriented with their $GaN(10\bar{1}2)$-planes parallel to the Si(100)-plane [Schulze 2004]. Pole figure measurements of the $GaN(0002)$ reflection are shown in Fig. 3.1. The image on the left hand side shows four maxima of the $GaN(0002)$ reflection with identical intensity when GaN are grown on exactly oriented Si(100), whereas each GaN-component has a c-axis tilt angle of ~ 43° with respect to the surface normal. The four main peaks indicate four preferred azimuthal alignments of the $(10\bar{1}2)$-plane oriented GaN crystallites. This effect can be described by the occurrence of a coincidence site lattice between $GaN(10\bar{1}2)$ and Si(100) surface atoms and their fourfold surface symmetry. One of these $GaN(10\bar{1}2)$ alignments can be preferred by using an off-oriented Si(100) substrate. As shown in Fig. 3.1, the intensity of one of the in-plane oriented $GaN(10\bar{1}2)$ reflections increases by enhancing the Si(100) surface miscut from 0° to 4°. However, a single crystalline and fully coalesced GaN-layer with this crystallographic orientation on Si(100) and Si(100) with miscut could not yet be obtained. More details of off-oriented Si(100) surface structures can be found in [Reiher 2008].

Si(h10), e.g. Si(410), is similar to off-oriented Si(100) towards the [110] direction with a miscut angle of 14.04°. Si(11h), e.g. Si(117), is Si(100) off-oriented towards the [111]

direction. The angle between the Si(117) surface plane and the Si(100) plane is 11.42°. Now the question is: is it possible to grow one component of semi-polar GaN structure on Si(h10) or Si(11h) and how large is the c-axis tilt angle of GaN layers with respect to the substrate surface normal vector?

The results of GaN structures grown on high index silicon substrates are presented in the following paragraphs.
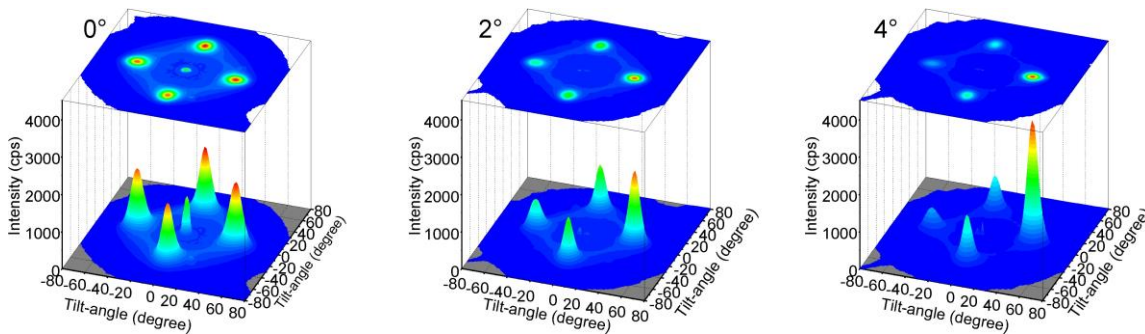

Fig. 3.1: *X-ray pole figure measurement of the GaN(0002) reflection grown on exactly and off-oriented Si(100) substrates with a miscut from 2° and 4° using a threefold HT-GaN / LT-AlN interlayer. The peak placed in (0,0) tilt-angle (in the image on the left hand side) shows a c-axis oriented GaN reflection [Reiher 2008].*

3.2 Polycrystalline semi-polar GaN on different high index Si substrates

To grow semi-polar GaN layers on silicon, first different oriented substrates were investigated to find suitable ones, which meet most of the necessary requirements. As known, Si(111) is a suitable Si orientation for growing c-axis oriented GaN layers because of the symmetry matching. As already mentioned in chapter 2, it is assumed that the GaN film is most likely grown on the Si(111) facets usually formed on the Si(11h) surface. Based on this assumption, a semi-polar GaN layer on Si(11h) can be obtained, if c-axis oriented GaN layers are grown on Si(111) facets, since Si(111) facets incline to Si(11h) surface. Therefore the c-axis tilt angle of the GaN structure depends on the Si(11h) orientation and increases from Si(112) to Si(117). Thus, GaN growth was preferably performed on Si(11h) with high h values to obtain a larger c-axis tilt angle reducing polarization fields along the growth direction. The GaN structures were grown on substrates with Si(115), Si(117), Si(100) and Si(100) with a miscut of 4.5° surface orientations, as well as on Si(111) substrates as reference. In order to investigate the impact of other Si surface structures, GaN was already grown on Si(410). Si(410) surface has a twofold symmetry.

GaN growth on heterosubstrates, such as Si, needs to start with a seeding layer. As mentioned in chapter 2, AlN seeding layer is one of the best ways of preventing melt-back etching.

To obtain semi-polar GaN with a larger c-axis tilt angle to improve the GaN quality, the seeding layer has to be optimized first. By varying the AlN seeding layer growth parameters, e.g. thickness (growth time), TMAl-flow rate, the impact of the seeding layer growth parameters on the GaN structures was investigated. Since a high temperature AlN seeding layer leads to a c-axis oriented GaN structure, in this work, all semi-polar GaN layers were grown with low temperature AlN seeding layers.

In order to investigate the impact of the substrate orientation on the GaN layer properties, GaN growth was performed on 3 or 4 different Si substrate orientations under the same growth conditions. To grow GaN on four different orientations simultaneously, each 2"-wafer was cut into 4 pieces. Finally, four or three different oriented pieces were loaded into the reactor for each experiment. Si(111) was almost always used as a reference sample. The typical sample structure was as follows:

A LT-AlN seeding layer was grown at 100 mbar and a TMAl flow rate of 8.6 µmol/min (20 sccm). The predeposition of around a monolayer of Al prior to the AlN seeding layer growth was performed. The next layer was followed by a threefold HT-GaN / LT-AlN (~ 160 nm / ~ 8 nm) interlayer sequence. For these layers, GaN and AlN were grown at 1145 °C and 630 °C, respectively. On top of this buffer, the main GaN layer was grown at 1145 °C and 200 mbar with a TMGa flow rate of 48.4 µmol/min for 15 minutes which relates to a nominal thickness of 600 nm. The sample structure is shown in Fig. 3.2.

In the following sections the results of sample investigations by means of X-Ray Bragg-Brentano and pole figure measurements are presented.
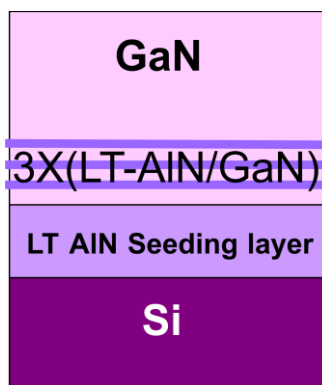

Fig 3.2: *Typical sample structure for buffer optimization. See appendix Tables 1,2,2,4,5 for detailed growth conditions.*

To investigate the effect of AlN seeding layer thickness on the GaN crystallite orientation and in particular their c-axis tilt angle inclination with respect to the surface

normal vector, samples (series α) were grown with different LT-AlN seeding layer (680 °C) growth times from 2 min to 26 min related to the nominal thickness from ~ 8 nm to ~ 104 nm (Fig. 3.2). All samples were grown with a nominal GaN layer thickness of 600 nm (15 min) on top. Fig. 3.3 shows the normalized intensity of different GaN reflections depending of the LT-AlN seeding layer thickness on Si(117). The angle between Si(117) and Si(111) is 43.3° (Carine). Thus a c-axis inclination angle of ~ 43.3° is expected. The results of Bragg-Brentano measurements show that the indicated reflections of the GaN crystallites change from $(10\bar{1}2)$ and $(10\bar{1}3)$ to $(10\bar{1}1)$ reflections by increasing the thickness of the LT-AlN seeding layer (Table 2.2 presents angles between the $\{0001\}$ plane and $\{10\bar{1}l\}$-planes). Here it is also found that very few crystallites were grown with their c-axis perpendicular to the surface.
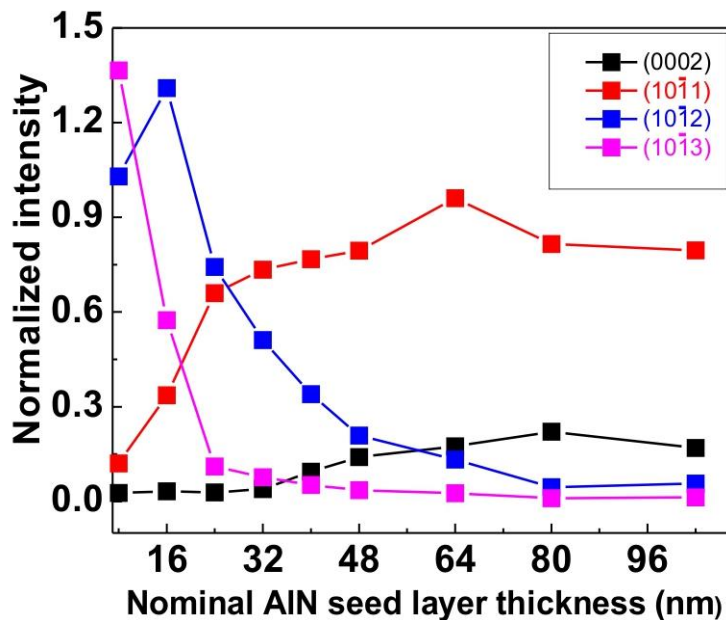

Fig. 3.3: *Normalized intensity of GaN reflections by changing a nominal AlN seeding layer thickness from ~ 8 nm to ~ 104 nm related to the growth time (from 2 min to 26 min) at Al-flux of 20 sccm. All samples were grown on Si(117) and investigated in Bragg-Brentano geometry. Intensity is normalized to the total measured intensity and the theoretical intensity of the powder-sample (Appendix Fig.4).*

Pole figure measurements of samples with a variation of the LT-AlN seeding layer thickness from (~ 8 nm to ~ 104 nm) were performed to determine the distribution of the GaN crystallite orientation over the whole half sphere. In Fig. 3.4, pole figure measurements of the GaN(0002) reflection grown on Si(117) are shown. Four maxima are observed, if the LT-AlN seeding layer thickness amounts to ~ 8 nm and only one of these is dominant in intensity. It is

found that the GaN maxima are asymmetrically located around the center of the circle. The number of GaN components remains constant up to a 6 min AlN growth time (~ 24 nm), but it increases from four to six GaN components when a thicker LT-AlN seeding layer is grown. Thus the number of GaN components depends on the LT-AlN seeding layer thickness. In the case of a thicker ~ 104 nm (26 min) LT-AlN seeding layer growth, nearly fiber textured GaN structures are indicated. It can be concluded that a thicker LT-AlN seeding layer leads to a higher degree of a random polycrystalline AlN structure in the seeding layer resulting in an increasing polycrystallinity of the GaN layer on top. It is also observed that the tilt-angle of the GaN c-axis increases when the LT-AlN seeding layer thickness is increased (Fig. 3.6). Thus, the probability of crystallite orientation transfer from the substrate to the GaN layer become less and less if thicker AlN seeding layers are applied. The symmetry of substrate surface can affect the crystallite orientation of GaN layers if a thin seeding layer is applied.

In order to prove that all maxima of the pole figure measurements are real GaN components, a simulation using the MULTEX software package was performed [Bettels 2011].
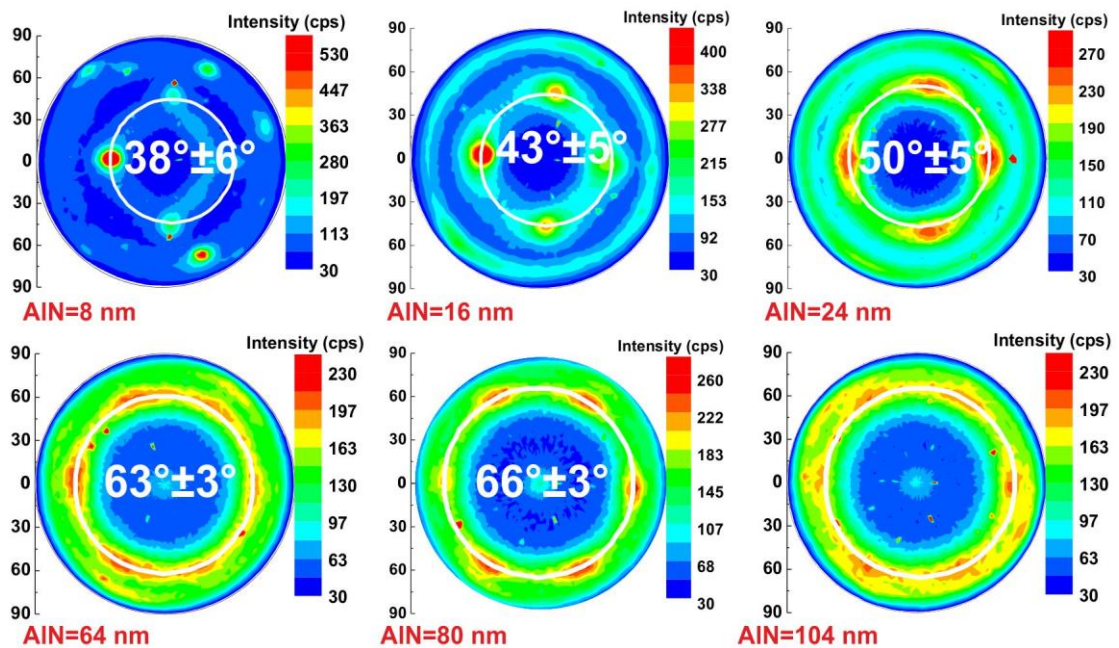

Fig. 3.4: *X-ray pole figure measurements of the GaN(0002) reflection grown on Si(117) with variations of the nominal LT-AlN seeding layer thickness from 8 nm to 104 nm corresponding to 8 min to 26 min growth time.*
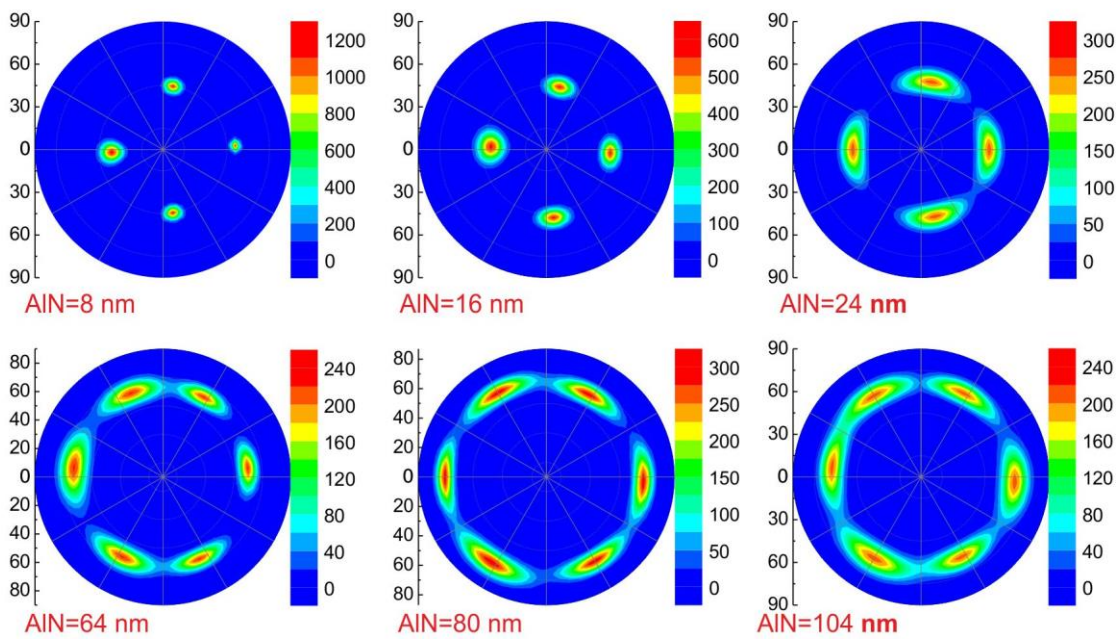
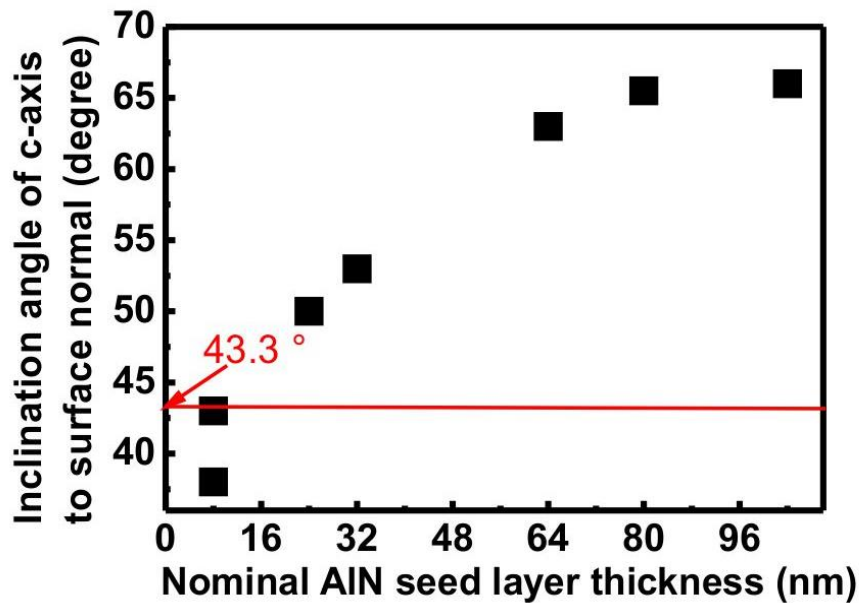**Fig. 3.5:** *Simulation of pole figures of GaN grown on Si(117).*

Fig. 3.6: *Inclination angles of the GaN c-axis with respect to the surface normal vector as a function of the LT-AlN seeding layer thickness grown on Si(117). The red line shows the position of the expected c-axis inclination angle if Si(117) is used.*

In Fig. 3.5, theoretical simulations of pole figures of GaN grown on Si(117) are shown, giving reasonable agreement with experimental results from Fig. 3.4. Each measured maxima indicates one GaN component.

Investigations of the surface morphology using Nomarski optical microscopy showed a very rough surface [Fig. 3.7]. In FE-SEM measurements an almost random distribution of orientations of the GaN crystallites for nearly all samples was observed. In contrast to that for GaN grown on Si(111), a smooth surface having a c-axis oriented GaN was obtained.
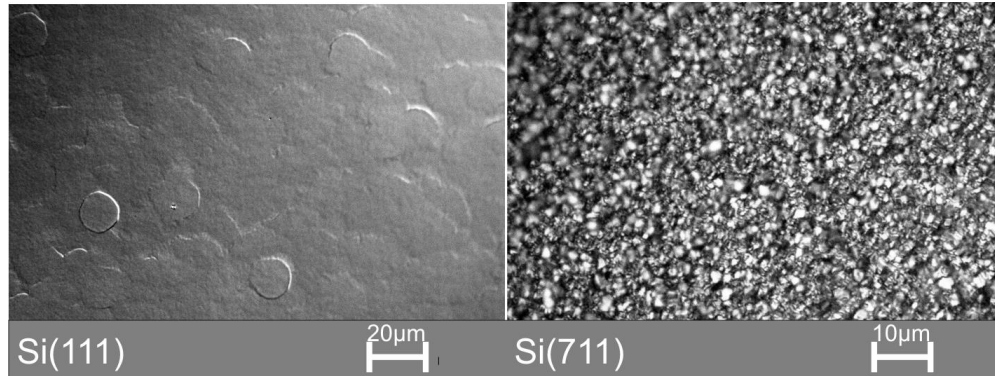

Fig. 3.7: *Nomarski images of GaN grown on Si(111) and Si(117) with 4 min LT-AlN seeding layer growth (16 nm). A smooth surface of the c-axis oriented GaN crystal can be seen on Si(111) compared to a rough surface of GaN grown on Si(117) (Appendix Fig 1 and Fig 2).*

It is expected that Si(111) terraces of Si(117) surface can be used to obtain a semi-polar GaN layer. The experimental results show that GaN structures are polycrystalline with a rough surface. As showed in Table 2.3, the Si(111) plane fraction of the Si(117) surface is 21%. Thus, it is challenging to obtain a smooth surface by using Si(117) as a substrate, because in comparison to the Si(111) terraces the Si(100) terraces are more and more dominating.

As already mentioned, GaN was simultaneously grown on different Si substrate orientations, e.g. Si(410) and Si(117). Si(410) and Si(117) are off-oriented Si(100) towards [110] and [111] directions, respectively having different surface structures and symmetries. Unfortunately, the surface structures of used substrates under their growth conditions are unknown. In series β of GaN samples grown on Si(410), the dependence of the GaN crystalline orientation in terms of the LT-AlN seeding layer thickness (~ 8 nm to ~ 64 nm, growth time: 2 min to 16 min) was investigated. Polycrystalline GaN structures are also observed as a result of Bragg-Brentano measurements.

Pole figure investigations were performed to study the orientation of the GaN crystallites grown on Si(410), as shown in Fig. 3.8. Two maxima are observed, in both cases, if the LT-AlN seeding layer thicknesses are ~ 8 nm (2 min) and ~ 16 nm (4 min). For a nominal LT-AlN seeding layer thickness of 24 nm (6 min) four maxima are indicated as for

Si(117), whereas their in-plane position is dependent on the Si surface orientations and their symmetries. In the case of thicker LT-AlN seeding layers, the number of maxima increases. It is indicated that the tilt-angle of the GaN c-axis depends on the thickness of the LT-AlN seeding layer and increases with increasing the seeding layer thickness. In Fig. 3.9 pole figures of three different Bragg reflections (left: $(10\bar{1}1)$, center: $(10\bar{1}2)$, right: $(10\bar{1}3)$) of the GaN sample with 2 min LT-AlN seeding layer growth (~ 8 nm) on a Si(410) substrate are shown. The angles between the (0002)-plane and $(10\bar{1}1)$-, $(10\bar{1}2)$-, $(10\bar{1}3)$-planes are ~ 62°, 43°, 32°, respectively. A simulation of pole figures of GaN different reflections grown on Si(410) with the seeding layer thickness of ~ 8 nm is presented in Fig. 3.10 (down) showing a good agreement with experimental results. The pictures in Fig. 3.10 are rotated by 180° compared to those in Fig.3.8 and Fig. 3.9.
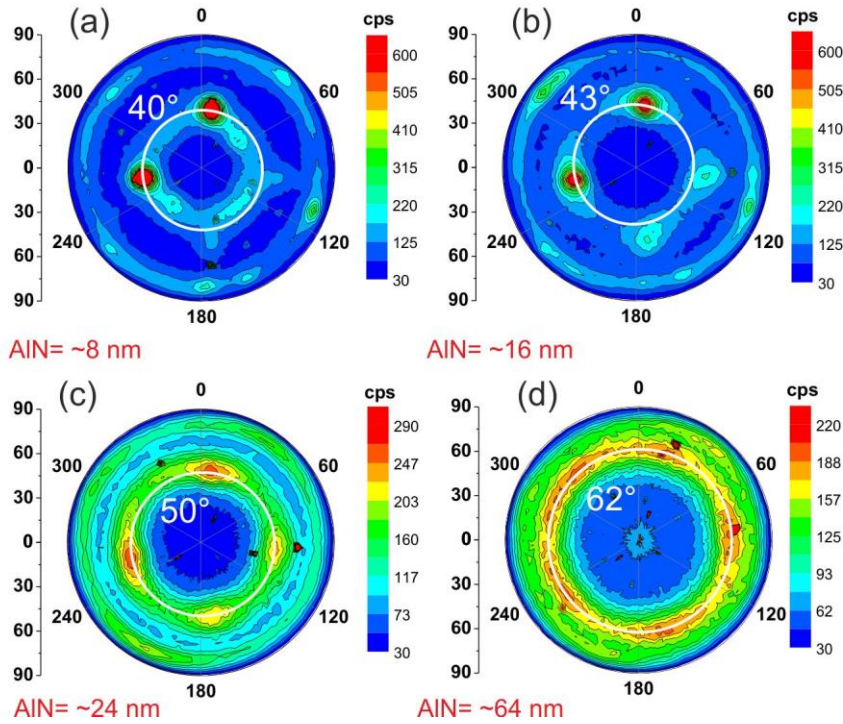

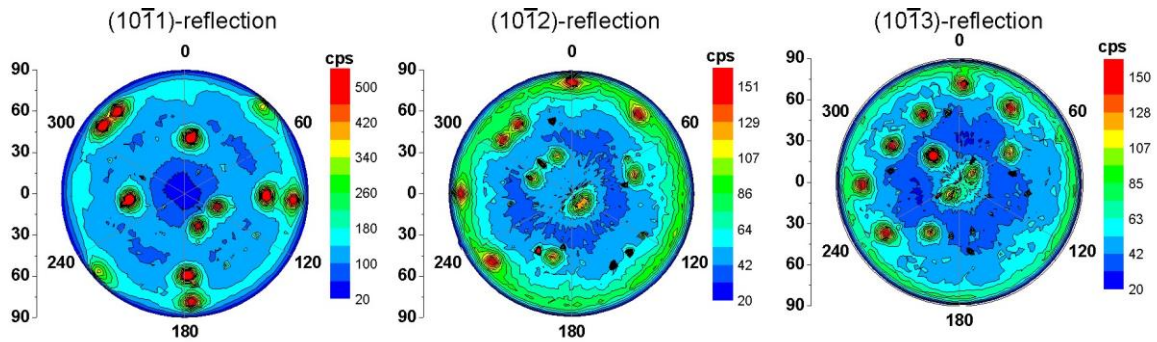**Fig. 3.8:** *X-ray pole figures of the GaN (0002) reflection grown on Si(410) with the LT-AlN seeding layer thickness increased.*

Fig. 3.9: *Pole figures of three different Bragg reflections (left:* $(10\bar{1}1)$*, center:* $(10\bar{1}2)$*, right:* $(10\bar{1}3)$*, of the GaN sample grown with 2 min (~ 8 nm) LT-AlN seeding layer on Si(410) substrate.*
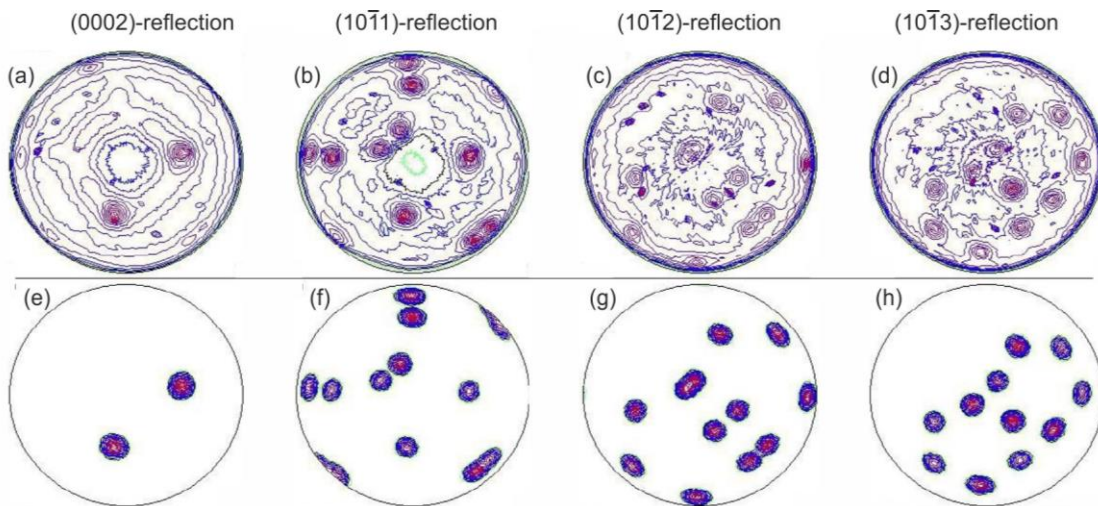

Fig. 3.10: *Pole figures of four different Bragg reflections (above) and their simulations (down) of the GaN sample grown with 2 min (~ 8 nm) LT-AlN seeding layer on Si(410) substrate. ((a, e): (0002) reflection, (b, f):* $(10\bar{1}1)$ *reflection, (c, g):* $(10\bar{1}2)$ *reflection, (d, h):* $(10\bar{1}3)$ *reflection)*

By applying a thick LT-AlN seeding layer, the preferred orientations (texture) of the GaN crystallites is nearly independent of the silicon surface orientation, which is observed for different Si orientations with different surface structures and symmetries. It can be concluded that the transfer of the substrate surface orientation, namely the Si(111) surface facet orientation, to the GaN layer becomes less probable, if thicker LT-AlN seeding layers are applied. The Si surface symmetry can be transferred onto the GaN using a thin LT-AlN seeding layer.

3.2.2 Impact of Si orientation on the AlN and GaN crystalline orientation

In order to grow a c-axis oriented GaN layer on Si(111) free from melt-back etching the required minimum thickness of the LT-AlN seeding layer is about 40 nm [Reiher 2008]. In the following section the nominal thickness of the LT-AlN seeding layer is ~ 40 nm corresponding to a growth time of 10 min. To investigate the effect of the Si-substrate orientation on the orientation of the AlN and GaN crystallites in each layer, three types of samples (series χ, δ, ε) structures were grown. Si(117), Si(410), Si(100), and 4.5° off-oriented Si(100) were used as substrates.

Series χ consists of a LT-AlN seeding layer (~ 40 nm, 680 °C) with 10 s Al predeposition (~ one monolayer Al). Series δ contains the same LT-AlN seeding layer (~ 40 nm with ~ one monolayer Al) followed by a threefold HT-GaN / LT-AlN (~ 160 nm / ~ 8 nm) layer sequence. The total thickness of these HT-GaN / LT-AlN interlayers varied from a few nm to a maximum value of ~ 500 nm. Series ε has also among other layers (Al predeposition, LT-AlN seed layer and threefold HT-GaN / LT-AlN interlayers) a nominally 600 nm thick GaN (15 min) top layer. Samples were grown under nearly the same growth parameters as mentioned in section 3.2.

The results of θ/2θ scans in Bragg-Brentano geometry for the samples series χ on different Si substrates show that AlN crystallites were grown nearly independently of the Si substrates orientation and the AlN crystallites were grown as $(10\bar{1}0)$, (0002) and $(10\bar{1}1)$ AlN-planes (Fig. 3.11, left).

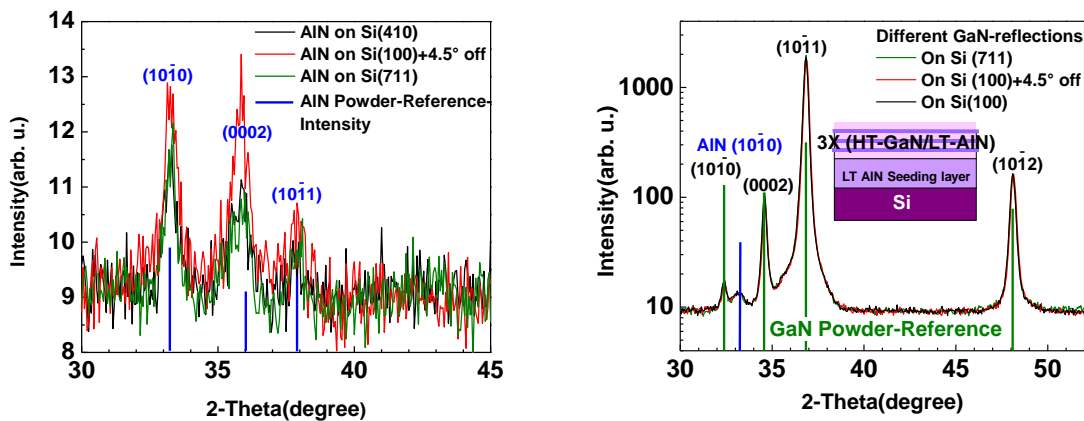**Fig. 3.11:** *Left: Bragg-Brentano θ/2θ scans of AlN layers grown on different substrates, e. g. Si(100) with 4.5° miscut, Si(117), and Si(410). Right: Bragg Brentano θ/2θ scans of HT-GaN / LT-AlN layers grown on Si(100), Si(100) with 4.5° miscut, and Si(117). Here the AlN $(10\bar{1}0)$ reflection is clearly visible. The inset shows the sample structure.*

The existence of several AlN reflections shows textured polycrystalline AlN structures because the ratio of the intensities of the measured AlN-reflections is not the same as that of AlN powder-reference-intensity.

In series δ, the impact of the substrate orientation on the HT-GaN / LT-AlN interlayer was studied. As shown in Fig. 3.11, right, nearly identical Bragg reflections of GaN with nearly the same intensity for different Si substrate orientations were observed. Thus, the GaN crystallites were grown independently of the individual substrate orientation. The preferred GaN growth plane with the highest intensity compared to the other planes is $(10\bar{1}1)$. It is found that GaN structures did not follow the LT-AlN seeding layer texture when a thick (~ 40 nm) polycrystalline LT-AlN seeding layer is applied.

FE-SEM top view images of some of these samples are shown in Fig. 3.12. The left picture shows the surface morphology of a sample of the series χ grown on Si(117). The surface morphology of the LT-AlN seeding layer shows the crystal platelets in different orientations. Such structures have been shown for a LT-AlN (700 °C) seeding layer grown on Si(111) [Saengkaew 2010]. The surface morphology of a sample from series δ grown on Si(117) is shown in Fig. 3.12, center. GaN crystallites show a randomly oriented structure on the sample surface with a size from a few nanometers to several micrometers. Fig. 3.12, right shows an image of the GaN structure with a nominal thickness of 600 nm (15 min) deposited at 1145 °C on top of the threefold (HT-GaN / LT-AlN) layer stack on a LT-AlN seeding layer. A long growth time of GaN shows bigger crystallite sizes but a non-coalesced surface.
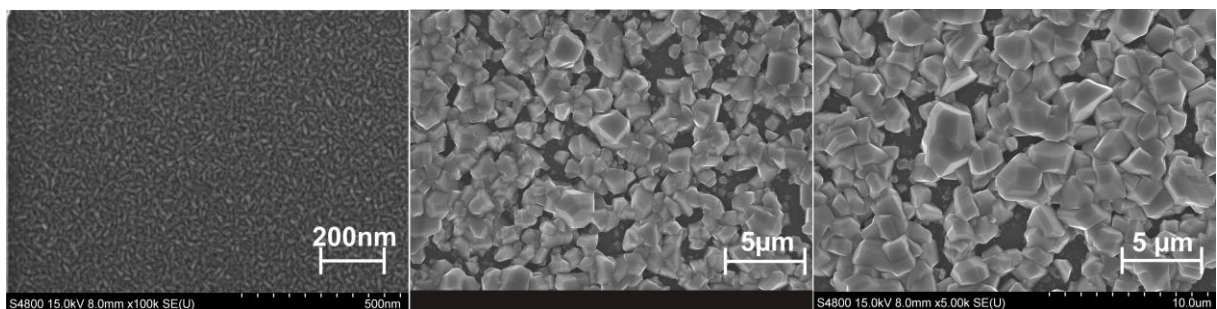

Fig. 3.12: *FE-SEM top view images of (left) LT-AlN seeding layer, (center) GaN (~ 500 nm thickness as total structures) and (right) GaN (~ 1100 nm thickness as total structures). All samples were grown on Si(117).*

3.2.3 Impact of TMAl-flow rate on AlN seed layer and GaN layer

In this section, the impact of the growth velocity of the LT-AlN seeding layer on a texture of the GaN structure is discussed. The growth velocity of the LT-AlN seeding layer relates to the TMAl-flow rate. Samples were grown with thin and thick LT-AlN seeding layers. The thickness of the LT-AlN seeding layers varied from ~ 4 nm to ~ 120 nm. Here, first results of GaN structures on Si(115) and Si(117) will be presented and then compared to results obtained on Si(112).

As mentioned in section 3.2.1, the orientation investigation of GaN crystallites, applying a thin (8 nm) LT-AlN seeding layer with a low TMAl-flow rate (20 sccm) on high index Si shows four $GaN(0002)$ crystal orientations with the c-axis inclination related to the inclination of the Si(111) plane of the substrate surface versus the surface normal. By increasing the LT-AlN seeding layer thickness, the c-axis inclination angle and the number of $GaN(0002)$ diffraction spots are increased.

A thick LT-AlN seeding layer can be obtained in two ways, either by increasing the growth time at an identical growth rate or using a higher TMAl-flow rate (higher growth rate). In the next step, the TMAl-flow rate was increased from 20 to 80 sccm. By using a faster growth rate and also thicker LT-AlN seeding layer (20 min, ~ 120 nm at 80 sccm) in series ϕ, variations of the GaN crystallites orientation are found as shown in Fig. 3.13.
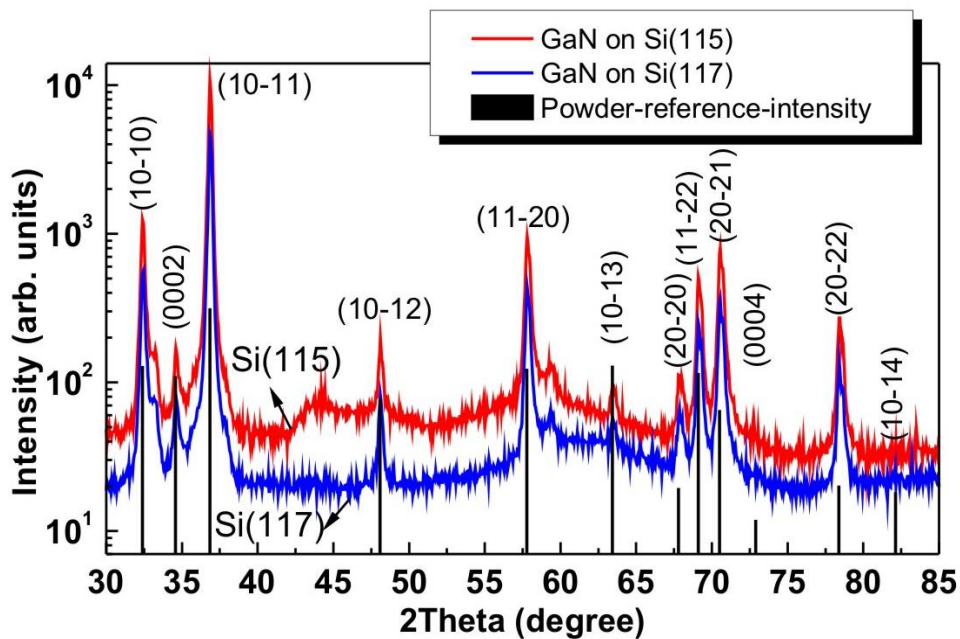

Fig. 3.13: *Bragg-Brentano θ/2θ scans of GaN on Si(115) and Si(117) with the Miller indices (hkil) of the GaN planes.*

It indicates that the orientation of GaN structures on Si(115) and Si(117) is nearly the same but in comparison to samples grown with a LT-AlN seeding layer grown at a low TMAl-flow rate and lower thickness the intensity of the (0002) GaN oriented crystallites is lower and the intensity of the $(10\overline{1}1)$ oriented GaN crystallites is higher.

The pole figure measurements of samples (series ϕ) grown on Si(115) and Si(117) are shown in Fig. 3.14. Here, the ring-shaped intensity maxima show that fiber-textured GaN structures were grown.

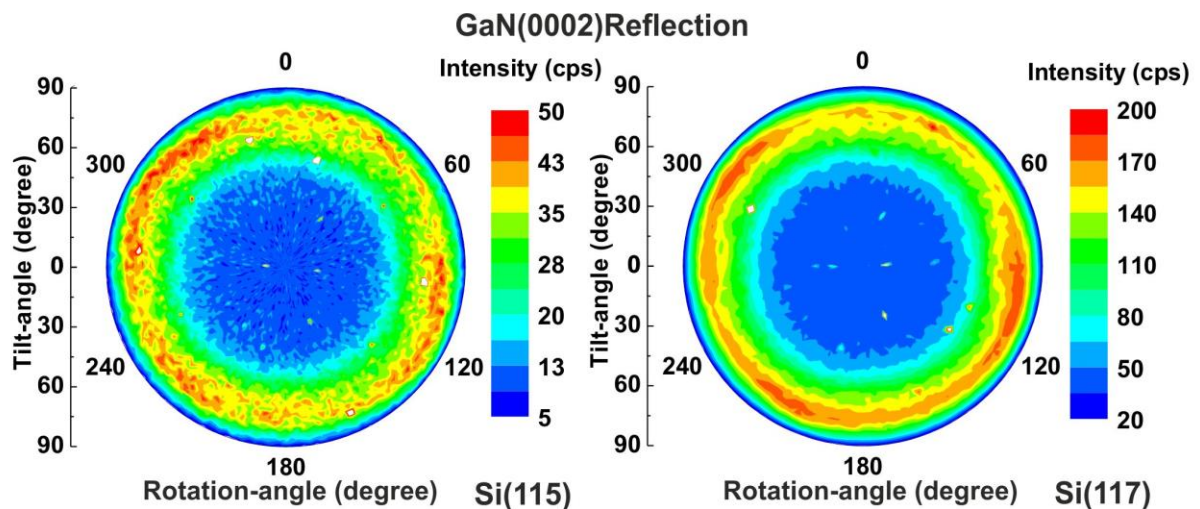**Fig. 3.14:** *X-ray pole figure measurements of the GaN(0002) reflection of a layer grown with the same growth parameter on Si(115) (left) and on Si(117) (right).*

Up to now, the GaN layers grown on different Si orientations (excepting Si(111)) showed nearly the same GaN textures when a thicker LT-AlN seeding layer was applied. The GaN structures are polycrystalline with a rough and non-coalesced surface. In the case of using Si(11h) with higher h value, the effect could be explained with a fraction of the Si(111) planes on Si(11h), which is smaller than that on Si(11h), e.g. Si(112) und Si(113). In the following section the results of GaN layer grown on Si(112) direction will be presented and discussed.

In Fig. 3.15, the $\theta/2\theta$ scan of GaN grown on Si(112) with an approximately identical LT-AlN seeding layer thickness ($\sim$ 110 nm) grown at high TMAl-flow rate (80 sccm) is shown (series γ). As shown, the GaN crystallites direction and their intensity do not have major differences when various high index Si substrates were applied. In contrast to that the pole figure measurement of the sample on Si(112) (Fig. 3.16) shows six distinguishable components of GaN(0002) compared to fiber-textured GaN structures (Fig. 3.14).
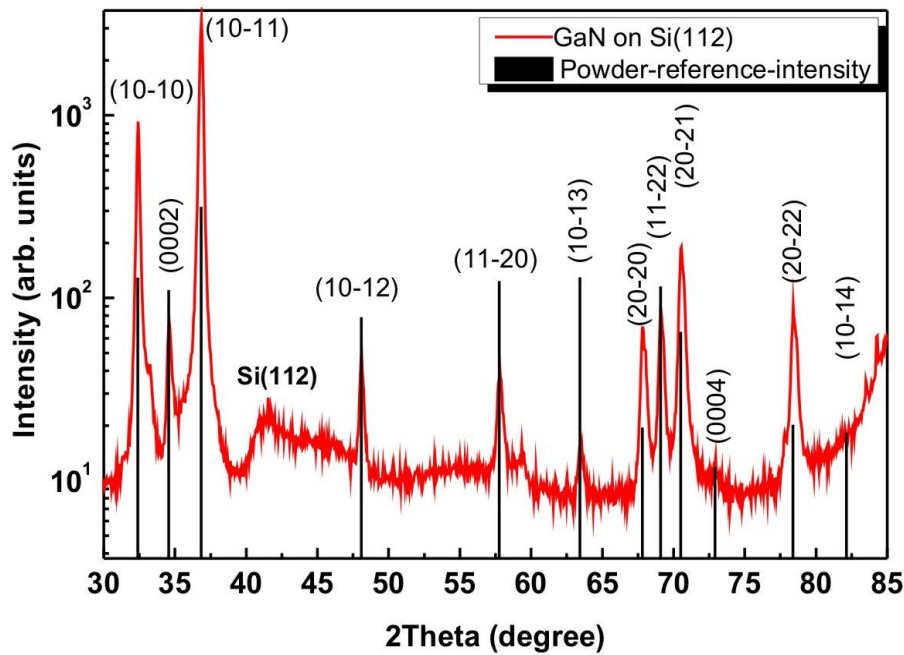
Fig. 3.15: *Bragg-Brentano θ/2θ scan of GaN on Si(112). The Miller indices (hkil) of indicated GaN planes are shown. The GaN$(10\bar{1}1)$ plane is grown as a preferred plane but the intensity of c-axis oriented GaN becomes much lower than for samples shown in Fig 3.13.*
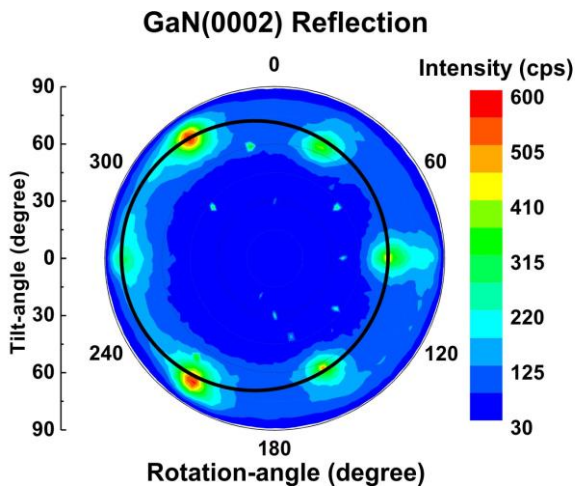
Fig. 3.16: *X-ray pole figure measurements of the GaN(0002) reflection of a layer grown with a LT-AlN seeding layer (~ 110 nm) at high growth rate (80 sccm) on Si(112). The tilt-angle is larger than 70°, however, the six different orientations hinder the growth of a continuous GaN layer.*

Applying a thick LT-AlN seeding layer makes the growth direction of the GaN crystallites nearly independent of the silicon surface orientation. The GaN$(10\bar{1}1)$ plane is grown as a preferred plane which was investigated for several Si substrate orientations (Si(117), Si(115), Si(112)). Here the lowest inclination from the Si(111) direction, namely Si(112), shows six well pronounced GaN(0002) reflections in pole figure measurements. One can assume that for Si orientations with small h values, thus a lower inclination angle from the Si(111) direction, GaN growth differs significantly from Si(11h) substrates with larger h

values when applying a thin LT-AlN seeding layer. To evaluate this in the next step, GaN layers were grown with a thin LT-AlN seeding layer with higher growth velocity on Si(112) and Si(117).

Bragg-Brentano θ/2θ scans and pole figures of GaN grown on a thin (15 s, ~ 4 nm) LT-AlN seeding layer with a high TMAl-flow rate (80 sccm) on Si(112) and Si(117) are shown in Figs. 3.17 and 3.18, respectively (series η). Using a thin (~ 4 nm) LT-AlN seeding layer, the GaN crystal directions show a significant dependency on the silicon surface orientation. The θ/2θ scans of GaN layers on Si(112) did not show any reflections in the 2θ range from 30° to 80° (Fig. 3.17 (a)). This means that no atomic planes of the GaN crystallites corresponding to 2θ angles from 30° to 80° are arranged parallel to the sample surface.

Bragg-Brentano measurement shows polycrystalline GaN structures grown on Si(117) (Fig. 3.17 (b)).

Since the angles between Si(112) and the Si(111) planes are about 19.5 °(Carine), if the GaN grows on the Si(111) planes of the Si(112) substrate, no GaN plane will be parallel to the surface. The $GaN(10\bar{1}6)$ plane is the nearest symmetric plane, whereas the angles between the $(10\bar{1}6)$ plane and the basal c-plane of GaN are about 17.4° [Carine). Thus, for the sample grown on Si(112) with a LT-AlN seeding layer thickness of ~ 4 nm, no symmetric reflection of GaN can be detected.

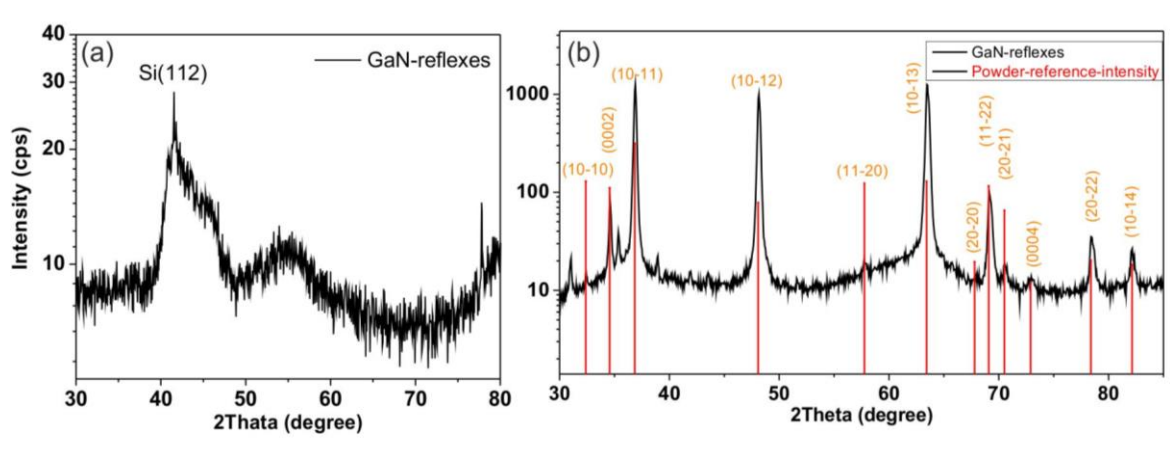**Fig. 3.17:** *Bragg-Brentano θ/2θ scans of GaN grown on Si(112) (a) and Si(117) (b).*
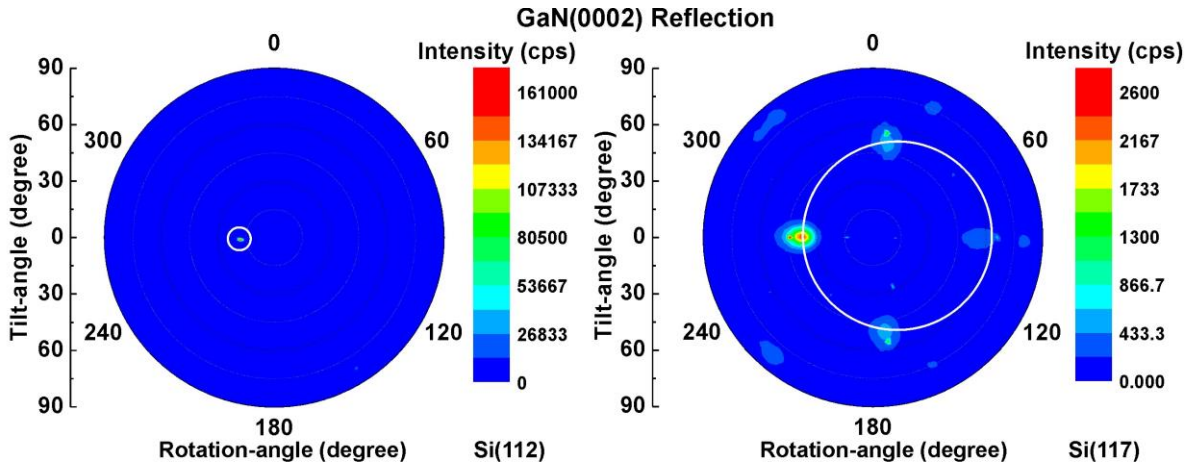
Fig. 3.18: *X-ray pole figure measurements of the GaN(0002) reflection of a layer grown with the same growth parameters on Si(112) (left) and on Si(117) (right). The existence of only one maximum in the image (left) shows that single crystalline GaN with a c-axis tilt-angle of ~ 18° with respect to the surface normal is grown on Si(112). When grown on Si(117) the four maxima of the GaN(0002) reflection in the right image show that there are four components of the GaN structure, whereby their c-axis has a tilt-angle of ~ 47° with respect to the surface normal and one of these is dominant. The white circle shows that the intensity maxima are not symmetrically positioned with respect to the center (0,0), which is the position of 0° tilt if the azimuthal rotation-angle is 0°.*

The pole figure measurements of (0002)GaN grown on Si(112) show only one GaN crystal orientation component with a tilt angle of about 18° [Ravash 2009], which is close to the angle between Si(112) and (111) (~ 19.4°). From a comparison of the expected Si(112) surface structure with the experimental results it can be concluded that the GaN film is most likely grown on the Si(111) facets usually formed on the Si(112) surface.

By measuring the GaN$(10\bar{1}1)$ reflection, six intensity maxima are observed (because of defocusing one of them has a lower intensity) which is expected for a hexagonal crystal structure. The angles between the GaN basal and $(10\bar{1}1)$ planes are ~ 62°, which are well pronounced in the pole figure. Because of the orientation of the GaN(0002) and two of the GaN$(10\bar{1}1)$ reflections in the same azimuth (Fig. 3.19, right), it is concluded that the azimuthal orientation of the c-axis inclination is towards the GaN$(1\bar{1}00)$ m-plane. Thus the GaN$(11\bar{2}0)$ a-planes are located perpendicularly to the substrate surface. From detailed x-ray measurements it is found that an angle of about 1.5° exists between the Si[111] and GaN[0001] directions. Additionally, the c-axis oriented GaN layer is not exactly grown

parallel to the Si(111) surface using a LT-AlN seeding layer on Si(111) and off-oriented Si(111) substrates (J. Bläsing). The reasons for this behavior are not clear.

The orientation distribution of the GaN crystallites grown on Si(117) shows four components having tilt-angles of ~ 47°, one of which is dominant with a higher intensity in comparison to the other maxima. This component has a higher intensity (~ four times) compared to one of the dominated GaN in-plane components grown by ~ 8 nm LT-AlN seeding layer with a low TMAl-flow rate (20 sccm) on Si(117) (Fig. 3.4). Si(001) has a four-fold symmetry. Since Si(001) / Si(111)-plane fraction on Si(117) substrate surface is higher than for Si(112), four in-plane components of GaN grown on Si(117) could be explained by the occurrence of a coincidence site lattice between nearly $GaN(10\bar{1}2)$ and Si(001) surface atoms and fourfold surface symmetry of Si(001) (as mentioned in section 3.1) [Reiher 2008].

The intensity of single crystalline GaN grown on Si(112) is significantly higher (~ 100 times) than that on Si(117).
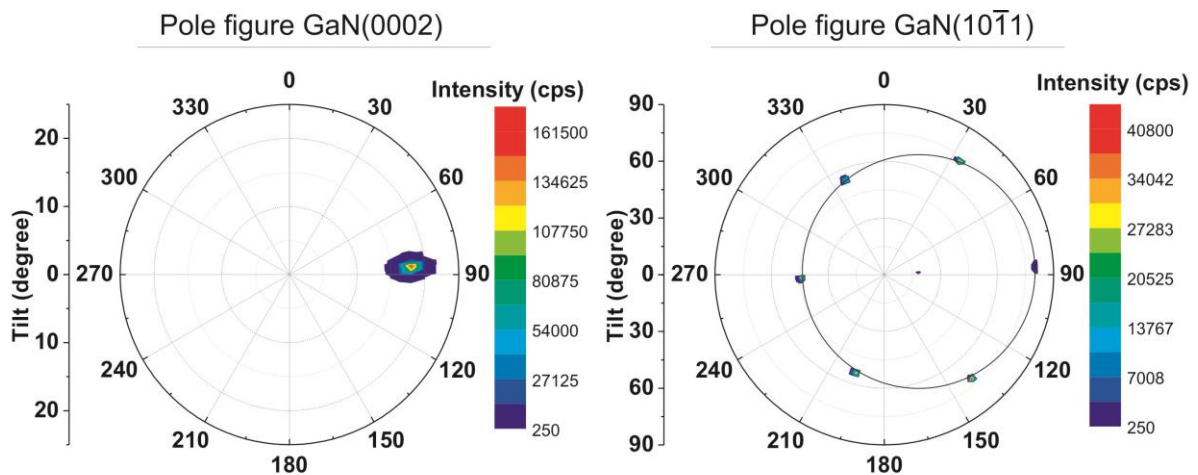
Fig. 3.19: *X-ray pole figure measurements of the GaN(0002) reflection (left) and $GaN(10\bar{1}1)$ reflection (right) grown on Si(112).*

The surface morphologies of these samples (series η) were measured by FE-SEM and are shown in Fig. 3.20. They demonstrate that the single crystalline GaN orientation on Si(112) enables the growth of a continuous GaN layer when a sufficiently thick GaN layer is grown. Fig. 3.20 (a) shows an early stage of coalescence of the GaN inlands on Si(112), which leads to a smooth surface after growing thicker GaN layers shown on Fig. 3.20 (c). In comparison Fig. 3.20 (b) shows a polycrystalline GaN growth resulting in non-coalesced GaN structures on Si(117) (Fig. 3.20 (d)).

Fig. 3.20: *FE-SEM-images of GaN structures grown with the same growth parameters on Si(112) (left) and Si(117) (right), (a) and (b) show nominally ~ 150 nm thick (4 min) GaN structures. (c) and (d) show nominally ~ 600 nm thick (15 min) GaN with a thickness of ~ 1.2 μm for the total structures. The sample structures are sown in Fig. 3.2 using a (~ 4 nm) LT-AlN seeding layer at high TMAl-flow rate (80 sccm).*

Conclusion

The orientation distribution of semi-polar grown GaN crystallites was investigated on high index silicon substrates (Si(112), Si(115), 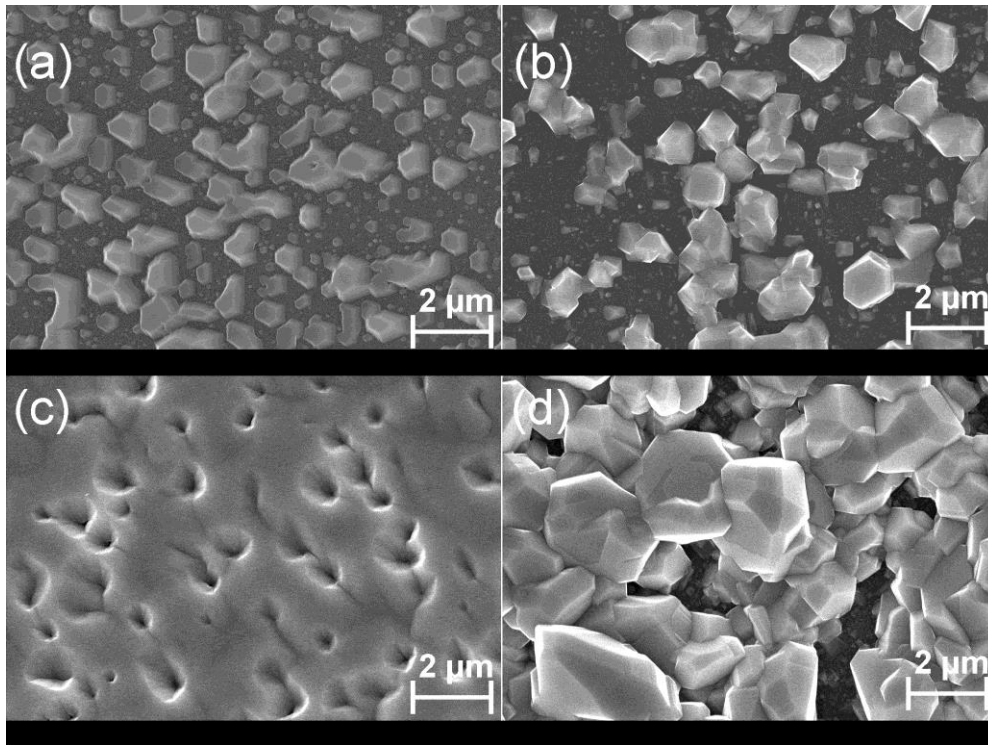Si(117), Si(410), and Si(100)+ 4.5° off-oriented). It is found that the GaN crystallite orientation depends on the LT-AlN seeding layer growth parameters such as temperature and thickness. It has been observed that using a HT-AlN seeding layer, c-axis GaN is grown independently of the substrate orientation [Reiher 2010]. A LT-AlN seeding layer can lead to a semi-polar growth of GaN. The crystallite orientation of GaN with a thick LT-AlN seeding layer is nearly independent of the silicon surface direction. Applying a thin (~ 4-8 nm) LT-AlN seeding layer shows a clear difference in GaN growth directions regarding the silicon surface orientations. In the case of a thin LT-AlN seeding layer, the symmetry of the substrate surface could be transferred onto the GaN layers. A single crystalline GaN with a continuous layer on Si(112) can be grown by applying a thin LT-AlN seeding layer (~ 4 nm, 15 s) grown with high TMAl-flow rate

(80 sccm), whereas with the same growth parameters on Si(117) four GaN components are achieved. It has been also observed that the values of c-axis tilt angles of GaN layers depends on LT-AlN seeding layer thickness.

3.3 Single crystalline semi-polar GaN layer on Si(11h)

In the following sections, the results of GaN textures as a function of the LT-AlN seeding layer thickness grown on Si(112) are presented. After this, semi-polar growth of GaN crystallites on different silicon surfaces such as Si(112), Si(113), Si(114), Si(115), Si(116), and Si(117) applying optimized seeding layer growth parameters for Si(112) are discussed. Single component gallium nitride crystallites were obtained on all Si(11h) substrates mentioned above except on Si(117).

3.3.1 Impact of LT-AlN seeding layer thickness on GaN grown on Si(112)

For this investigation, samples labelled A to E are grown on Si(112). Here the effect of the LT-AlN seeding layer thickness (growth time) variation on the GaN crystallite orientation is studied. See Fig. 3.2 and Table 3.1 for sample structure and growth parameters respectively. The LT-AlN seeding layer was grown for 15 seconds to 16 minutes corresponding to a nominal thickness of ~ 4 to 250 nm at a fixed TMAl-mass flow rate of 35 μmol/min (TMAl-flow rate = 80 sccm, at TMAl bubbler pressure of 1000 mbar).

Table 3.1: Growth parameters of the samples A to G.

Sample	AlN	AlN	AlN	GaN
	TMAl-mass-flow-rate (μmol/min)	Temperature (°C)	Nominal thickness (Growth time)	Nominal thickness
A(MD5459)	35	680	~250 nm (16 min)	~600 nm
B(MD5453)	35	680	~32 nm (2 min)	~600 nm
C(MD5450)	35	680	~16 nm (1 min)	~600 nm
D(MD5458)	35	680	~8 nm (30 s)	~600 nm
E(MD5460)	35	680	~4 nm (15 s)	~600 nm
G(MD5637)	35	680	~4 nm (15 s)	~1.6 μm

The Bragg-Brentano θ/2θ measurements of these samples are shown in Fig. 3.21. It is observed that the thick LT-AlN seeding layer (sample A, ~ 250 nm) leads to polycrystalline GaN structures detecting different GaN reflections such as $(10\bar{1}0)$, (0002), $(10\bar{1}1)$,

$\left(10\bar{1}2\right)$. It was observed that the intensity of GaN reflections reduces when the LT-AlN seeding layer thickness decreases. For sample E grown with a thickness of ~ 4 nm LT-AlN seeding layer, no symmetric reflection of GaN is detected in the 2θ range from 30° to 80°. The pole figure of this sample is shown in Fig. 3.18.
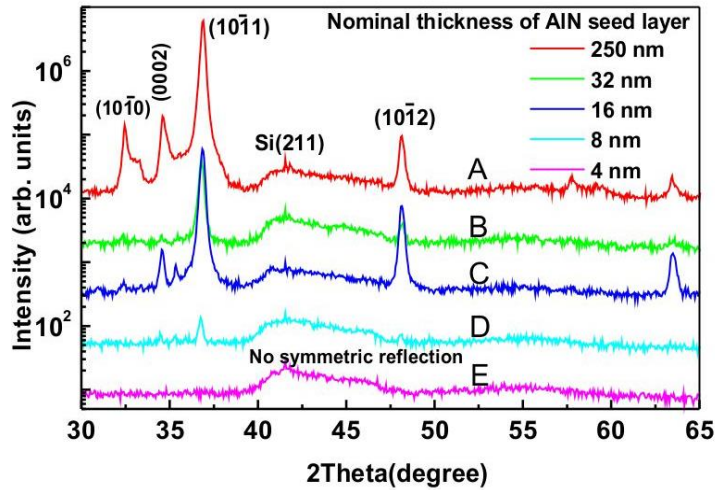
Fig. 3.21: *Bragg-Brentano measurements of GaN layers as a function of LT-AlN seeding layer thickness (growth time).*

The FE-SEM measurements of the GaN surface morphology are shown in Fig. 3.22. Sample A with a thicker LT-AlN seeding layer shows a rough surface (left). Sample E shows a continuous GaN (~ 600 nm) resulting in smooth surface GaN layers with a number of pits (middle). Sample G with about 1.6 µm thick GaN layers (45 min) shows a decreasing density of pits (right). Sample G was grown with the same growth parameters of sample E for LT-AlN seeding layer and GaN layer, except the GaN-thickness.

Fig. 3.22: *FE-SEM measurements of the GaN surface morphology. The sample G with about 1.6 µm thick GaN layers shows a decreasing density of pits (right).*

3.3.2 Single component GaN grown on Si(11h)

Three groups of samples, with the samples of each group grown under the same growth conditions are investigated. Group I includes Si(112) and Si(117), group II contains Si(113), Si(114) and Si(116) and group III consists of Si(112), Si(113) and Si(115). Group I and II: A LT-AlN seeding layer with an Al predeposition is directly deposited onto the Si-substrates at 720 °C. The growth parameters 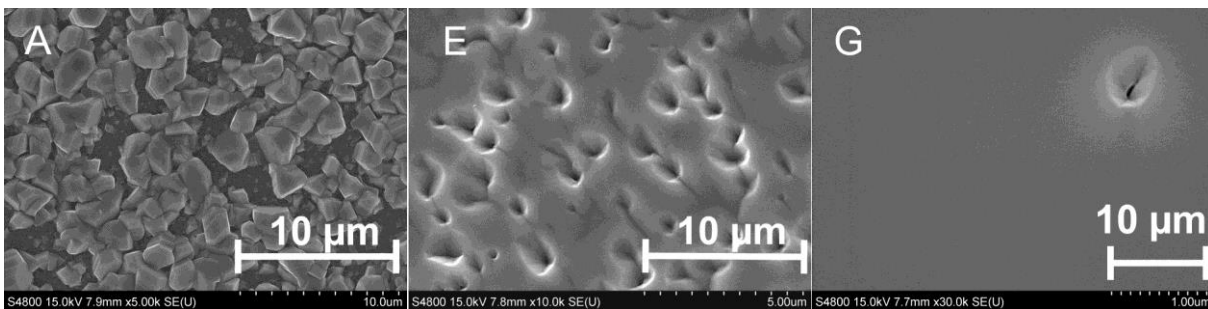are optimized for Si(112) substrate and applied for all other Si orientations (growth parameters are listed in Appendix, Table 3). Because a thin (~ 4 nm) LT-AlN seeding layer is not able to sufficiently prevent melt-back etching, a threefold HT-GaN / LT-AlN (~ 160 nm/~ 8 nm) interlayer sequence follows the seeding layers. On top of the layers, a nominally 600 nm thick GaN layer is grown for 15 min at 1145 °C. The samples of group III are differently grown in order to study the layer quality for thicker GaN. Nearly the same LT-AlN seeding layer, as above mentioned for group I and II, are followed by an $Al_xGa_{1-x}N$ layer with an Al content of about 50%. Subsequently, the GaN main layer is grown ~ 2 μm thick at 1145 °C. For stress compensation, a LT-AlN interlayer (~ 8 nm) is inserted in the GaN layer after a thickness of ~ 800 nm.

3.3.2.1 X-ray measurements

The results of pole figure measurements are shown in Fig. 3.23. It is found that single component GaN is grown on planar Si(11h) from (112) to (116), whereas four components of GaN with a larger tilt angle appear on Si(117). As the index h increases an increasing c-axis tilt-angle of the semi-polar GaN crystallites is observed. The results demonstrate a correlation between the c-axis tilt-angle θ of GaN (experimental values) and the angles α (theoretical values = angle between Si(11h) and Si(111) planes) (Table 3.3). It is also found that the c-axis of the GaN layers are not oriented parallel to the Si[111] direction and that there are deviations between these two directions, whereby their values increase from Si(112) to Si(117) (Fig. 3.24). For GaN grown on Si(112) to Si(116) the tilt angles are smaller than angles α, whereby they are larger for the case when Si(117) is used as a substrate. Fig. 3.25 shows that the deviation values of theoretical α and experimental θ angles are dependent on the Si(111) plane fraction on the Si(11h) substrate surface.

With increasing tilt angle the intensity maxima from Si(112) to Si(117) are broadened visibly by the width of the texture reflections. Due to the increasing mosaicity the coalescence

of the GaN crystallites to form continuous layers is increasingly difficult for higher h values. The intensity of the GaN maxima decreases from 161 kcps for Si(112) to 400 cps for Si(117). Since GaN grown on Si(115) is thicker than that grown on other Si orientations, a higher intensity of GaN is observed, but the c-axis tilt-angles are nearly independent of the thickness of GaN.

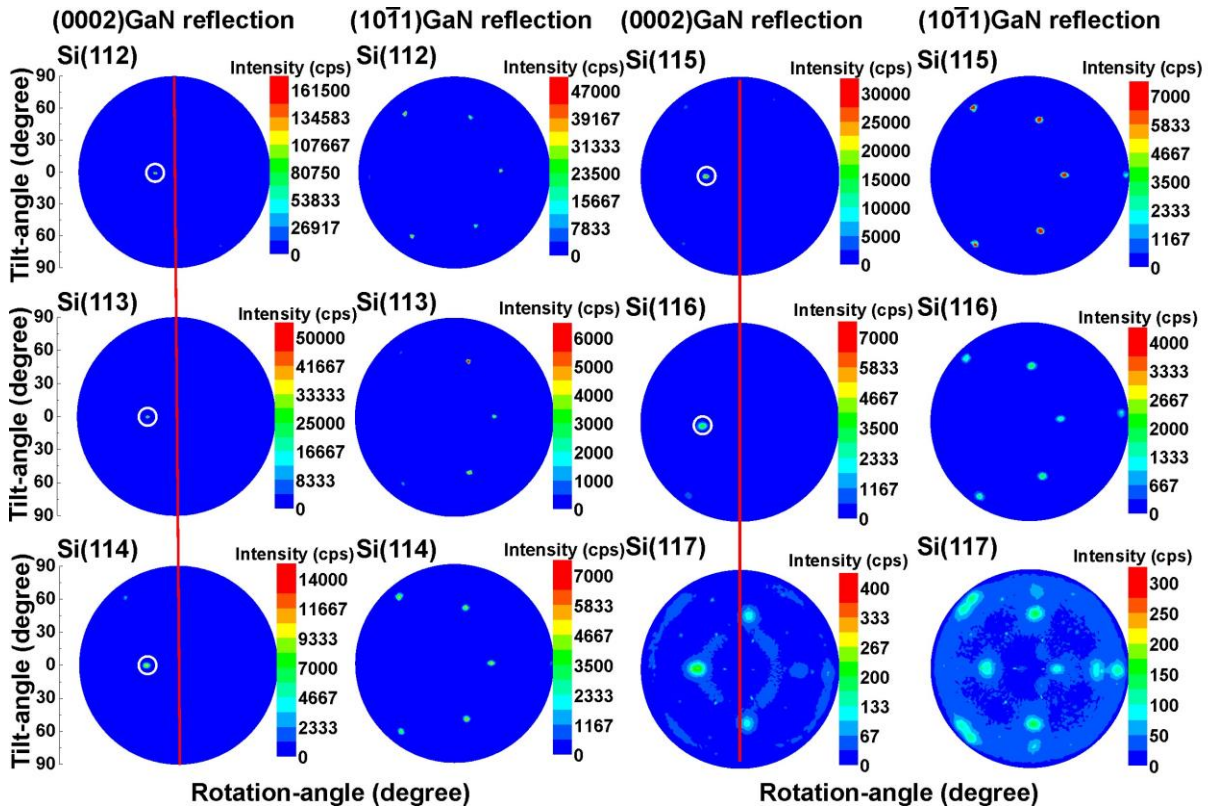**Fig. 3.23:** *Pole figure measurements of GaN structures grown on different Si surfaces from Si(112) to Si(117). Measurements at the GaN(0002) and GaN$(10\bar{1}1)$ reflections are performed for each sample showing crystallite orientation and azimuthal rotation of the GaN crystallites, respectively. The (φ,ψ) = (0,0) is marked by a red vertical line, which shows the position for c-axis oriented GaN.*
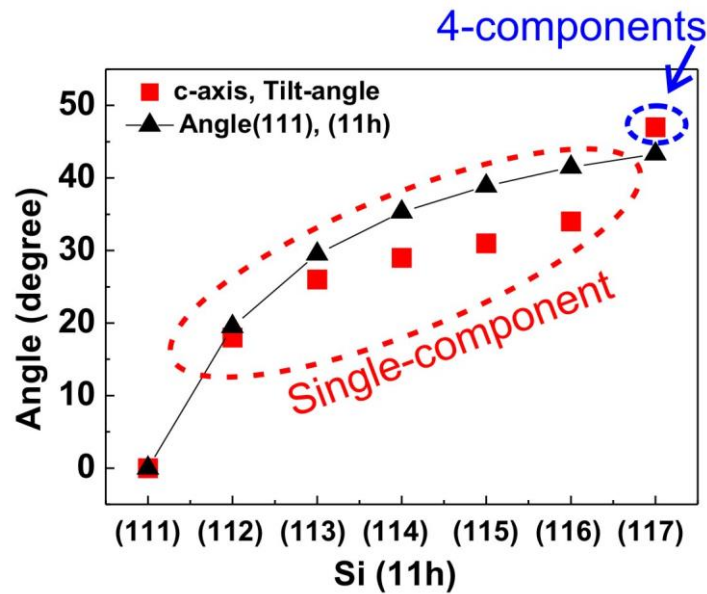
Fig. 3.24: *Correlation between angle θ (experimental c-axis tilt angle) and the angle α (between Si(111) and Si(11h) planes) (see Table 2.2).*

Imperfection in crystals can be defined as mosaicity, which is the width of the distribution of mis-orientation angles of all the unit cells in a crystal. In order to determine the mosaicity of thin film GaN as a function of GaN thickness, two groups of samples with different nominal thickness of 600 nm and 2 μm for GaN were investigated by ω-scans. Here, for investigated samples, the full width at half maximum (FWHM) is dominated by the orientation disorder, i.e. twist and tilt of the crystallites with respect to each other. The results for all samples of each group (II and III) grown on different Si substrate orientations are shown in Fig. 3.26. Since there is no lattice plane of GaN parallel to the substrate surface, a symmetric ω-scan measurement is impossible. Here the x-ray ω-scans of the nearly symmetric GaN reflection are measured. These are the $\text{GaN}(10\bar{1}6)$ and $\text{GaN}(10\bar{1}4)$ reflections for Si(112) and Si(113) and the $\text{GaN}(10\bar{1}3)$ reflection for Si(114), Si(115) and Si(116), respectively, which best correspond to the c-axis tilt angles in each sample (Table 2.2). It is observed that the tilt and twist of GaN crystallites increases significantly from Si(112) to Si(117). Therefore Si(11h) substrates with smaller h values are mostly used for further investigation.

70

Table 3.3: *Theoretical and experimental results of c-axis tilt angle of the GaN structures grown on Si(11h).*

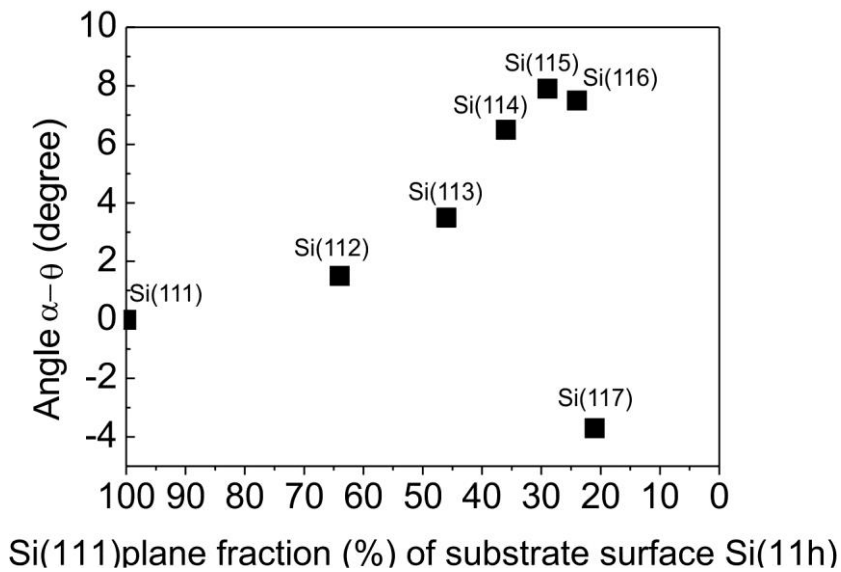| Si(11h)	Theoretical Angle α between Si(111) and Si(11h)	Experimental c-axis tilt angle θ	Si(111)plane fraction of substrate surface
(111)	0°	0° (one-component)	100%
(112)	19.5°	18°(one-component)	64%
(113)	29.5°	26°(one-component)	46%
(114)	35.3°	29°(one-component)	36%
(115)	38.9°	31°(one-component)	29%
(116)	41.5°	34°(one-component)	24%
(117)	43.3°	47°(four-components)	21%
(001)	54.7°	43°(four-components)	0%

Fig. 3.25: *Deviation of the angles α (angle between Si(111) and Si(11h) planes) and θ (theoretical c-axis tilt angle) as a function of the Si(111) plane fraction of Si(11h) substrate surface. The Si(111) plane fraction of Si(11h) surface decreases from Si(112) to Si(117). Si(117) has a larger c-axis tilt angle compared to its theoretical value.*
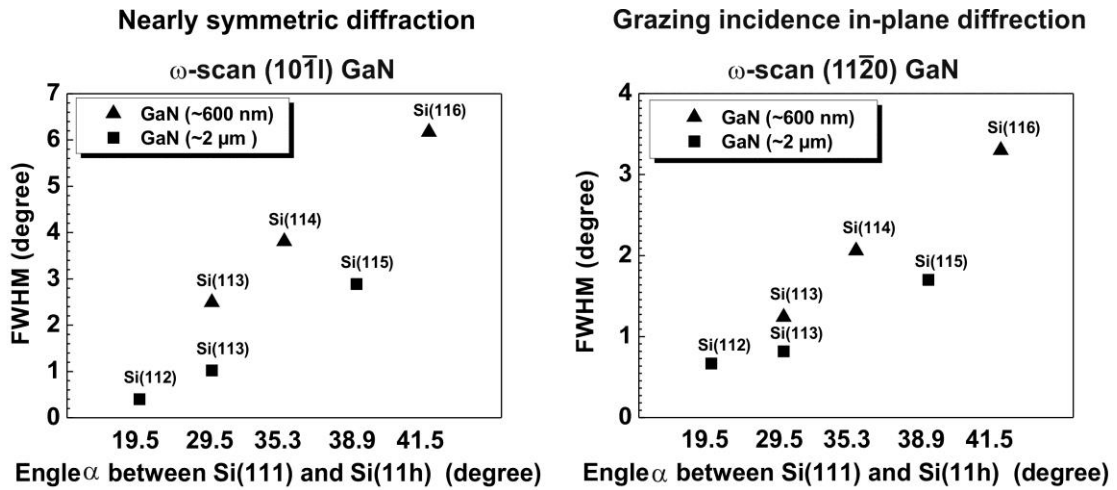
Fig. 3.26: *FWHM of ω–scan of nearly symmetric GaN $\left(10\bar{1}l\right)$ reflections (left) and FWHM of ω-scan of grazing incidence in-plane GaN $\left(11\bar{2}0\right)$ reflection (right).*

3.3.2.2 Surface morphology of GaN

The surface morphologies of the samples (described in section 3.3.2) are shown in Fig. 3.27. They are measured by FE-SEM. GaN surface structures on Si(112), Si(113), Si(114), Si(116), and Si(117) show that the tendency of the smooth GaN layer formation is reduced from Si(112) to Si(117). Since the Si(111) planes on Si(117) surface are smaller than those on Si(112), it is difficult to obtain a two dimensional growth mode resulting in a smooth GaN layer on Si(117). Fig. 3.27 (a, c) shows the surface of GaN on Si(112) and Si(117) respectively, whereas ~ 160 nm GaN are grown on three-fold HT-GaN / LT-AlN layers. Here, an early stage of coalescence of the GaN inlands on Si(112) is shown. In comparison, the GaN inlands grown on Si(117) cannot coalesce together. Fig. 3.27 (b, d) shows a surface morphology of 600 nm GaN on Si(112) and Si(117), respectively. A smooth surface can be obtained for a GaN layer grown on Si(112) in comparison to GaN structures grown on Si(117) having a rough surface. Figs. e-g show the surfaces of GaN structures on Si(113), Si(114), and Si(116), respectively, whereas Fig. 3.27 (h-j) are enlarged images of Fig. 3.27 (e-g).
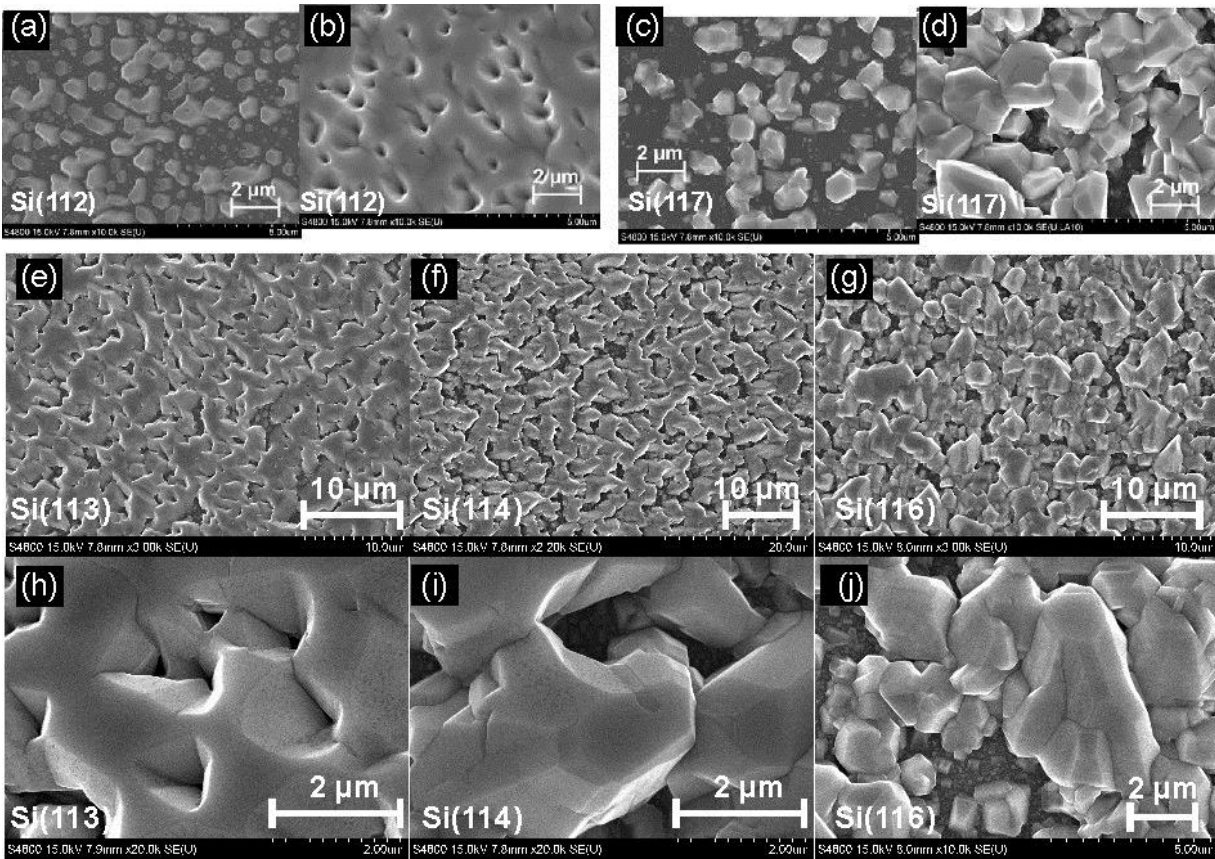
Fig. 3.27: *FE-SEM images of GaN structures (a-d) grown on different Si(112) to Si(117) substrates (group I). (e-g) images show surface of GaN structures (group II) on Si(113), Si(114) and Si(116), respectively, whereas (h-j) are enlarged images of (e-g).*

3.3.3 GaN growth on Si(11h), h = 2, 3

As shown in section 3.3.2, the semi-polar GaN layers were grown on a thin (~ 4 nm) LT-AlN seeding layer at high Al-flux = 80 sccm on Si(112) and Si(113). A thin (~ 4 nm) LT-AlN seeding layer cannot fully prevent melt-back etching when thick GaN layers are deposited. Therefore the following samples (series ι) were grown with a thicker LT-AlN seeding layer at TMAl-flow rate = 20 sccm. Here the results of GaN layers with different LT-AlN seeding layer thicknesses from ~ 4 nm to ~ 40 nm (growth time variation from 1 min to 10 min) are presented. The samples structures were grown with the nominal growth parameters (Appendix, Table 4) as presented in Fig. 3.2 (Al-predeposition/ LT-AlN seeding layer/ 3x [HT-GaN (~ 160 nm)/ LT-AlN (~ 8 nm)] / GaN (600 nm)).

3.3.3.1 Surface morphology

Nomarski images of GaN structures grown on Si(112) are shown in Fig. 3.28. A smooth surface with a pit density of $\sim 10^7$ /cm^2 (10 per 100 µm^2) is obtained when applying a $\sim$ 8 nm (2 min) LT-AlN seeding layer. The size and density of the pits increase when the LT-AlN seeding layer thickness increases but also in the case of a reduced LT-AlN seeding layer thickness (1 min growth time).

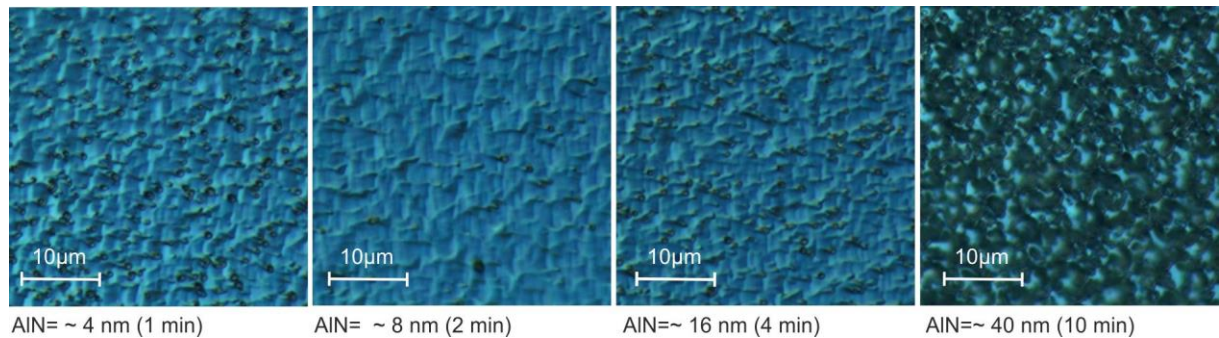AlN= $\sim$ 4 nm (1 min)   AlN= $\sim$ 8 nm (2 min)   AlN=$\sim$ 16 nm (4 min)   AlN=$\sim$ 40 nm (10 min)

Fig. 3.28: *Nomarski images of the surface morphology of GaN layers ($\sim$ 600 nm, 15 min) on Si(112) with different (from 4 nm to 40 nm) LT-AlN seeding layer thicknesses.*

3.3.3.2 X-ray measurements

Fig. 3.29 shows the GaN c-axis tilt angle as a function of the LT-AlN seeding layer thickness. One can see that the GaN c-axis tilt angle becomes smaller as the LT-AlN seeding layer thickness increases, resulting in an increased deviation between the experimental data and the theoretical values for c-axis tilt angle. This probably originates in the higher coverage of thick LT-AlN, preventing the dominance of AlN grown on Si(111) facets and a higher influence from AlN nucleated with a lower inclination angle on the Si(001) type terraces. Unfortunately, the detailed surface structure during AlN nucleation is unknown. Since different Si surface structures are not based on the simple surface model, assuming Si(111) and Si(001) terraces, man can see a deviation between the experimental data and the theoretical values for c-axis tilt angle. On the other hand, the GaN c-axis tilt angle becomes smaller as the LT-AlN seeding layer thickness decreases ($\sim$ less than 8 nm, 2 min). The exact reason of this effect is unknown. It could be explained due to melt-back etching effect in the case of thin ($\sim$ less than 8 nm, 2 min) LT-AlN seeding layers. The optimum tilt angle could be obtained for a thick LT-AlN seeding layer thickness between 8 nm and 16 nm (2 to 4 min growth time).

Fig. 3.30 (left) presents the FWHM of ω–scans of nearly symmetric GaN$(10\bar{1}6)$ and GaN$(10\bar{1}4)$ reflections grown on Si(112) and Si(113) substrates, respectively. Fig. 3.30 (right) shows the FWHM of ω-scans of grazing incidence in-plane GaN$(11\bar{2}0)$ reflection, which were grown on Si(112) and Si(113). The best GaN quality (in series ι) could be achieved for a LT-AlN seeding layer with a thickness between 8 nm and 16 nm (2 to 4 min growth time).
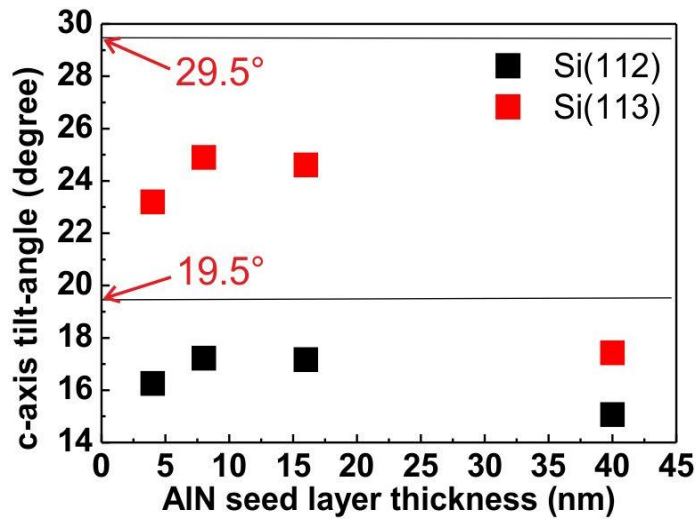
Fig. 3.29: *C-axis tilt angle of GaN structures as a function of LT-AlN seeding layer thickness on Si(112) and Si(113). 19.5° and 29.5° are the expected theoretical values of GaN inclination anglse with respect to the substrate surface normal vector grown on Si(112) and Si(113).*
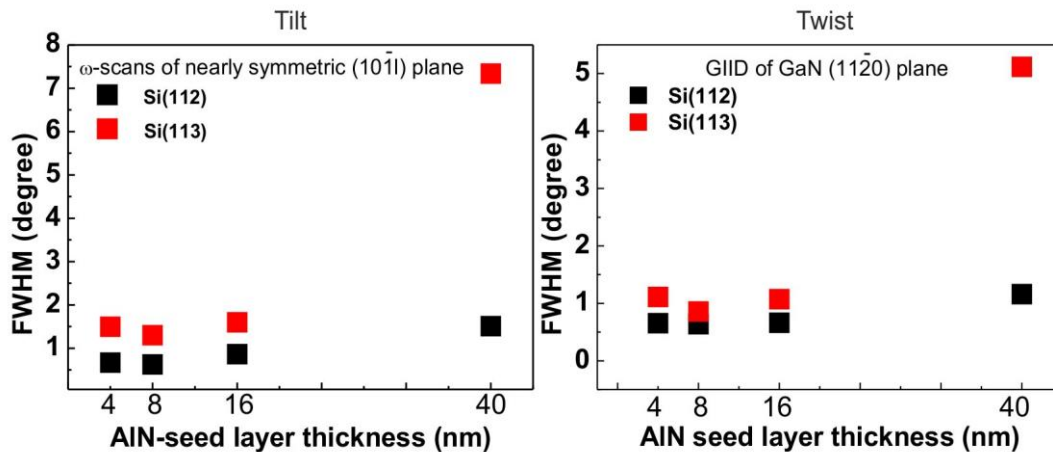

Fig. 3.30: *FWHM of XRD ω–scan of nearly symmetric GaN $(10\bar{1}l)$ reflections (left) and FWHM of ω-scan of grazing incidence in-plane $(11\bar{2}0)$ reflection (right).*

Conclusion

The results of a study on the semi-polar GaN layer grown on the different non-patterned high index Si substrates such as Si(11h) and Si(410) regarding to the LT-AlN seeding layer thickness (growth time) are briefly summarized in this section. Fig. 3.31 shows the GaN inclination angle with respect to the substrate surface normal vector as a function of the LT-AlN seeding layer thickness. The results can be divided into 3 groups:

The first group grown on Si(115), Si(117) and Si(410): here it is observed that the GaN c-axis tilt angles and the number of GaN components increase as the LT-AlN seeding layer thickness increases.

The second group grown on Si(112) and Si(113): GaN layers were grown as single-component GaN on Si(112) and Si(113) applying ~ 4 nm (1 min) to ~ 40 nm (10 min) thick LT-AlN seeding layers. The GaN c-axis tilt angles decrease as the LT-AlN seeding layer thickness increases from ~ 8 nm to ~ 40 nm (from 2 min to 10 min).

As already mentioned, GaN growth on Si(11h) with the LT-AlN seeding layers is essentially c-axis oriented growth on the naturally occurring Si(111) planes on the high index Si(11h) substrate surfaces. It is known that Si(113) consists of a nearly equal fraction of the Si(111) and Si(001) and the fraction of the Si(111) plane decreases for higher h values > 3 and increases for Si(11h) with h < 3 [Dabrowski 2000]. Because of this GaN grown on Si(114) (third group) shows an interesting boundary behaviour where the GaN structural properties are changed. Single component GaN layers are grown on Si(114) for LT-AlN seeding layer thicknesses of ~ 8 nm. Here Si(114) behaves like Si(11h) with h ≤ 3. A layer with six GaN-components showing a larger c-axis tilt angle was grown on Si(114) in the case of ~ 40 nm thick (10 min) LT-AlN seeding layer. Additionally, it was observed that a thin (~ 4 nm) AlN seeding layer at high Al-flux (80 sccm) leads to a larger GaN inclination angle grown on Si(112) and Si(117). Pole figure measurements of these samples show a higher intensity compared to that with a low Al-flux (20 sccm). A single component GaN layer was grown on Si(112) to Si(116) compared to four components GaN layer on Si(410) and Si(117).
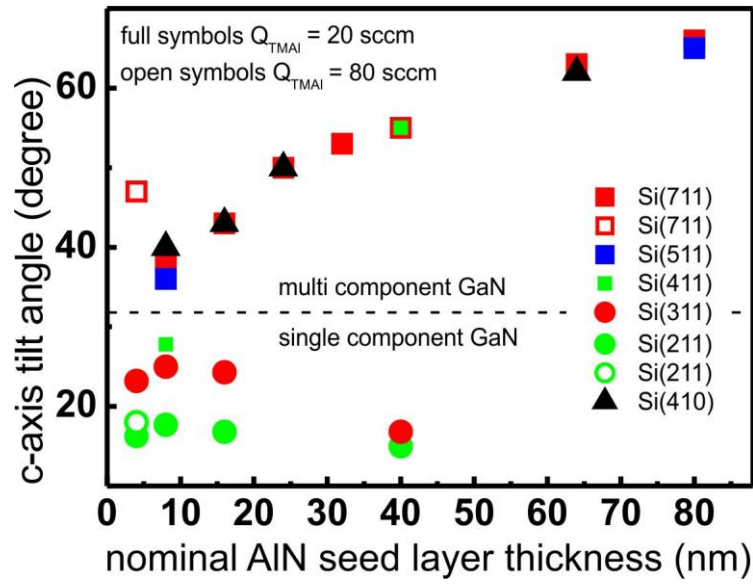
Fig. 3.31: *GaN c-axis tilt angle in a function of LT-AlN seeding layer thickness and growth rate on different Si substrate orientation.*

4 Elimination of stacking faults

The reduction of polarization fields in III–V nitride structures requires the growth of non-polar or semi-polar layers. Stacking faults (SFs) are one of the main types of extended defects in such layers [Wieneke 2009, Liu 2005]. Usually they are terminated at each end by partial dislocations [Stampfl 1998]. TEM investigations have reported a higher density of SFs near the layer-substrate interface [Wu 1996, Romano 1997]. In this chapter, the elimination of stacking faults by the insertion of a LT-AlN interlayer in semi-polar GaN layers grown on Si(112) and Si(113) is presented and discussed. The optical and structural properties of the samples were investigated by CL, PL, FE-SEM, TEM, STEM, and STEM-CL measurements.

4.1 Structural and optical properties of GaN grown on Si(112)

As demonstrated in chapter 3, a ~ 4 nm thin LT-AlN seeding layer grown with a high Al-flux (80 sccm) has a significant effect on GaN layers and single crystalline semi-polar were achieved on Si(112) as well as on Si(11h) with h=3,4,5 and 6. For samples E and G (grown on Si(112)), the final GaN layer was deposited with a nominal thickness of ~ 0.6 μm and ~ 1.6 μm leading to a total structure thickness of ~ 1.2 μm and ~ 2 μm respectively (layer structures are shown in Fig. 3.2).

To determine the tilt distribution of the GaN crystallites, x-ray ω-scans of nearly symmetric $GaN(10\bar{1}6)$ reflection with a ω-FWHM of ~ 0.9° and ~ 0.3° were measured for samples with total thicknesses of ~ 1.2 μm and ~ 2 μm respectively. Additionally, for analyzing the in-plane orientation of the GaN structures ω-scans of the $(11\bar{2}0)$ reflection were measured by GIIXD, resulting in a ω-FWHM of about 0.9° and 0.57° for GaN with total thickness of ~ 1.2 μm and ~ 2 μm respectively.

Optical properties were examined by CL spectroscopy at low temperature (5 K). The measured spectra in the spectral range from 343 nm to 390 nm are shown in Fig. 4.1. Here the (D^0,X) emission at 357 nm dominates the spectrum. An I_1-type basal plane stacking fault (I_1-BSF) with related luminescence of around 364 nm is visible with an intensity of approximately an order of magnitude lower. The emission peak at ~ 376 nm could be due to a donor-acceptor pair (DAP) band recombination, a prismatic stacking fault (PSF), I_2-BSF and partial dislocation (PD) or a combination of these effects.
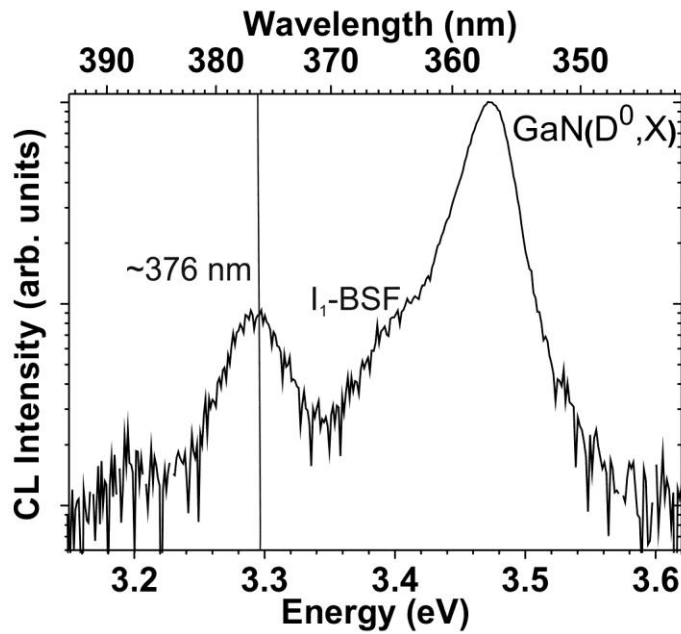
Fig. 4.1: *Integrated plan-view CL of GaN grown on Si(112) with threefold HT-GaN/ LT-AlN interlayer. The spectrum is dominated by (D^0,X) luminescence at 357 nm, I_1-BSF related luminescence at ~ 364 nm and a emission peak at ~ 376 nm (sample E).*

To study the growth in the early stage of GaN epitaxy, a cross sectional TEM measurement of the sample with a total thickness of ~ 1.2 μm was performed. As shown in Fig. 4.2 (a), GaN layers grown after the seeding layer are not smooth and LT-AlN interlayers follow these surface undulations. In the GaN/AlN/Si interface region, locally varying stress leads to a bending of the thin specimen foil and to grey contrasts (known as bend contours) while they originate from thickness interferences because the foil is very thin. In the coalescence region (marked with a blue dashed circle) of GaN crystals a higher number of defects is found. Even though the CL measurement (Fig. 4.1) shows a low intensity of I_1-BSF luminescence compared to that of non-polar GaN layers [Wieneke 2009], STEM image (Fig. 4.2 (b)) shows BSF penetration through the LT-AlN interlayer in a position, where they are not growing parallel to the substrate surface.
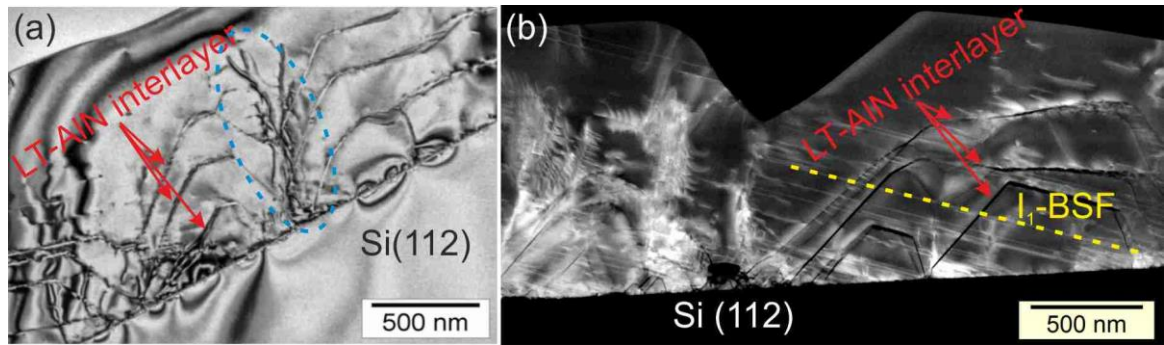
Fig. 4.2: *TEM image (a) and STEM image (b) of a ~ 1.2 μm GaN layer grown on Si(112). Here the threefold HT-GaN/LT-AlN layer stack marks different stages of growth.*

4.2 Thick GaN grown on Si(112) and Si(113)

To further investigate the impact of the Si substrate orientation on the subsequent GaN-layer, samples were grown simultaneously on Si(112) and Si(113) substrates using the LT-AlN seeding layer growth parameters optimized on Si(112) substrates. These samples start with an AlGaN interlayer after the ~ 4 nm thick LT-AlN seeding layer (Fig. 4.3). Nearly $(10\bar{1}6)$ and $(10\bar{1}4)$ oriented GaN films on planar Si(112) and Si(113) were obtained leading to a c-axis inclination angle of ~ 18° and ~ 26° with respect to the surface normal vector.
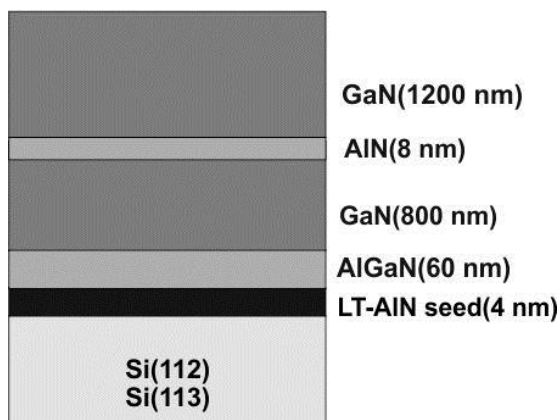
Fig. 4.3: *Layer structure of sample MD5818 (Appendix, Table 3).*

4.2.1 Sample morphology

FE-SEM images of GaN layers on Si(112) and Si(113) are shown in Fig. 4.4, whereas (a) and (b) are cross sectional and (c) and (d) top-view images. The LT-AlN interlayers are

marked with dashed lines. As shown in Fig. 4.4 (a), the LT-AlN interlayer follows the surface morphology of the first GaN layer, being nearly parallel to the substrate surface on Si(112). The second GaN layer (~ 1.2 μm), which is grown on top of the LT-AlN interlayer on Si(112), is smoother with few pits and some cracks (Fig. 4.4 (c)).

In contrast, a cross sectional FE-SEM image (Fig. 4.4 (b)) of GaN grown on Si(113) shows that the first GaN layer was deposited as separated islands and not coalesced before the LT-AlN interlayer. Thus, the second GaN layer is not sufficiently thick to smooth out and terminates in a rough pyramidal GaN surface. This shows the higher contribution from 3D grown GaN on Si(113) and the significant impact of the substrate orientation on the morphology of the GaN layers.
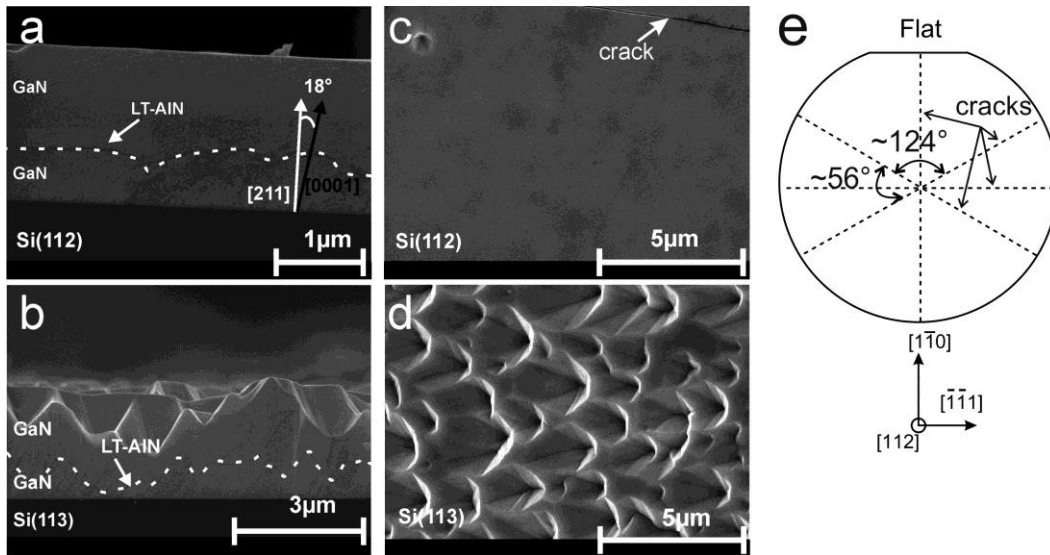
Fig. 4.4: *FE-SEM images of GaN layers in cross sectional (a, b) and top-view (c, d). Samples were grown on Si(112) (a, c) and on Si(113) (b, d). The LT-AlN interlayer is highlighted by dashed lines in cross sectional images (a, b). Both samples were grown in the same growth experiment under conditions optimized for GaN on Si(112). (e) shows the crack directions (dashed lines) of GaN structures grown on Si(112).*

4.2.2 Optical properties

The optical properties were examined by PL- and CL-spectroscopy at low temperature. PL integral spectra in the spectral range from 344 nm to 413 nm are shown in Fig. 4.5. The red curve shows the emission of GaN grown on Si(112): the (D^0,X) emission at ~ 360 nm dominates the spectrum and shows GaN under tensile stress. With an about two orders of magnitude lower intensity, I_1-BSF related luminescence around 368 nm is visible.

At ~ 381 nm an emission peak was measured which can relate to DAP/PSF/I_2-BSF/PD luminescence.

This sample has a good optical quality as evidenced by the presence of an intense near band edge emission. The blue curve shows the emission of GaN grown on Si(113): two contributions of (D^0,X) and I_1-BSF luminescence are observed with a nearly the same intensity.
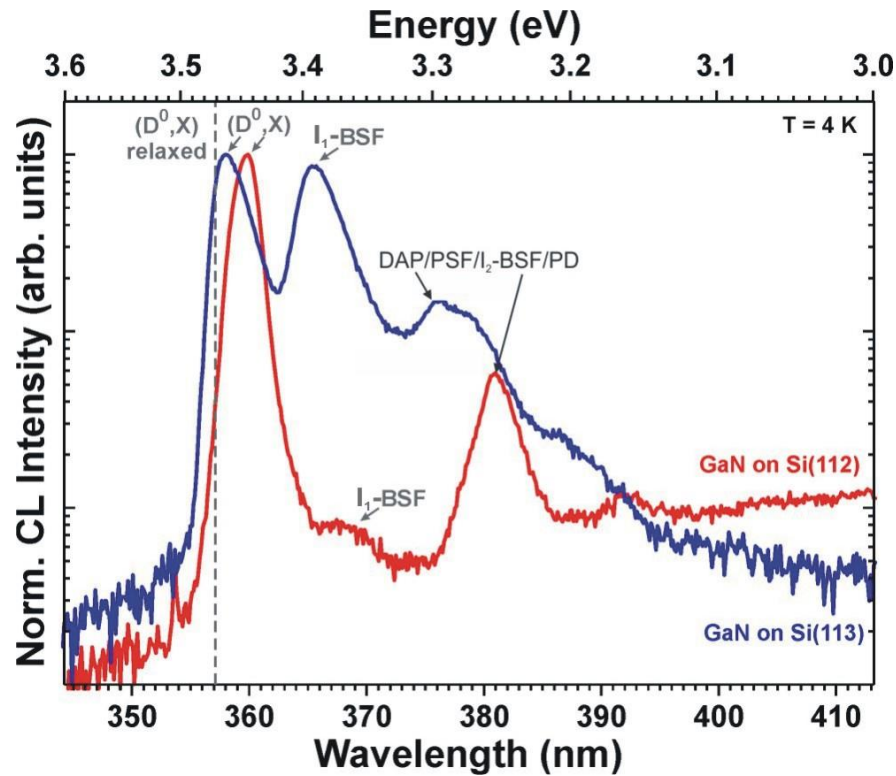
Fig. 4.5: *Top-view PL-measurements of GaN on Si(112) (red) and Si(113) (blue): here integrated PL spectra at low temperature (4 K) show strongly reduced I_1-BSF in GaN on Si(112).*

Cross sectional CL and local spectra recorded at different positions, i.e. the local spectra of the first and the second GaN layers grown on Si(112) and Si(113) are shown in Figs. 4.6 and 4.7, respectively [Morkoc 2005]. The CL wavelength image (Fig. 4.6 (c)) of the sample grown on Si(112) was recorded in the wavelength range from 355 nm to 380 nm. It shows that the first GaN layer exhibits a spotty wavelength distribution dominated by I_1-BSF, I_2-BSF, PSF, PD, and DAP luminescence. In comparison to the second GaN layer, the upper GaN layer depicts (D^0,X) luminescence and very weak defect related luminescence. The results of the local spectra (Fig. 4.6 (a)) are as follows: in a region near the substrate, dominant I_1-BSF emission and weak (D^0,X) emission of a compressively stressed GaN layer can be observed. In the region below the LT-AlN interlayer, dominant DAP/PSF/I_2-BSF/PD

luminescence with a weak (D^0,X) emission are visible. In the upper GaN layer, a dominant (D^0,X) emission from tensely stressed material is found.

In Fig. 4.7 (c), the CL wavelength image does not show clearly identifiable single layers. Here a spot like wavelength distribution within the whole structures is observed. GaN grown on Si(113) under the same growth conditions does not show I_1-BSFs reduction in the GaN layer and needs further optimized growth conditions.
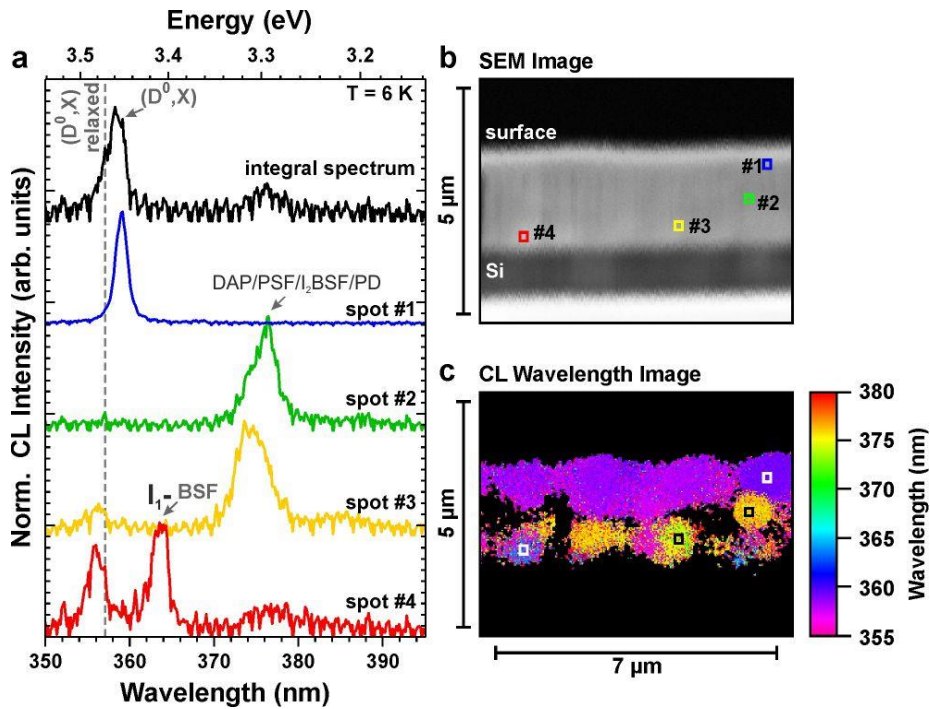
Fig. 4.6: *Local spectra (a) at the cross section shown in the SEM image (b) and the corresponding CL wavelength image (c) in which single layers of the sample grown on Si(112) are visible. The lower GaN layer exhibits a spotty wavelength distribution mostly originating in I_1-BSF and DAP/PSF/I_2-BSF/PD related luminescence. In contrast to that, the upper GaN layer shows dominant (D^0,X) luminescence.*
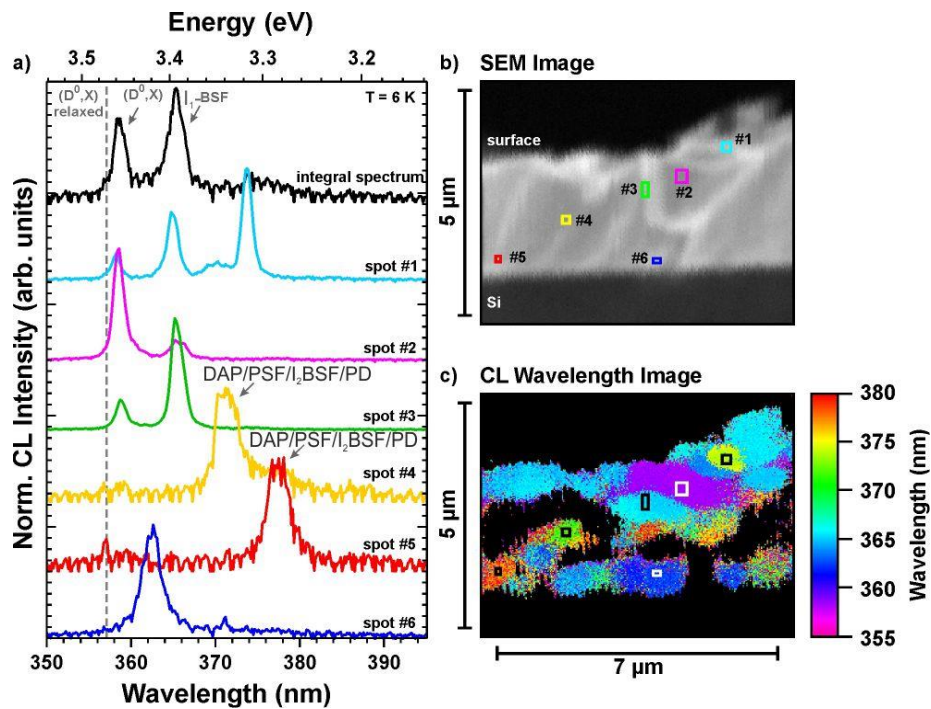
Fig. 4.7: *Local spectra (a) at the cross section shown in the SEM image (b) and the corresponding CL wavelength image (c) of the sample grown on Si(113). The local spectra depict no reduction of I_1-BSF emission by the interlayer.*

Fig. 4.8 shows SEM images and CL line scans along the cross section of the GaN grown on Si(112) and Si(113).
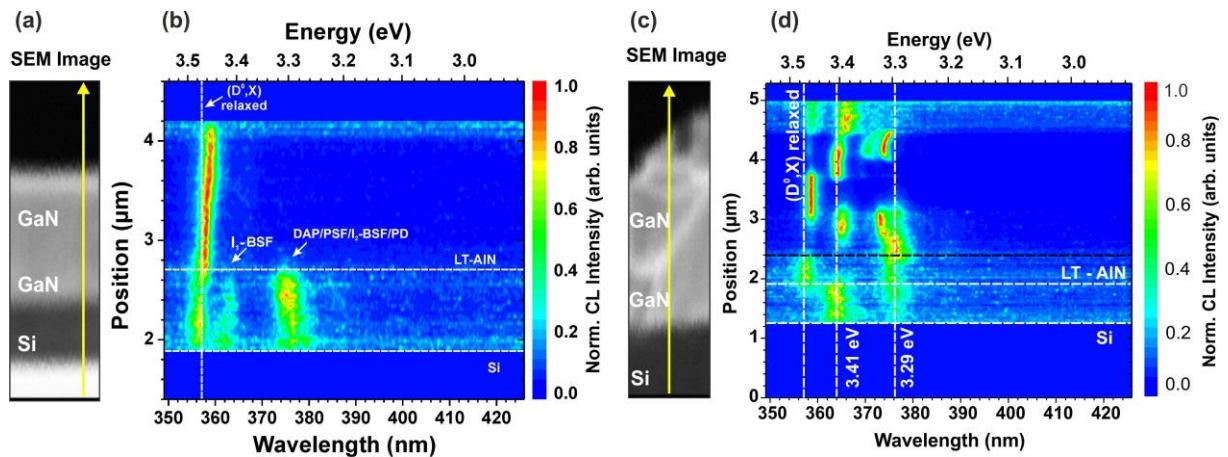
Fig. 4.8: *SEM images and CL line scans recorded along the cross section of the sample structures grown on Si(112) (a and b) and on Si(113) (c and d) at 6 K. Here, one can see the significant effect of the LT-AlN interlayer for GaN grown on Si(112) in improving the GaN layer quality, namely reducing I_1-BSFs and DAP/PSF/I_2-BSF/PD related emission when compared to non-optimized GaN grown on Si(113).*

A dominating (D^0,X) luminescence is found in the upper GaN layer with a slight red-shifting due to increasing tensile stress (Fig. 4.8 (b)). In contrast, the lower GaN layer shows I_1-BSF and DAP/PSF/I_2-BSF/PD related emissions.

In comparison, a CL line scan of the non-optimized GaN based layer structure grown on Si(113) does not show any defect reduction (Fig 4.8 (d)).

I_1-BSFs can be stopped, if the LT-AlN interlayer grows parallel to the substrate surface and sufficiently thick to result in lattice relaxation. This requires an optimization of the thickness and height position of the inserted LT-AlN interlayer.

4.2.3 TEM and STEM measurements

TEM and STEM measurements of GaN on Si(112) and Si(113) were performed for further investigations (Fig. 4.9). STEM annular dark field (ADF) images show that the LT-AlN interlayer eliminates I_1-BSFs, which originate at the AlN / Si interface (Fig. 4.9 (a), (b)).
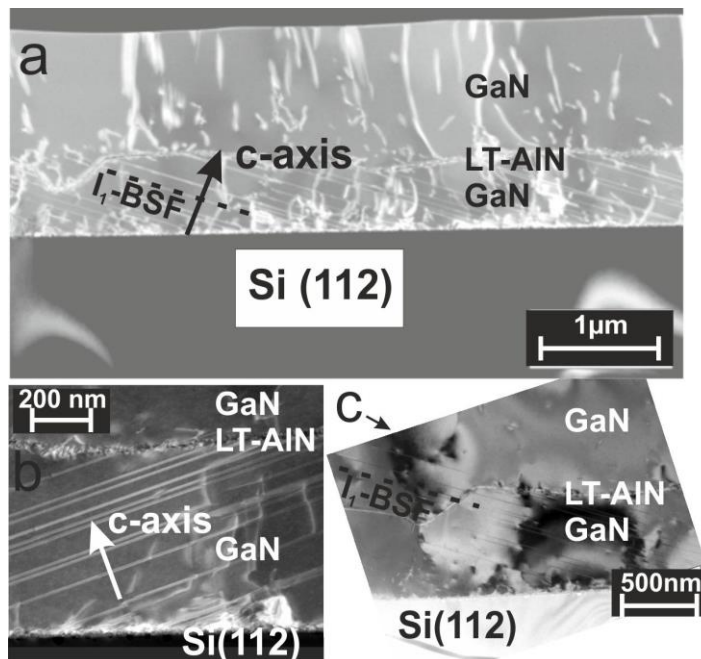
Fig. 4.9: *(a) and (b) show STEM(ADF) cross sectional images of the GaN layer with a LT-AlN interlayer. I$_1$-BSFs are eliminated at the LT-AlN interlayer. (c) shows the TEM (bf) image of a position, where I$_1$-BSFs cross the LT-AlN interlayer. I$_1$-BSFs are highlighted by black dashed lines.*

The I_1-BSF defect density is reduced in the upper GaN layer to 2×10^4 cm^{-1} compared to that in the lower GaN layer (10^5 cm^{-1}). Fig. 4.9 (c) shows a TEM bright field (bf) image of a position where the LT-AlN interlayer is not grown parallel to the substrate surface having large faceted steps. At such positions I_1-BSF can go through the LT-AlN interlayer and are not eliminated in contrast to regions where the LT-AlN is parallel to the substrate surface. In comparison the STEM(ADF) image of GaN on Si(113) (Fig. 4.10) shows many I_1-BSFs in the upper GaN layer. Here the structure needs to be optimized to achieve a smooth surface prior to LT-AlN growth.
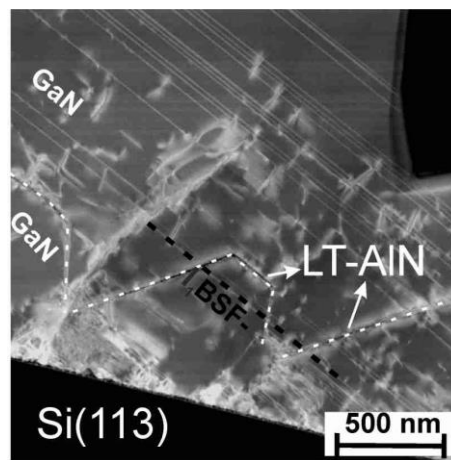
Fig. 4.10: *STEM(ADF) image of GaN on Si(113) with high I_1-BSF density. The LT-AlN interlayer and an I_1-BSF are marked by white and black dashed lines respectively.*

4.2.4 STEM-CL measurements

As mentioned in chapter 2, a direct nano-scale correlation of structural and optical properties of the sample is possible by using low temperature cathodoluminescence spectroscopy (T < 20 K) in a STEM. Fig. 4.11 shows a detailed view by cross sectional STEM(ADF) and monochromatic CL-intensity images of sample MD5818 grown on Si(112). These images exhibit the microscopic origin of luminescence: in the STEM(ADF) image (Fig 4.11 (a)) dislocations and BSFs are shown as bright contrast lines, whereas the BSFs density is reduced by the LT-AlN interlayer in the upper GaN layer. Furthermore, it has been found that with increasing layer thickness larger dislocation-free areas can appear. As shown in Fig. 4.11 (c), many BSFs are visible below the LT-AlN interlayer accompanied by their characteristic luminescence. Above the LT-AlN layer, only very few stacking faults remain, of which a dominant example is marked by a blue dashed line. In Fig. 4.11 (b), the dominating (D^0,X) luminescence intensity of around 358 nm can be correlated to dislocation

and stacking fault free areas compared to the I_1-BSF luminescence at 364 nm, which is directly correlated to the diagonally propagating stacking fault planes (Fig. 4.11 (c)). At a wavelength of 376 nm, a DAP/PSF/I_2-BSF/PD related luminescence is shown, always in the vicinity of I_1-BSFs (Fig. 4.11 (d)). Further information about the optical investigation of these samples can be found in [Schmidt 2011, Müller 2010] and references therein.
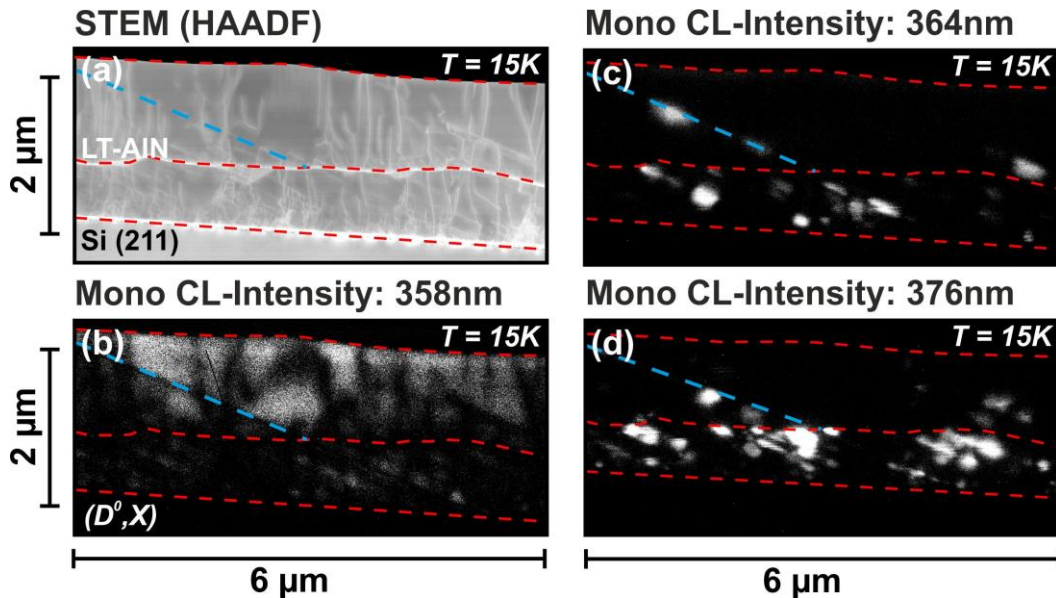
Fig. 4.11: *(a) STEM(ADF) image and monochromatic STEM-CL images of sample MD5818 grown on Si(112): (b) CL-intensity images of (D^0,X) luminescence, (c) I_1-BSF luminescence, and (d) luminescence at 376 nm. The position of an I_1-BSF in the upper layer is marked by the blue dashed line. Si/AlN, GaN/LT-AlN and GaN/vacuum interfaces are marked by red dashed lines.*

4.3. Optimized semi-polar GaN layers grown on Si(113)

As described in chapter 3, GaN growth on Si(11h) is essentially c-axis oriented growth on the naturally occurring Si(111) facet planes of high index Si(11h) surfaces. The Si(111) plane fraction on the surface of Si(113) substrates is smaller than that on Si(112) substrates (64% for Si(112), and 46% for Si(113)). Thus, a higher melt-back etching tendency for layers grown on Si(11h) substrates with higher h values was observed. The sample (MD6677) was grown on Si(113) under optimized growth conditions for Si(113) orientation. Here an optimized 12 nm thick (3 min) seeding layer was deposited at 710 °C, 20 sccm TMAl flow and 100 mbar reactor pressure. In the second GaN layer, N_2 was used as carrier gas. The layer structure is shown in Fig. 4.12.
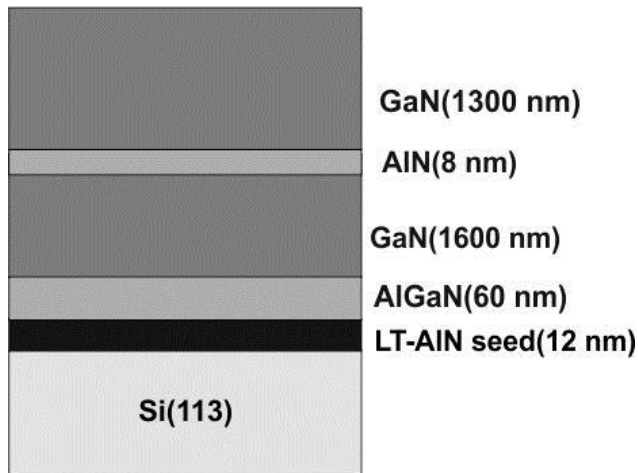
Fig 4.12: *layer structures of sample MD6677.*

To characterize the sample, top view and cross sectional FE-SEM images were performed as shown in Fig. 4.13. This sample shows a smooth surface with some small pits. As shown in the cross sectional image (Fig. 4.13, (b)) the LT-AlN interlayer was inserted after ~ 1.6 µm GaN growth and grows parallel to the substrate surface. The thickness of the GaN layer above LT-AlN interlayer is ~ 1.3 µm.
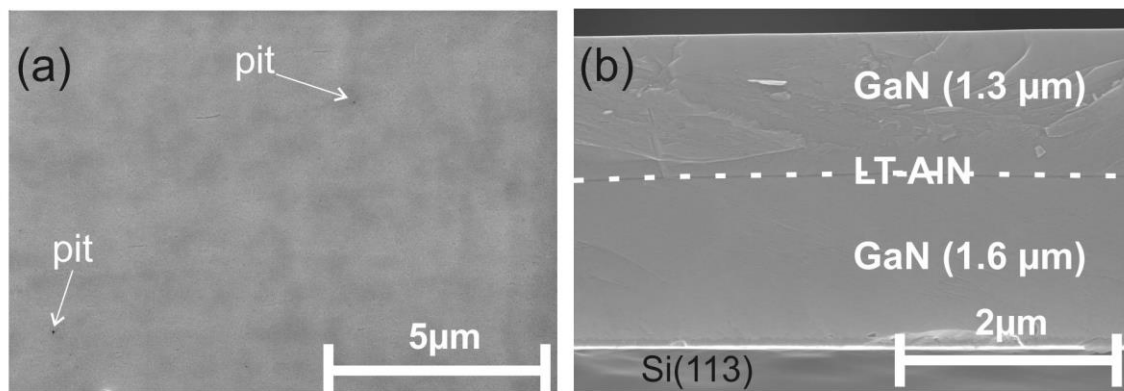
Fig: 4.13: *FE-SEM images of GaN layer (a) top-view and (b) cross section.*

I_1-BSF elimination by LT-AlN interlayer is shown in Fig. 4.14, which presents a STEM(ADF) image of GaN layers grown on Si(113). By an optimization of the GaN growth parameters a partially relaxed LT-AlN interlayer between two GaN layers resulting in an I_1-BSF reduction in the upper GaN layer is obtained. The c-axis of this optimized GaN grown on Si(113) is tilted by ~ 21° with respect to the surface normal vector in comparison to 26° as usually obtained and the theoretically expected value of 29.5°. The reason of this large inclination angle deviation is not clear. Thus, the GaN $(10\bar{1}5)$ plane is nearly parallel to substrate surface.
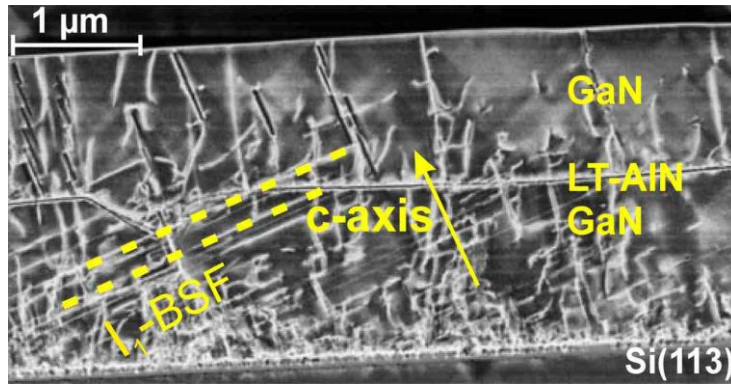
Fig. 4.14: *STEM(ADF) image of the optimized GaN structure on Si(113) (sample MD6677).*

4.4 Mechanism of stacking faults reduction

As presented in this chapter, LT-AlN interlayers can give rise to a reduction of the I_1-BSF density in the upper GaN layer. A mechanism is proposed explaining the reduction of I_1-BSFs at the LT-AlN interlayer by the formation of Frank-Shockley partial dislocations ($\vec{b} = 1/6\langle 20\bar{2}3\rangle$), which contribute to the relaxation of AlN/GaN misfit strain.

It has been reported that partial dislocations (PD) with a Burgers-vector of $\vec{b} = 1/6\langle 20\bar{2}3\rangle$ are involved in misfit strain relaxation via I_1-BSFs generation for the m-planar InGaN/GaN interface [Fischer 2009]. There, it has been observed that the $Ga_{0.67}In_{0.33}N$ layer is fully relaxed in c-axis direction for a thickness of 8 nm. Partial strain relaxation by stacking fault generation in InGaN multiple quantum well (MQW) grown on semi-polar $(1\bar{1}01)$GaN layers has also been reported by Wu et al. [Wu 2011]. In the case of InGaN/GaN MQW growth on m-plane GaN, the wider InGaN in-plane lattice parameter requires a reduction in the number of stacked layers in c-direction upon InGaN strain relaxation leading to I_1-BSF generation. But at the AlN/GaN interface, AlN has a smaller lattice parameter than GaN. Thus one can assume that in order to obtain relaxation of the AlN layer, the insertion of additional lattice planes is required [Dadgar 2011].
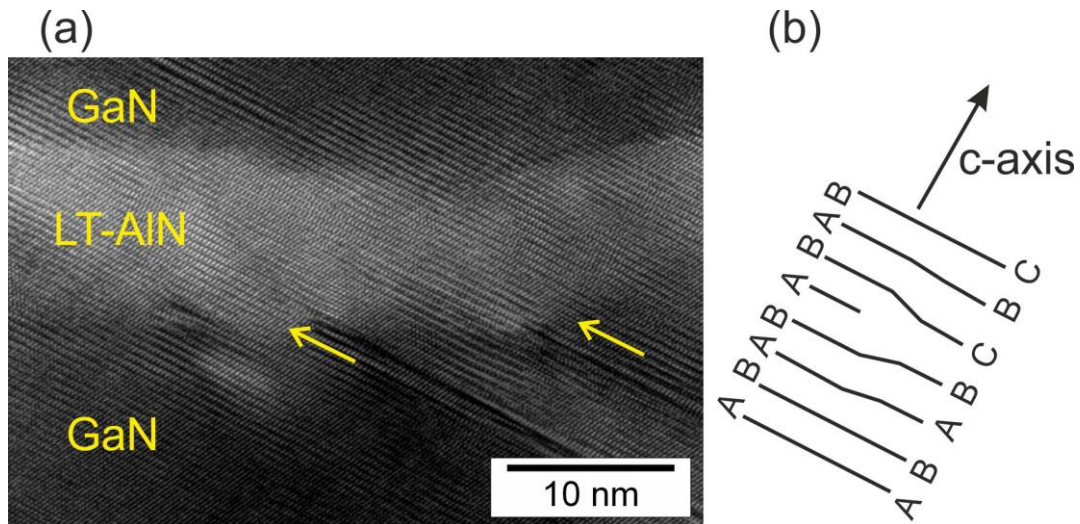
Fig. 4.15: *(a) HRTEM image, the arrows mark the position of the I₁-BSF, (b) a model showing I₁-BSF elimination. The sample is grown on Si(113) as shown in Fig. 4.14 (sample MD6677).*

As shown in Fig. 4.15 (a) the insertion of a LT-AlN interlayer in GaN films grown on Si(113) leads to a reduction in I_1-BSF density. The majority of I_1-BSFs are eliminated at the LT-AlN interlayer. The I_1-type basal plane stacking fault is eliminated by the insertion of an extra c-half plane and subsequent shear of $1/3\langle 10\bar{1}0\rangle$ and changes the stacking sequence to the original (Fig. 4.15 (b)).

For a better understanding of the underlying mechanism behind the I_1-BSF reduction, a sample grown on Si(112) (Fig. 4.3) was investigated with aberration corrected high resolution TEM (HRTEM) and HRSTEM Z-contrast by T. Markurt et al at IKZ Berlin. The combined HRSTEM investigation in the $\langle 11\bar{2}0\rangle$ projection reveals that I_1-BSFs are eliminated at the lower interface of the LT-AlN interlayer (Fig. 4.16 (a)). The LT-AlN interlayer appears darker in the corresponding STEM Z-contrast image (Fig. 4.16 (b)). The lower STEM Z-contrast intensity is caused by the smaller mean atomic number Z of the LT-AlN interlayer compared to the GaN matrix [Pennycook 1990]. From the characteristic disturbed stacking sequence (AB **ABC** BC) in the lower GaN layer (Fig. 4.16 (c)) the eliminated BSFs were identified as I_1-type [Zakharov 2005]. Another important observation is that inserted (0001) and $(10\bar{1}0)$ half-planes are found at the AlN/GaN interface directly at the eliminated I_1-BSF. The inserted lattice planes correspond to a Frank-Shockley PD with a Burgers-vector of $\vec{b}=1/6\langle 20\bar{2}3\rangle$ which bounds the I_1-BSF. A simple model shown in Fig. 4.16 (d) illustrates these observations.
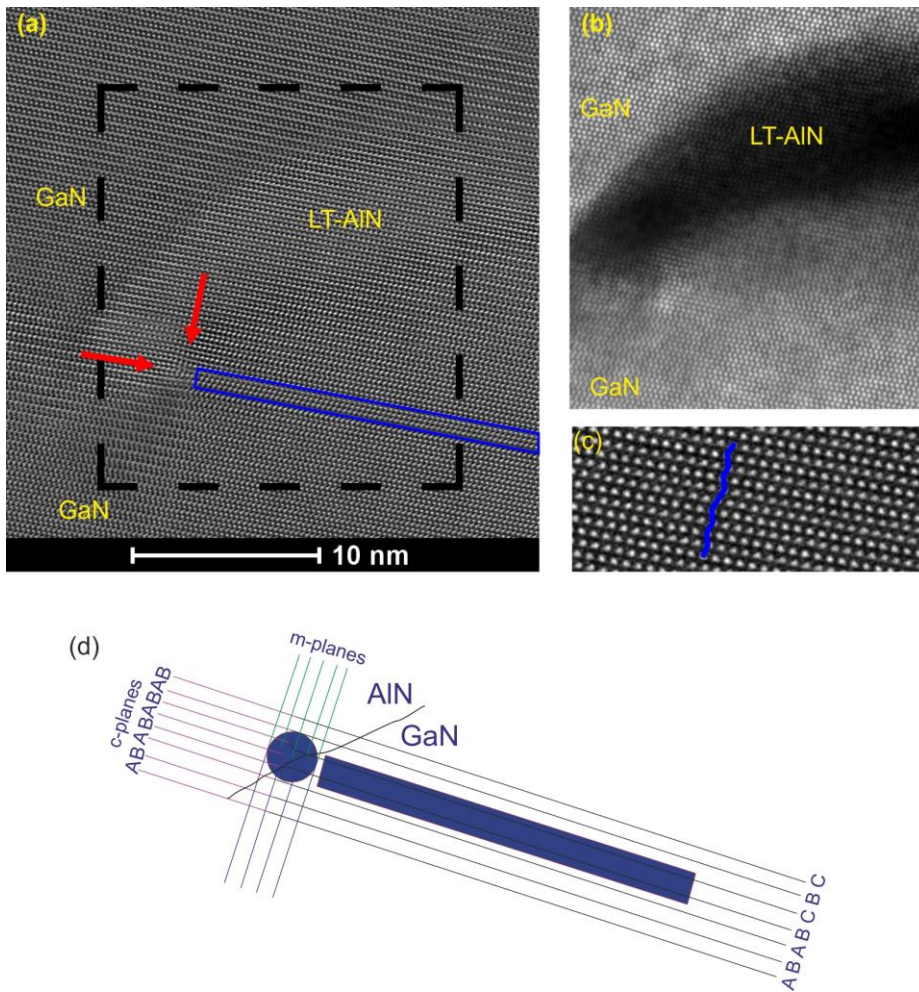
Fig 4.16: *(a) HRTEM image in the $\langle 11\bar{2}0 \rangle$ projection of an I_1-BSF (blue rectangle), which is eliminated at the interface of the LT-AlN interlayer. The inserted $\left(10\bar{1}0\right)$ and $\left(0001\right)$ half planes, which correspond to the Frank-Shockley PD ($\vec{b} = 1/6\langle 20\bar{2}3 \rangle$) bounding the I_1-BSF, are indicated by red arrows. (b) shows the region within the rectangle (black dashed line in (a)) in HR(S)TEM Z-contrast. (c) is a magnified HRTEM image of an I_1-BSF indicating its characteristic AB AB **ABC** BC BC stacking (blue line). (d) model of I_1-type stacking fault elimination via the insertion of m- and c-half planes (sample MD5818 grown on Si(112)).*

The hexagonal closed-packed (hcp) (AB AB AB) stacking of the wurtzite lattice is restored on the one hand by the insertion of an extra basal half-plane ($\vec{b} = 1/2\langle 0001 \rangle$). In Fig. 4.16 (d) this is an inserted "A" $\left(0001\right)$ half-plane. On the other hand, a subsequent shear of the crystal by $\vec{b} = 1/3\langle 10\bar{1}0 \rangle$ (transforms "C"$\rightarrow$"B" and "B"$\rightarrow$"A" in Fig. 4.16 (d)) is required to fully restore the hcp stacking sequence. It can thus be assumed that the elimination

of I_1-BSFs occurs by the formation of Frank-Shockley PDs at the interface of the LT-AlN interlayer.

The dislocation formation itself can be understood in terms of plastic relaxation of the AlN/GaN misfit strain. Because the Frank-Shockley PDs bound the eliminated I_1-BSFs, their line direction is defined by the form of these planar defects. In the present work, the boundary of the eliminated I_1-BSFs is approximately the intersection of the basal plane (0001) including the I_1-BSF with the interfacial plane $(10\bar{1}6)$ of the LT-AlN interlayer, i.e. the $\langle 11\bar{2}0 \rangle$ direction (actually the line direction is parallel to the viewing direction in Fig. 4.16).

The angle between the line direction and the Burgers-vector of the Frank-Shockley PDs is non-zero and therefore the Frank-Shockley PDs have an edge component which relieves part of the misfit strain. Thereby, the inserted m- as well as the c-half planes contribute to the plastic relaxation of the AlN/GaN misfit [Markurt 2012].

Two questions remain open: firstly, why do I_1-BSFs protrude the LT-AlN interlayer at the position of growth pits or larger faceted steps at the LT-AlN interlayer (see Fig. 4.17 (a))?

A possible explanation lies in the thickness of the LT-AlN interlayer. As shown in Fig. 4.17, the thickness of the LT-AlN interlayer perpendicular to the AlN/GaN interface is smaller at pit sidewalls (~ 8 nm) than on horizontal surfaces (> 10 nm). It is well known in literature that in heteroepitaxial growth plastic relaxation of a strained layer occurs only for layer thicknesses above a critical value [Van der Merwe 1963, Matthews 1970, Matthews 1974, People 1985].
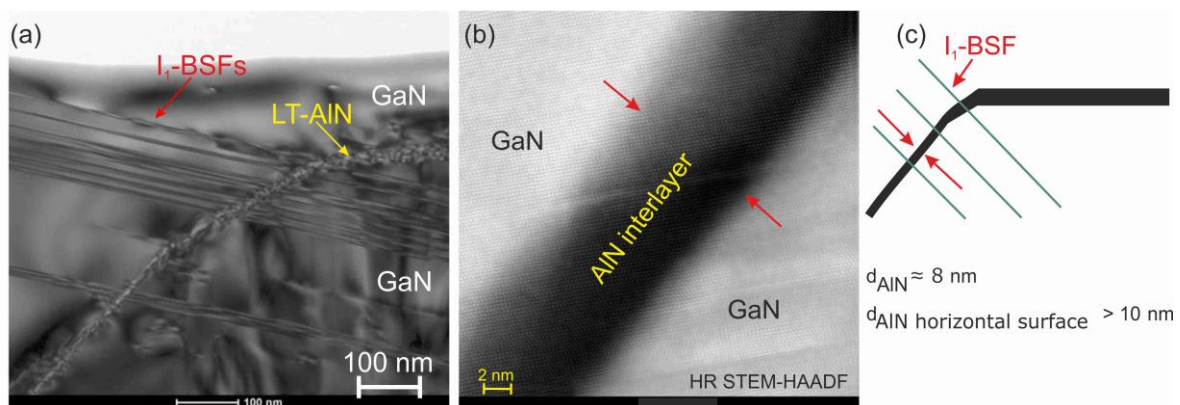
Fig. 4.17: *(a) TEM bright field image showing a position without I_1-BSF elimination by LT-AlN. (b) HR STEM-HAADF image, (c) a model showing the thickness of the LT-AlN interlayer at different positions.*

In terms of a critical thickness model our observations can be interpreted in such a way that in the case of the pit sidewalls the critical thickness for the formation of an extra Frank-Shockley PD and thus elimination of I_1-type BSFs is not yet reached. Therefore the I_1-BSF density is not reduced by the LT-AlN interlayer at such positions.

The second remaining question is: Are new BSFs generated at the upper AlN/GaN interface similar to InGaN on GaN?

Cross sectional TEM imaging (Fig. 4.18 (a)) reveals that new BSFs can be generated at the upper interface of the LT-AlN interlayer. However, from an analysis of the stacking sequence AB AB **ABCA** CA CA it was found that in contrast to the eliminated I_1-BSF, these BSFs are of I_2-type [Zakharov 2005]. This stacking sequence is shown as a blue line in Fig. 4.18 (b), whereas the zigzag line represents a wurtzite lattice (AB AB or CA CA) and the straight part represents a cubic lattice (ABCA). Another difference is that the I_2-BSFs do not expand through the whole sample, but are limited in their length between 5 nm to a maximum of 100 nm. The newly generated I_2-BSFs are bound at each side by Shockley partial dislocations ($\vec{b} = 1/3\langle 10\bar{1}0\rangle$). The inserted lattice planes of both Shockley PDs bounding the I_2-BSF can be seen by tilting the TEM specimen from the $\langle 11\bar{2}0\rangle$ projection by 30° around the c-axis and imaging in the $\langle 1\bar{1}00\rangle$ projection (Fig. 4.18 (c)). Here red lines show the vertical planes and red rows indicate the interpolated $(10\bar{1}0)$ planes. A complete Burgers-circuit around the full I_2-BSF (including both Shockley PD) leaves a shift of $\vec{b} = 1/3\langle 11\bar{2}0\rangle$, i.e. a full a-type misfit dislocation, which relaxes the misfit between GaN/AlN at the upper interface of the LT-AlN interlayer. Since in investigated samples the basal planes are inclined with respect to the GaN/AlN interface, the primary glide-system $1/3\langle 11\bar{2}0\rangle|(0001)$ in the wurtzite crystal is activated and shear stresses are present. Thus full a-type dislocations dissociate into two Shockley partial dislocations, which then spread apart by glide on the basal plane and produce an I_2-type BSF in between [Zakharov 2005].

$$\vec{b}_{full} \rightarrow \vec{b}_{partial1} + \vec{b}_{partial2} \qquad (12)$$

$$\tfrac{1}{3}\langle 11\bar{2}0 \rangle \rightarrow \tfrac{1}{3}\langle 10\bar{1}0 \rangle + \tfrac{1}{3}\langle 01\bar{1}0 \rangle \qquad (13)$$

The splitting into two PDs is driven by the reduction in the self-energy of the dislocation, which depends on the square of the Burgers-vector.

$$E_{disloc} \sim \vec{b}^{2} \qquad (14)$$

$$\left(\tfrac{1}{3}\langle 11\bar{2}0 \rangle\right)^{2} \rangle \left(\tfrac{1}{3}\langle 10\bar{1}0 \rangle\right)^{2} + \left(\tfrac{1}{3}\langle 01\bar{1}0 \rangle\right)^{2} \qquad (15)$$

Since $\left|\langle 11\bar{2}0 \rangle\right| = 3a$, $\left|\langle 10\bar{1}0 \rangle\right| = \left|\langle 01\bar{1}0 \rangle\right| = 2m$, $m^{2} = \tfrac{3}{4}a^{2}$, then

$$a^{2} \rangle \tfrac{1}{3}a^{2} + \tfrac{1}{3}a^{2} \qquad (16)$$

where $\vec{b}^{2}$ is the square of Burgers-vector and a, m are lattice constants respectively. Fig. 4.18 (d) shows a simple model to illustrate this dissociation. We can thus assume that the I$_2$-BSFs newly generated at the upper interface of the LT-AlN interlayer are formed by the dissociation of a full a-type misfit dislocation. However, the important point is that these I$_2$-BSFs do not expand through the whole layer, but are limited in their length to approximately a few 10 nm [Markurt 2012].
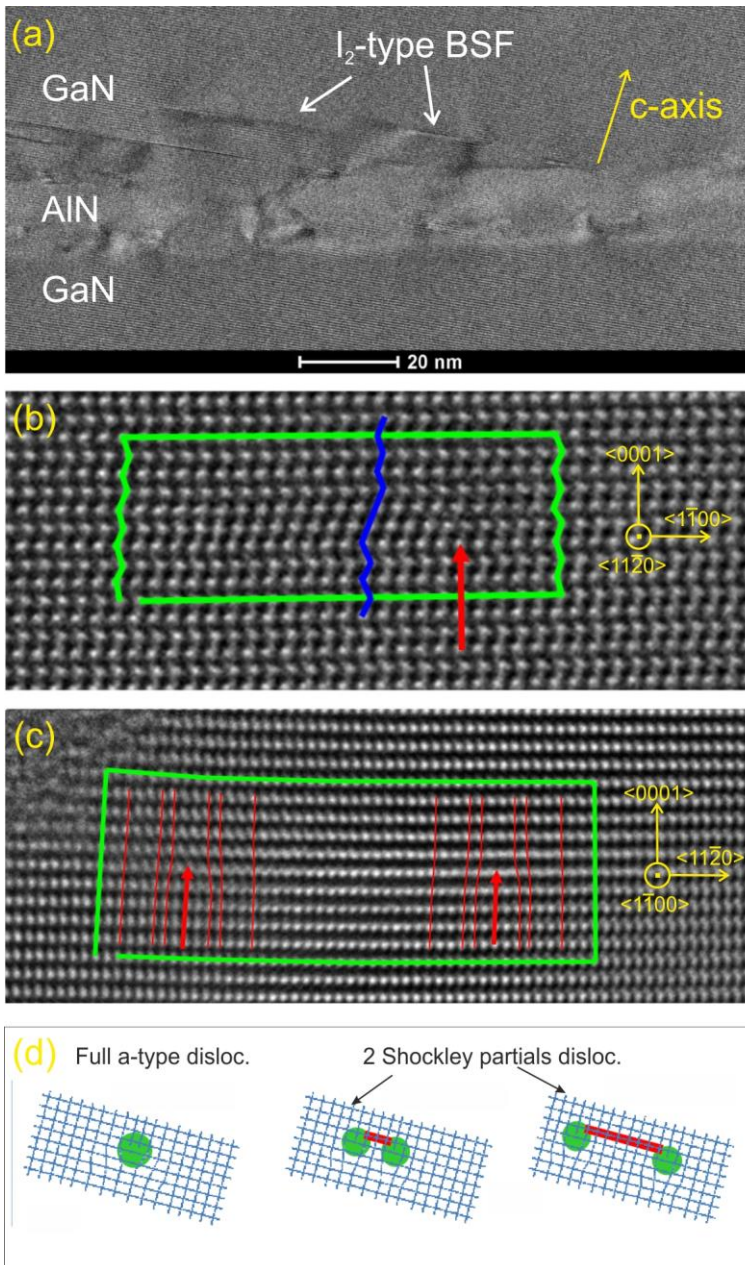
Fig. 4.18: *(a) cross sectional TEM showing the formation of new I_2-BSFs at the upper AlN/GaN interface of the LT-AlN interlayer. (b) displays a magnified HRTEM image in the $\langle 11\bar{2}0 \rangle$ projection of an I_2-BSF indicating its characteristic disturbed stacking sequence AB AB **ABCA** CA CA (blue line). In (c) the same SF is viewed in the $\langle 10\bar{1}0 \rangle$ projection by tilting the specimen by 30°. In this projection the inserted $(10\bar{1}0)$ half-planes of both Shockley PD bounding the SF can be seen (red arrow). In both HRTEM images the Burgers-circuit is indicated by a green frame and reveals a full a-type misfit dislocation (b=1/3$\langle 11\bar{2}0 \rangle$). (d) This model demonstrates the dissociation of a full a-type dislocation into two Shockley partials dislocation (green circle) bounding an I_2-BSF (red line) between them.*

5 Semi-polar GaN LEDs structures

An efficient LED requires a high quality InGaN/GaN quantum well structure, which means a good carrier confinement and high carrier injection effieciency. Therefore an optimized buffer structure for minimum defect density and highly n-type and p-type doped layers is necessary.

As mentioned in chapter 2, compared to commercially available devices grown in the c-axis oriented GaN direction, the efficiency of a GaN-based LED can be significantly improved by semi- and non-polar device structures with reduced or eliminated QCSE [Yoshizumi 2009]. For all LED structures investigated in this work n-type and p-type layers were achieved by Si- and Mg-doping respectively. In this chapter, properties of semi-polar GaN LED structures on non-patterned Si(112) and Si(113) substrates are presented and discussed.

5.1 Semi-polar LED structure grown on Si(112)

The basis for the semi-polar LED structure is a high quality GaN buffer layer grown on the optimized seeding layer for each substrate orientations, as described in chapter 4.

Two device structures were investigated (Fig 5.1). The first one (sample 1) consists of a thin (~ 4 nm, 15 s) LT-AlN seeding layer grown at high Al-flux (100 sccm), nominal growth temperature (720 °C) and 100 mbar reactor pressure on a Si(112) substrate. Since the thin (~ 4 nm) AlN seeding layer cannot fully avoid the meltback etching effect, an AlGaN layer (~ 60 nm) was grown on top of the seeding layer. Subsequently, a GaN layer (~ 0.8 μm) with an AlN interlayer (~ 8 nm) was deposited followed by a n-tpye GaN:Si (~ 0.8 μm) layer. The necessary strain engineering and BSF-defect reduction is carried out by the inserted AlN (~ 8 nm) interlayer. On top of this optimized buffer layer, a fivefold GaN/InGaN QW structure was grown followed by the final GaN:Mg (~ 100 nm) cap layer. Samples 2 and 3 were grown under nearly the same nominal growth conditions as sample 1 with the following important differences. A thin (~ 8 nm, 2 min) LT-AlN seeding layer was grown at low Al-flux (20 sccm), 100 mbar reactor pressure on a Si(112) substrate. An (~ 60 nm) AlGaN (~ 50 % Al concentration) interlayer was deposited. Samples 2 and 3 were grown at the LT-AlN seeding layer nominal growth temperature at 690 °C and 710 °C respectively. In contrast to samples 2 and 3, which were grown one after the other in series, sample 1 was grown in a separate series with different growth parameters for the LT-AlN seeding layer.
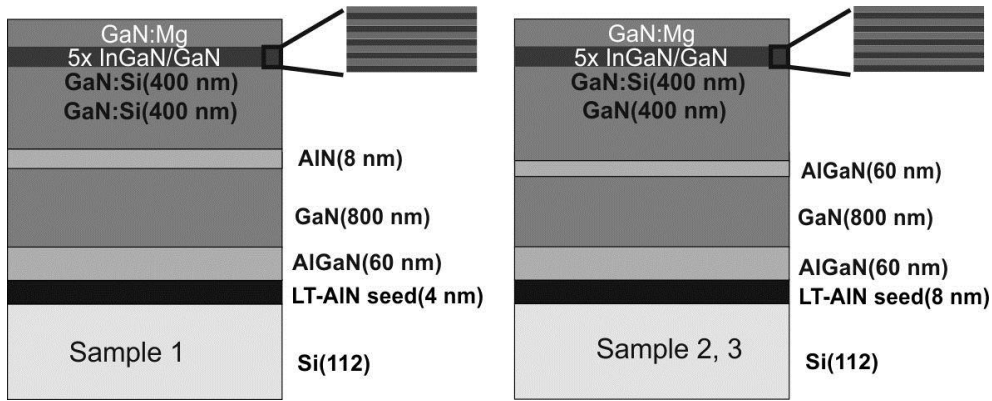
Fig. 5.1: *Layer structures of samples 1, 2, and 3. (sample 1: MD7018 (720 °C), (sample 2: MD7078 (690 °C)), (sample 3: MD7075 (710 °C)). The temperatures are the seeding layer set points in the growth recipe.*

5.1.1 Structural properties of GaN/InGaN MQWs

For sample 1, the X-ray investigation shows nearly $(10\bar{1}6)$ oriented GaN films grown on Si(112) leading to a c-axis inclination angle of ~ 18° with respect to the surface normal. The mosaic tilt was determined by a ω-scan of the nearly symmetric $(10\bar{1}6)$ reflection with a FWHM of 0.48°. A GIID ω-scan of a GaN $(11\bar{2}0)$ reflection yields a FWHM of 0.8° for the twist. For further investigations of the InGaN/GaN MQW quality, a HR-XRD θ/2θ-scan on the GaN $(10\bar{1}6)$ reflection was performed. Fig.5.2 does not show a very sharp InGaN/GaN interference pattern. The broadening of the superlattice peaks is determined by the fluctuation of QW-thickness and composition. The simulation of the GaN/InGaN MQW yields thicknesses of ~ 8 nm and ~ 2.8 nm, which show a close agreement to the thickness determined by TEM. The simulation is performed by applying a program (Leptos Bruker AXS-GmbH), which is developed for c-axis oriented GaN and cannot simulate semi-polar GaN structures. Since the 2θ value of the GaN $(10\bar{1}6)$ diffraction peak is close to that of GaN (0006), GaN $(10\bar{1}6)$ was simulated as GaN (0006). The HR-XRD measurements show nearly the same results for sample 2 and 3 (not shown here).
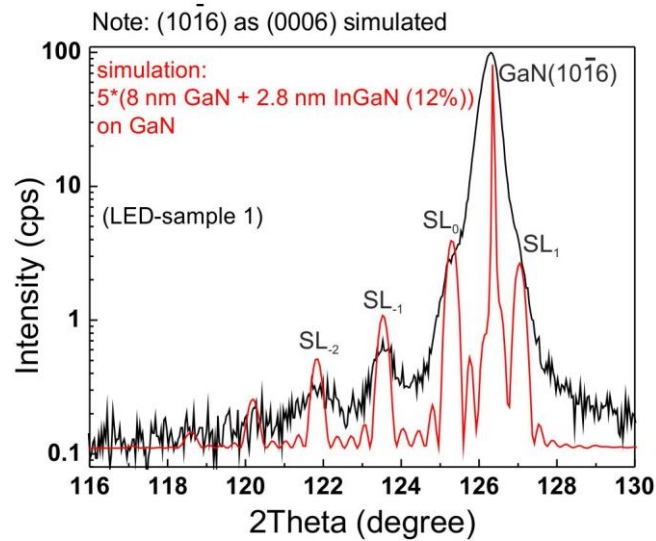
Fig. 5.2: *HR-XRD* $\theta/2\theta$-*scan of the GaN* $(10\bar{1}6)$ *reflection (black line) and its simulation (red line) showing the expected superlattice fringes.*

5.1.2 Dependence of c-axis inclination angle on AlN seeding layer growth temperature

As mentioned in chapter 3, the c-axis inclination angle of the GaN layers depends on growth temperature and thickness (growth time) of the AlN seeding layer. GaN layers are grown along a polar c-direction using a high temperature AlN seeding layer. The angle of c-axis inclination increases if the AlN seeding layer growth temperature decreases. This effect is shown using reciprocal space mapping (RSM) measurements. In the following section, the properties of the three samples mentioned above, which were grown at different LT-AlN seeding layer temperatures, are presented (Fig. 5.1). Since the angle of the c-axis inclination in sample 1 is in the same category of those in samples 2 and 3, the RSM-measurements of these samples are presented together.

Reciprocal space maps

RSMs of GaN $(10\bar{1}6)$ and GaN (0004) reflections were performed by using a Seifert URD6 diffractometer with a position sensitive detector. RSM investigations simultaneously supply information on the crystalline quality and the strain state of the GaN/InGaN layers. Fig. 5.3 shows nearly symmetric RSM images of samples 1, 2 and 3. It is observed that the maximum positions of the GaN $(10\bar{1}6)$ reflections vertically align to those of the InGaN MQW for all samples and they are on one line, which is parallel to q_z. This means that they

have the same q_x value. It shows that the MQW superlattice fringes, i.e. the interfaces of the MQW layers are parallel to the substrate surface. Black lines denote the $(2\theta/\omega)$ offset scans. If the maximum position of the GaN and the SL_0 (QW with n=0) peaks lie on the $(2\theta/\omega)$ offset scans, then the lattice planes of the GaN and InGaN MQW are parallel to each other. For all three samples the black lines have tilt angles with respect to q_z. They indicate different tilt angles of GaN $(10\bar{1}6)$ towards the substrate surface depending on the AlN seeding layer growth temperature and thickness. Thus q_x of the GaN $(10\bar{1}6)$ is not equal to zero (If $\theta=\omega$ then $q_x=0$ and GaN $(10\bar{1}6)$ lies parallel to the Si(112) surface). Tilt angles of GaN $(10\bar{1}6)$ with respect to the substrate surface normal are measured as 17.73°, 15.05° and 13.21° for samples 1, 2 and 3, respectively. However, the c-axis inclination angle of the InGaN MQW can be controlled by the AlN seeding layer growth temperature and thickness. The QW interfaces and sample surfaces are parallel to the substrate surface. The polarization field in growth direction can be reduced if the c-axis inclination angle increases.
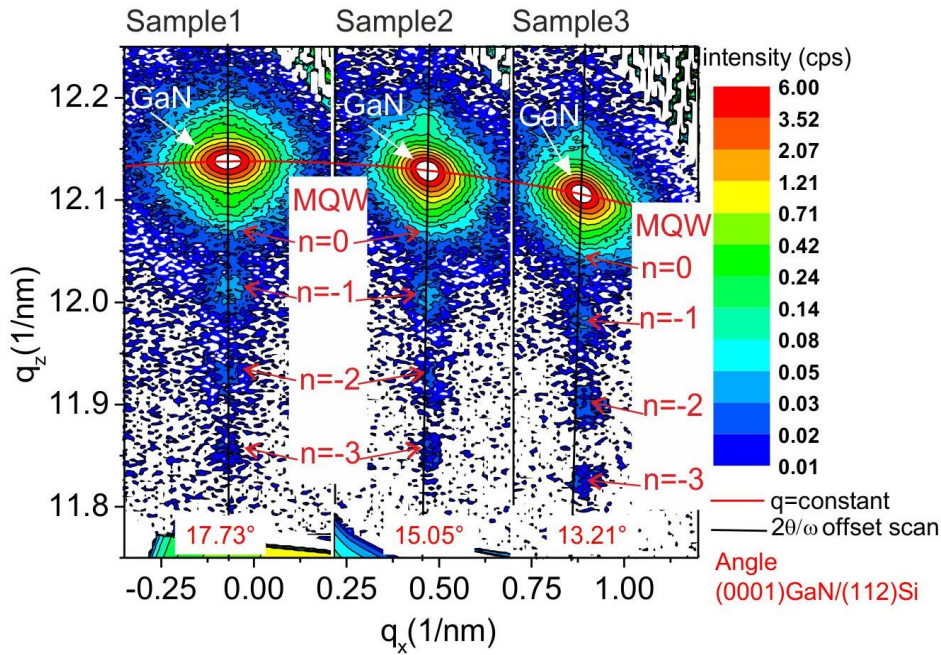
Fig. 5.3: *Nearly symmetric RSM images of the GaN $(10\bar{1}6)$ reflections of samples 1, 2 and 3. Black lines indicate the $(2\theta/\omega)$ offset scans. All points that lie on the red line have the same scattering vector $|\vec{q}|$.*

A RSM around the asymmetric GaN (0004) X-ray diffraction of sample 3 is presented in Fig. 5.4. The diffraction spots from the GaN layer and InGaN superlattices lie at the same q_x value and show no sign of relaxation (relaxation line marked by the red line). Consequently, the InGaN MQW layers are pseudomorphically grown on the GaN layer.
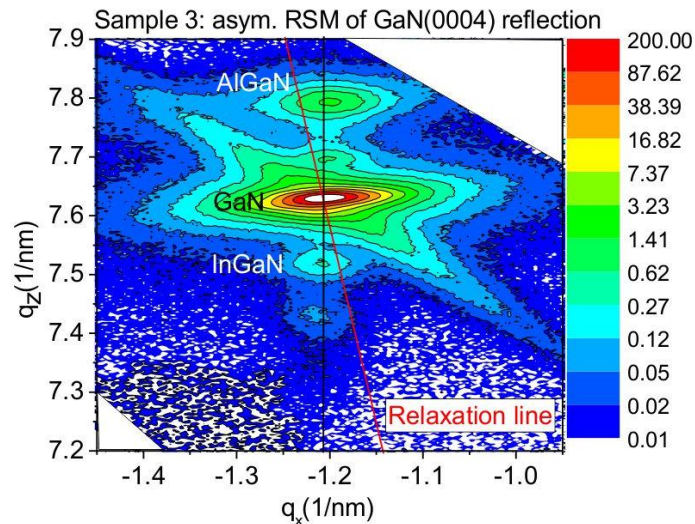
Fig. 5.4: *Asymmetric RSM of the GaN reflection of the sample 3. The red line shows the relaxation line. The black line is parallel to q_z.*

FE-SEM measurements

The surface morphologies of samples 1, 2, and 3 are shown in Figs. 5.5 (a), (b) and (c), respectively. A smooth surface morphology with a few pits is obtained for each sample. The larger pits are observed for sample 1, whereas the pit size decreases for samples 2 and 3.
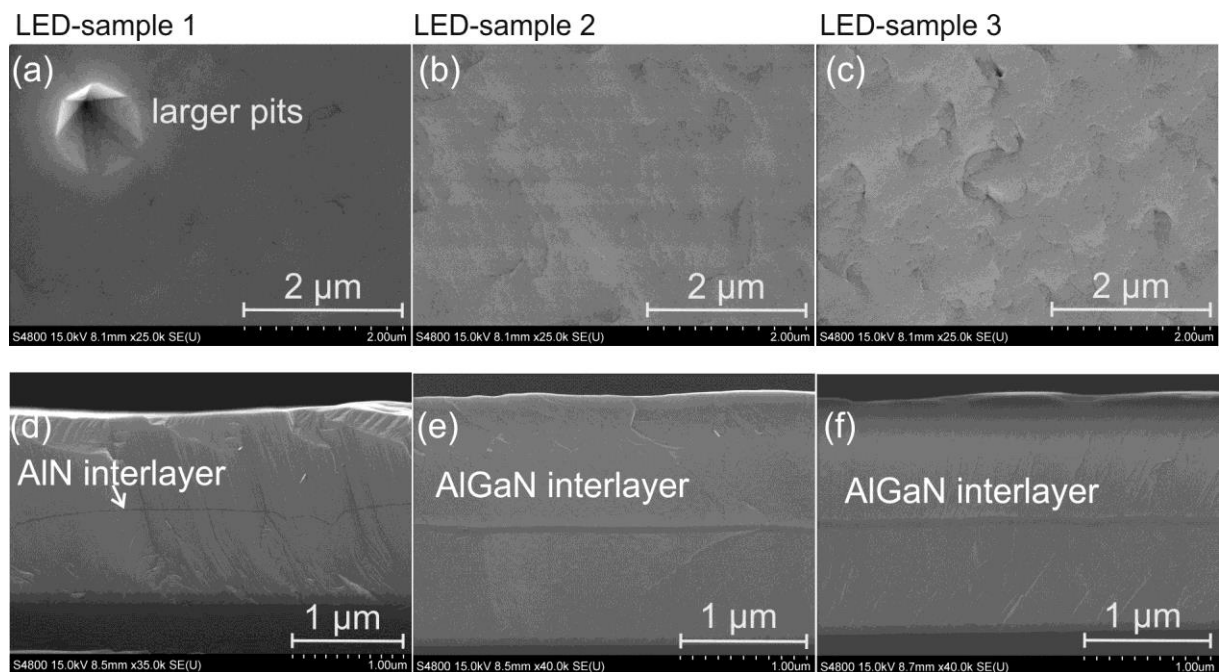
Fig. 5.5: *FE-SEM images of samples 1, 2 and 3: the images on top (a, b, c) show surface morphology and those on bottom (d, e, f) show cross sectional images of the total structures of each samples.*

Cross sectional images of these LED structures are shown in Fig. 5.5 (d, e, f). A nearly planar growth of the (AlN and AlGaN) interlayers is observed for all three samples. CL measurements (not shown here) show an improvement of the GaN layer quality, which is grown on top of the LT-AlN and AlGaN interlayers for all samples.

TEM measurements

For further investigations of the structural properties of sample 1, which has larger v-shaped pits on its surface, STEM(HAADF) and TEM(bf) measurements were performed. The V-defects mostly originate in the initial three dimensional growth of the structure and an incomplete coalescence. Fig. 5.6 (a) and (b) show an undulated large faceted position of GaN/AlN/GaN layers which leads to a v-shaped surface pit. At this position, a deformation of the MQW structure and an inhomogeneous planar growth are found. Fig. 5.6 (c) indicates that the MQW thickness changes at such defect positions causing locally selective indium incorporation. The thickness of InGaN and GaN layers of the MQW is ~ 3 nm and ~ 8.5 nm respectively.

TEM-results of the BSF investigation show that after a LT-AlN interlayer the GaN layer is grown stacking faults free in an area with a total length of ~ 100 μm.
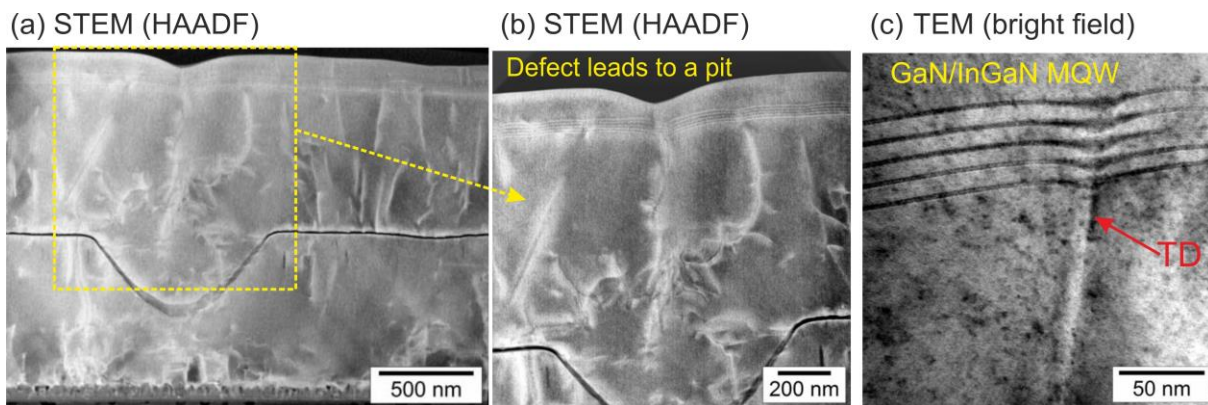
Fig. 5.6: *Cross sectional (a) STEM(HAADF) image, (b) an enlarged image of (a), and (c) TEM (bf) image of GaN/InGaN MQW.*

5.2 Simultaneous growth of LED structures on Si(112) and Si(113)

In order to investigate the impact of the Si orientation on the InGaN MQW properties, the semi-polar LED structures were simultaneously grown on Si(112) (sample L) and Si(113) (sample M), respectively, under optimized growth parameters for a LT-AlN seeding layer

grown on Si(112). The layer structures are shown in Fig. 5.7. Sample L and sample M consist of the following layers: a LT-AlN seeding layer was grown for 2 min (~ 8 nm) at 700 °C and 100 mbar reactor pressure on the Si substrate. The predeposition of around a monolayer of Al prior to the AlN seeding layer growth is helpful for suppressing Si substrate nitridation. An AlGaN layer (~ 60 nm) was grown on top of the seeding layer. Subsequently, GaN layers (~ 1.8 μm) with an AlGaN interlayer (~ 60 nm) were deposited on Si(112). This AlGaN (~ 50 % Al concentration) layer is deposited after about 0.8 μm GaN to reduce the SFs and tensile stress. On top, fivefold GaN/InGaN QWs followed by a GaN:Mg (~ 100 nm) cap layer were grown.

Sample N was grown under growth conditions optimized for Si(113). It consists of nearly the same layer structure as mentioned above except of the following differences: the LT-AlN seeding layer was grown for 3 min (12 nm), a LT-AlN interlayer was inserted after ~ 0.9 μm GaN followed by a GaN layer (~ 1.8 μm), and N_2 was employed as a carrier gas for the second GaN layer which is beneficial for achieving a fully coalesced surface as for this sample (related to my experience). X-ray diffraction measurements, cathodoluminescence and field emission scanning electron microscopy were used for sample characterization. X-ray investigations show nearly $(10\bar{1}6)$ and $(10\bar{1}4)$ oriented GaN films on Si(112) and Si(113) leading to a c-axis inclination angle of ~ 18° and ~ 26° with respect to the surface normal, respectively for samples L and M. For determining the mosaic tilt distribution of the GaN crystallites X-ray ω-scans of nearly symmetric $(10\bar{1}6)$ and $(10\bar{1}4)$ reflections with an ω-FWHM of ~ 0.32° and ~ 0.67° for layers grown on Si(112) and Si(113) were measured for samples L and M, respectively.
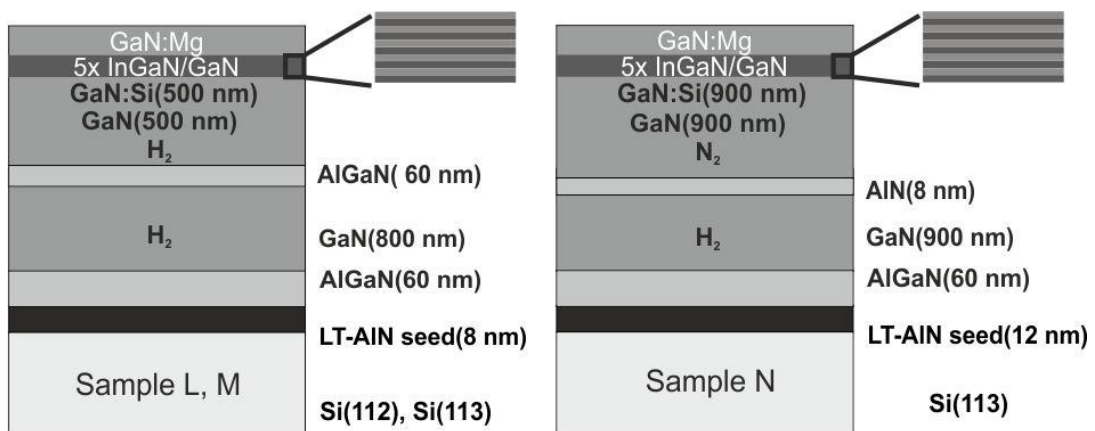
Fig. 5.7: *Layer structures of the samples L, M (left) and N (right) (MD6480, MD6678).*

5.2.1 Surface morphology

Top view FE-SEM images of LED structures on Si(112) and Si(113) are shown in Fig. 5.8. A smooth surface morphology with a few pits is observed for sample L (Fig. 5.8 (a)). In contrast, the surface morphology for the non-optimized LED structures on Si(113) (sample M) shows a rough surface having large V-shaped pits (Fig. 5.8 (b)). Most of the V-shaped pits in Fig. 5.8 (b) are large in diameter and originate below the MQW. They are most likely due to an incomplete coalescence of the buffer layer.
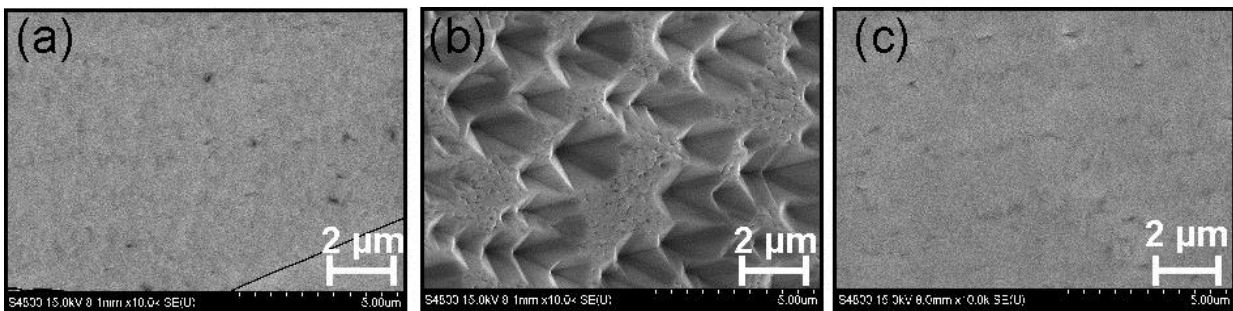
Fig. 5.8: *FE-SEM images: (a) sample L grown on Si(112), (b) sample M grown on Si(113), (c) sample N grown on Si(113).*

5.2.2 Cathodoluminescence measurements

To investigate the optical properties of the samples plan-view low temperature CL measurements were performed at 6 K. The SEM images as well as the corresponding integral spectra and CL wavelength images are presented in Fig. 5.9. For sample L, a relatively homogenous wavelength distribution is observed apart from local spots of strongly varying emission wavelengths in the spectral range from 450 nm to 500 nm (Fig. 5.9 (g)). The differing spotty wavelength distribution in the CL wavelength image is most likely caused by locally varying indium incorporation due to morphological defects such as pits. In comparison, the emission wavelength of sample M shows a distribution in a broader spectral range from 354 nm to 554 nm (Fig. 5.9 (h)). The rough surface having large pits affects the integral CL spectra of sample M showing two dominant InGaN MQW peak emissions (Fig. 5.9 (b)). The QW emission from 380 nm to 420 nm stems from the flat region and the luminescence from 470 nm to 550 nm is emitted from the rough region including the V-shaped pits. For a more complete understanding, monochromatic CL images of these spectral regions have been taken which better visualize the luminescence distribution (Figs. 5.9 (k), (l)). The luminescence of the peaks I and II shows a complementary behavior,

i. e. in areas where peak I comprises an emission with high intensity, the emission from peak II is drastically reduced and vice versa.

5.2.3 Semi-polar LED structure optimized for Si(113)

As shown in CL measurements and FE-SEM images, growth conditions optimized for GaN on Si(112) did not lead to high quality GaN with a smooth surface on Si(113). Therefore the growth parameters had to be optimized for each Si orientation, here for Si(113). As a result GaN $(10\bar{1}5)$ was grown nearly parallel to the Si(113) substrate surface with a c-axis tilt angle of 21°.

Figs. 5.8 (c) and 5.9 (f) show a smooth surface morphology with a few pits on sample N. The CL integral spectrum (Fig. 5.9 (c)) shows one dominant peak at ~ 380 nm, which is shifted about 90 nm towards shorter wavelengths compared to the InGaN peak position of sample L (Fig. 5.9 (a)). In addition, a low-intensity InGaN peak is visible at ~ 430 nm, probably due to a higher In concentration (Fig. 5.9 (c)).

Here, two questions remain open: the first one is if the CL spectrum at ~ 380 nm (related to ~ 3.25 eV) in Fig. 5.9 (c) is due to MQW emission or to defect luminescence. To answer this question, cross sectional CL- and FE-SEM-measurements were performed. Fig. 5.10 presents cross sectional FE-SEM images of samples L, M and N. The positions of the interlayers (AlGaN on sample L, M and LT-AlN on sample N) are highlighted by dashed lines. For the optimized samples L and N, one can see that interlayers are grown nearly parallel to the substrate surface resulting in stacking fault reduction for the second GaN layer. In contrast, it is observed for sample M that an undulated AlGaN interlayer is grown between the GaN layers. As already shown in chapter 4 such a non-planar interlayer is not able to annihilate SFs in the GaN layer. Figs. 5.11 (g), (h) and (i) show cross sectional CL wavelength images of samples L, M and N, respectively. In these images, one can see that the GaN grown after the interlayers is of better quality, evidenced by dominating band edge emission (D^0,X), whereas the first GaN layers (GaN layer below the interlayers) show a dominant defect luminescence. The integral CL intensities of samples L, M and N are shown in Fig. 5.11 (d), (e) and (f), respectively. A dominant InGaN emission is observed from optimized GaN structures in Fig. 5.11 (d) and (f), whereas in Fig. 5.11 (e) one can see the InGaN MQW luminescence as well as luminescence of the other layers. The second question is why there is a variation of the indium concentration in the MQWs. Transmission electron microscopy results of the other samples, which were deposited on Si(112) with nearly the

same structures (Fig. 5.6), show that the QW thickness and their interface sharpness depend on the structural quality of the GaN buffer layers. A smooth GaN buffer layer with a very low defect density results in a high quality MQW with homogenously distributed In in the active area yielding in a narrow luminescence spectrum.
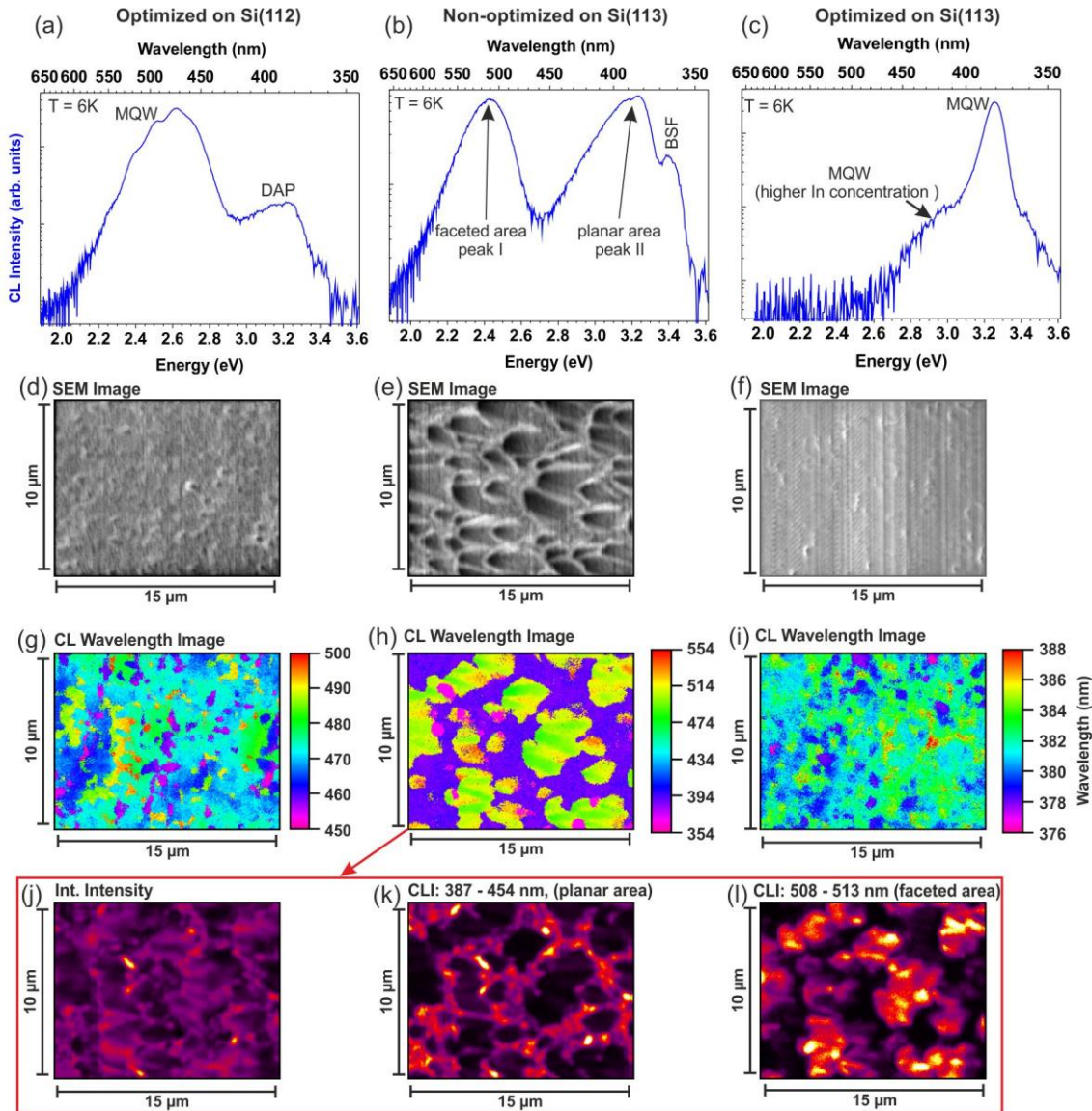
Fig. 5.9: *Integral CL spectra (a,b,c) of the sample areas shown in the SEM images (d,e,f) and corresponding CL peak wavelength images (g,h,i) giving the emission distribution of the InGaN QW for sample L, M and N, respectively. Integral CL intensity image for sample M (j) and CL intensity images of the high energy emission (k) and low energy emission (l).CL intensity images have a logarithmic scale.*
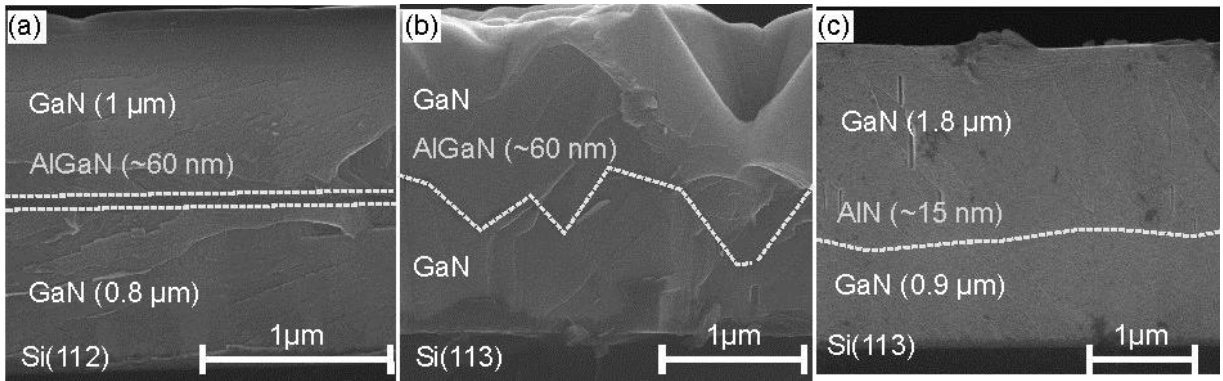
Fig. 5.10: *FE-SEM cross sectional images: (a) sample L, (b) sample M, (c) sample N.*
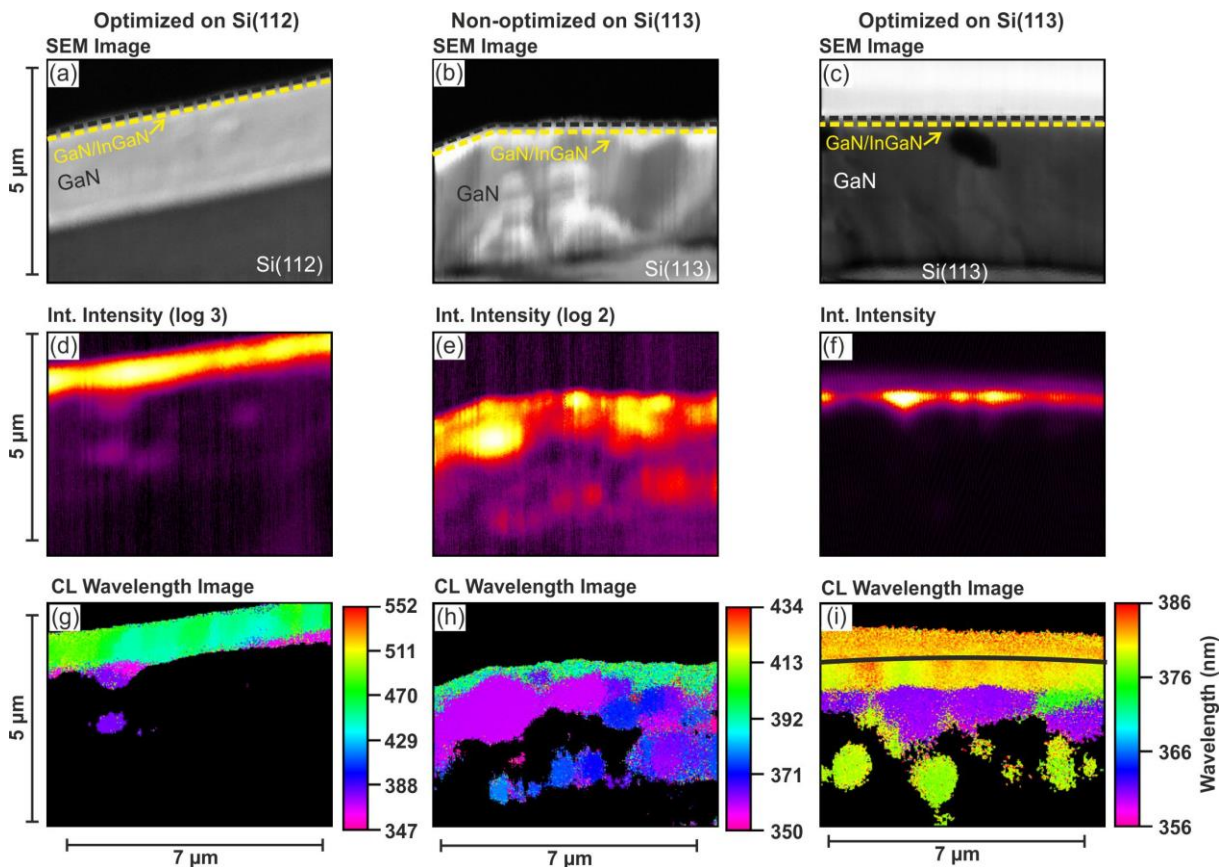
Fig. 5.11: *Cross section SEM images (a,b,c) with corresponding integral CL intensity images (d,e,f) and CL wavelength images of the LED structure (g,h,i) for samples L, , and C, respectively. The border between the sample's edge and surface is marked by a black line in image (i). The surfaces of the samples are marked by black dashed lines and the nominal positions of the active GaN/InGaN layers are highlighted by yellow dashed lines.*

Semi-polar InGaN QWs grown on Si(112) and Si(113) show luminescence at different wavelengths. The position and width of the InGaN peaks are influenced by the MQW-thickness, Indium concentration, electric field and Si orientation. Electron holography and differential phase contrast (DPC) can characterize internal electric fields in QWs. Using these

investigation methods, the internal electric fields in the QWs could be measured with respect to the c-axis tilt angle and Si surface orientations. Unfortunately the samples of semi-polar QWs were grown inhomogeneously regarding to thickness and In concentration and have many cracks. Because of this a precise investigation in terms of a reduction of the electric fields in growth direction is not possible. Semi-polar QWs on high index Si have to be optimized to obtain a crack free surface and a sharp InGaN/GaN interface.

Therefore it is observed that a GaN/InGaN MQW grown under nominally identical growth conditions on different silicon substrate orientations with different GaN buffer layers shows different properties.

6 Summary

In this work a new method for the growth of semi-polar single crystalline GaN layers on non-patterned Si(11h) substrates by metal organic vapor phase epitaxy (MOVPE) is demonstrated.

For this purpose silicon substrates with different surface orientations such as Si(111), Si(112), Si(113), Si(114), Si(115), Si(116), Si(117) and Si(410) were investigated. As a result of this it was observed that the Si surface orientation and AlN seeding layer growth parameters, e.g. temperature, thickness and growth rate have a significant impact on the variety of crystalline orientations of the AlN and with it the GaN grown on top. A high temperature AlN seeding layer (>1000 °C) leads to c-axis oriented GaN growth on all investigated Si surface orientations, whereas a low temperature AlN seeding layer (680 °C) can result in semi-polar GaN layers, except for Si(111) where always c-axis oriented GaN has been achieved.

Semi-polar GaN structures, which were grown and investigated in this work, can be divided into two groups regarding the LT-AlN seeding layer thickness and growth rate and Si surface directions.

The first group was deposited on non-pattered planar substrates with orientations from Si(112) to Si(117) (with a thin ~ 4 nm and a high growth rate LT-AlN seeding layer) optimized for Si(112). Hereby, single component semi-polar growth of GaN layers was demonstrated on Si(112) to Si(116). In comparison, on Si(117) only multi-component GaN structures could be realized. Pole figure measurements of these samples grown on Si(117) showed a higher intensity and a larger GaN inclination angle compared to those grown on a LT-AlN seeding layer with low growth rate. It was found that the c-axis tilt angle depends on the h values and increases from Si(112) to Si(117), e.g. from ~ 18° to ~ 47° respectively.

The second group was grown on Si(112), Si(113) and Si(114) with LT-AlN grown with a low growth rate and varied thickness from ~ 8 nm to ~ 40 nm. For GaN layers grown on Si(112) and Si(113), it was observed that the GaN c-axis inclination angles decrease as the LT-AlN seeding layer thickness increases from ~ 4 nm to ~ 40 nm. GaN layers were deposited as single component GaN on Si(112) and Si(113) applying ~ 4 nm to ~ 40 nm thick LT-AlN seeding layers.

Another result achieved is the elimination of basal plane stacking faults by the insertion of a LT-AlN interlayer in semi-polar GaN layers. This result does not only apply for

layers on Si but to all semipolar heterolayers with an inclination of the c-axis towards the m-plane. In this work, stacking fault elimination was demonstrated for nearly $(10\bar{1}6)$ and $(10\bar{1}5)$ oriented GaN layers grown on Si(112) and Si(113) respectively. The efficient defect elimination was visualized by CL as well as STEM and STEM-CL measurements. Here the I_1-BSF density was reduced from $10^5\,cm^{-1}$ in the lower GaN layer to $2\ x10^4\ cm^{-1}$ in the upper GaN layer.

Finally, semi-polar GaN/InGaN MQW structures were grown on GaN layers on Si(112) and Si(113) substrates. Here a direct comparison between c-axis oriented structures and semi-polar structures was difficult due to the different optimum growth condictions on each surface. Thus a reduction in polarization field strength has not yet been able to be proved by such samples.

Crack elimination of semi-polar GaN layers turned out to be more demanding than for GaN grown on Si(111), mostly because layer schemes can not be simply transferred from growth on Si(111) to Si(11h) due to very different seeding layer conditions and a still inferior material quality. Thus further work is required to optimize growth for high-quality semi-polar GaN based LEDs on planar high index Si substrates. In principle, with low stacking fault densities achievable by LT-AlN interlayers, GaN growth on Si(11h) substrates opens a promising route towards low-cost, polarization reduced light emitters on planar Si substrates.

Bibliography

[AHE]   A. Dadgar, Abteilung Halbleiterepitaxie, Otto-von-Guericke-Universität Magdeburg
http://www.uni-magdeburg.de/ahe

[Amano 1986]   H. Amano, N. Sawaki, I. Akasaki, and Y. Toyoda, *Metalorganic vapor phase epitaxial growth of a high quality GaN film using an AlN bufferlayer*, Appl. Phys. Lett. **48**, 5, 353 (1986).

[Amano 1989]   H. Amano, M. Kito, K. Hiramatsu, and I. Akasaki, *P-type conduction in Mg-doped GaN treated with low-energy electron beam irradiation (LEEBI)*, Jpn. J. Appl. Phys. **28**, no. 12, L2 112 (1989).

[Ambacher 1998] O. Ambacher, review article, *Growth and applications of Group III-nitrides,* J. Phys. D, appl. Phys. **31**, 2653 (1998).

[Ambacher 1999] O. Ambacher, R. Dimitrov, M. Stutzmann, B.E. Foutz, M.J. Murphy, J.R. Shealy, N.G. Weimann, K. Chu, M. Chumbes, B. Green, A.J. Sierakowski, W.J. Schaff und L.F. Eastman, *Role of Spontaneous and Piezoelectric Polarization Induced Effects in Group-III Nitride Based Heterostructures and Devices,* Phys. Stat. Sol. (b) **216**, 381 (1999).

[Avramescu 2009] A. Avramescu, T. Lermer, J. Müller, S. Tautz, D. Queren, S. Lutgen, and U. Strauss, *InGaN laser diodes with 50 mW output power emitting at 515 nm,* Appl. Phys. Lett. **95**, 071103 (2009).

[Baker 2005]   T. J. Baker, B. A. Haskell, F.Wu, P. T. Fini, J. S. Speck, and S. Nakamura, *Characterization of planar semipolar gallium nitride films on spinel substrates*, Jpn. J. Appl. Phys. **44**, no. 28–32, L920 (2005).

[Baker 2006]   T. J. Baker, B. A. Haskell, F. Wu, J. S. Speck, and S. Nakamura, *Characterization of Planar Semipolar Gallium Nitride Films on Sapphire Substrates,* Jpn. J.Appl. Phys. Part 2 **45**, L154 (2006).

[Baski 1997]   A. A. Baski, S.C. Erwin and L. J. Whitman, *the structure of silicon surfaces from (001) to (111),* Surface Science, **392**, issue 1-3, 69 (1997).

[Berghaus 1987]   Th. Berghaus, A. Brodde, H. Neddermeyer and St. Tosch, *Scanning tunneling microscopy on Si(112),* Surf. Sci. 1**84**, 273-288, (1987).

[Bernardini 1997]   F. Bernardini, V. Fiorentini, and D. Vanderbilt, Spontaneous polarization and piezoelectric constants of III-V nitrides, Phys. Rev. B, **56,** R10024 (1997).

[Bernardini 1998]   F. Bernardini and V. Fiorentini, *Macroscopic polarization and band offsets at nitride heterojunctions.* Phys. Rev. B, **57**, R9427 (1998).

[Bertram 1999]   F. Bertram, *Kathodolumineszenz- Mikroskopie an komplexen, lokal selektiven Epitaxie- und lateral überwachsenen GaN-Strukturen,* Dissertation, Otto-von-Guericke-Universität Magdeburg FNW/IEP/AFP (1999).

[Bettels 2011]   Ch. Bettels, *Röntgentexturanalyse an semi- und unpolaren GaN-Schichten, Belegarbeit,* Otto-von-Guericke-Universität Magdeburg FNW/IEP/AFP (2011).

[Bruns 1985]   G. Burns, *Solid State Physics,* Academic Press, New York, pp. 88-92 (1985).

[Chadi 1984]   D. J. Chadi, *Theoretical study of the atomic structure of silicon (211), (311), and (331) surfaces,* Phys. Rev. B **29**, 785 (1984).

[Chakraborty 2004]   A. Chakraborty, B. A. Haskell, S. Keller, J. S. Speck, S. P. DenBaars, S. Nakamura, and U. K. Mishra, *Nonpolar InGaN/GaN emitters on reduced-defect lateral epitaxially overgrown a-plane GaN with drive current-independent electroluminescence emission peak,* Appl. Phys. Lett. **85**, 5143 (2004).

[Chen 2001]   P. Chen, R. Zhang, Z.M. Zhao, D.J. Xi, B. Shen, Z.Z. Chen, Y.G. Zhou, S.Y. Xie, W.F. Lu, and Y.D. Zheng, *Growth of high quality GaN layers with AlN buffer on Si(111) substrates*, J. Cryst. Growth **225**, 150 (2001).

[Chichibu 2003]   S. F. Chichibu, T. Onuma, T. Aoyama, K. Nakajima, P. Ahmet, T. Chikyow, T. Sota, S. P. DenBaars, S. Nakamura, T. Kitamura, Y. Ishida, and H. Okumura, *Recombination dynamics of localized excitons in cubic InxGa1−xN/GaN multiple quantum wells grown by radio frequency molecular beam epitaxy on 3C–SiC substrate*, J. Vac. Sci. Technol. B 21, 1856 (2003).

[Chichibu 2006]	S. F. Chichibu, A. Uedono, T. Onuma, B. A. Haskell, A. Chakraborty, T. Koyama, P. T. Fini, S. Keller, S. P. DenBaars, J. S. Speck, U. K. Mishra, S. Nakamura, S. Yamaguchi, S. Kamiyama, H. Amano, I. Akasaki, J. Han, and T. Sota, *Origin of defect-insensitive emission probability in In-containing (Al, In, Ga) N alloy semiconductors*, Nat. Mater. **5**, no. 10, 810 (2006).
[Chiu 2011]	Chiu C-H, Lin D-W, Lin C-C, Li Z-Y, Chang W-T, Hsu H-W, Kuo H-C, Lu T-C, Wang S-C, Liao W-T, Tanikawa T, Honda Y, Yamaguchi M, and Sawaki N, *Reduction of efficiency droop in semipolar (1101) InGaN/GaN light emitting diodes grown on patterned silicon substrates, Appl. Phys. Express,* **4** 012105 (2011).
[Clames 2006]	J. Y. Clames, Ch. Giesen, T. Meyer, and M. Heuken, *MOCVD of InGaN-based light emitting structures on silicon substrates with strain optimized buffer layers using long Al predeposition*, Phys. Stat. Sol. C **3** (6), 2191 (2006).
[Dabrowski 2000]	J. Dabrowski and H.-J. Müssig, *Silicon Surfaces and Formation of Interfaces*, World Scientific, Singapore, (2000).
[Dadgar 2000a]	A. Dadgar, J. Bläsing, A. Diez, A. Alam, M. Heuken und A. Krost, *Metalorganic Chemical Vapor Phase Epitaxy of Crack-Free GaN on Si(111) Exceeding 1 μm in Thickness* Jpn. J. Appl. Phys. **39**, L1183 (2000).
[Dadgar 2000b]	A. Dadgar, J. Christen, S. Richter, F. Bertram, A. Diez, J. Bläsing, A. Krost, A. Strittmatter, D. Bimberg, A. Alam, and M. Heuken, IPAP Conference Series 1, 845 (2000).
[Dadgar 2002]	A. Dadgar, A Krost, Vacuum Science and technology: Nitrides as seen by the Technology p.196-241 (2002), edited by Tanya Paskova, Bo Monemar (Published by Research Signpost).
[Dadgar 2003]	A. Dadgar, M. Poschenrieder, J. Bläsing, O. Contreras, F. Bertram, T. Riemann, A. Reiher, M. Kunze, I. Daumiller, A. Krtschil, A. Diez, A. Kaluz, A. Modlich, M. Kamp, J. Christen, F.A. Ponce, E. Kohn, and A. Krost, *MOVPE growth of GaN on Si(111) substrates,* J. Cryst. Growth, **248**, 556 (2003).

[Dadgar 2007]   A. Dadgar, F. Schulze, M. Wienecke, A. Gadanecz, J. Bläsing, P. Veit, T. Hempel, A. Diez, J. Christen, and A. Krost, *Epitaxy of GaN on silicon-impact of symmetry and surface reconstruction*, New J. Phys. **9**, 389 (2007).´

[Dadgar 2010].   T. Li, M. Mastro, A. Dadgar, *III–V Compound Semiconductors: Integration with Silicon-Based Microelectronics,* Published by CRC Press (2010).

[Dadgar 2011]   A. Dadgar, R. Ravash, P. Veit, G. Schmidt, M. Müller, A. Dempewolf, F. Bertram, M. Wieneke, J. Christen, and A. Krost, *Eliminating stacking faults in semi-polar GaN by AlN interlayers,* Appl. Phys. Lett. **99**, 021905 (2011).

[Damilano 2008]   B. Damilano, F. Natali, J. Brault, T. Huault, D. Lefebvre, R. Tauk, E. Frayssinet, J. C. Moreno, Y. Cordier, F. Semond, S. Chenot, and J. Massies, *Blue (Ga,In)N/GaN Light Emitting Diodes on Si(110) Substrate*, Appl. Phys. Express, **1**, 121101(2008).

[Degushi 1999]   T. Deguchi, K. Sekiguchi, A. Nakamura, T. Sota, R. Matsuo, S. Chichibu, and S. Nakamura, *Quantum-Confined Stark Effect in an AlGaN/GaN/AlGaN Single Quantum Well Structure,* Jpn. J. Appl. Phys. Part 2 **38**, L914 (1999).

[Drum 1965]   C.M. Drum, *Intersecting faults on basal and prismatic planes in aluminium nitride,* Philosophical Magazine, **11**, 313 (1965).

[Eaglesham 1993]   D. J. Eaglesham, A. E. White, L. C. Feldman, N. Moriya and D. C. Jacobson, *Equilibrium Shape of Si,* Phys. Rev. Lett. **70**, 1643 (1993).

[Feltin 2001]   E. Feltin, S. Dalmasso, P. de Mierry, B. Beaumont, H. Lahrèche, A. Bouillé, H. Haas, M. Leroux and P. Gibart, *Green InGaN Light-Emitting Diodes Grown on Silicon (111) by Metalorganic Vapor Phase Epitaxy*, Jpn. J. Appl. Phys. **40,** L738 (2001).

[Feneberg 2007]   M. Feneberg and K. Thonke, *Polarization fields of III-nitrides grown in different crystal orientations,* J. Phys. Condens. Matter **19**, 403201 (2007).

[Fischer 2009]   A. M. Fischer, Z. Wu, K. Sun, Q.Wei, Y. Huang, R. Senda, D. Iida, M. Iwaya, H. Amano, and F. Ponce, *misfit strain relaxation by*

stacking fault generation in InGaN Quantum Wells grown on m-Plane GaN, Appl. Phys. Express **2**, 041002 (2009).

[Fujioka 2010]   A. Fujioka, T. Misaki, T. Murayama, Y. Narukawa, and T. Mukai, *Improvement in Output Power of 280-nm Deep Ultraviolet Light-Emitting Diode by Using AlGaN Multi Quantum Wells,* Appl. Phys. Express **3,** 041001(2010).

[Fujito 2009a]   K. Fujito, S. Kubo and I. Fujimura, *Development of bulk GaN crystals and nonpolar/semipolar substrates by HVPE MRS Bull,* **34,** 313 (2009).

[Fujito 2009b]   K. Fujito, S. Kubo, H. Nagaoka, T. Mochizuki, H. Namita and S. Nagao, *Bulk GaN crystals grown by HVPE J. Cryst. Growth,* **311,** 3011 (2009).

[Fulk 2006]   C. Fulk, S. Sivananthan, D. Zavitz, R. Singh, M. Trenary, Y. P. Chen, G. Brill, and N. Dhar, *The Structure of the Si (211) Surface*, J. Electronic Materials, **35**, 1449 (2006).

[Funato 2006]   M. Funato, M. Ueda, Y. Kawakami, Y. Narukawa, T. Kosugi, M. Takahashi and T. Mukai, *Blue, Green, and Amber InGaN/GaN Light-Emitting Diodes on Semipolar {11-22} GaN Bulk Substrates,* Japan. J. Appl. Phys. **45**, L659 (2006).

[Gordon 2011]   S.Gordon, *In-situ Kathodolumineszenzspektroskopie an photonischen Halbleiterheterostrukturen im Rastertransmissionselektronenmikroskop, Diplomarbeit,* Otto-von-Guericke-Universität Magdeburg FNW/IEP/AFP (2011).

[Grundmann 1991]   M. Grundmann, A. Krost and D. Bimberg, *Low-temperature metalorganic chemical vapor deposition of InP on Si(001),* Appl. Phys. Lett. **58**, 284 (1991).

[Harrison 1980]   W.A. Harrison, *Electronic structure and properties of solids*, NY. Dover, pp. 174-179 (1980).

[Haskell 2003]   B. A. Haskell, F. Wu, M. D. Craven, S. Matsuda, P. T. Fini, T. Fujii, K. Fujito, S. P. DenBaars, J. S. Speck and S. Nakamur, *Defect reduction in $\left(11\bar{2}0\right)$ a-plane gallium nitride via lateral epitaxial overgrowth by hydride vapor-phase epitaxy,* Appl. Phys. Lett. **83**, 644 (2003).

[Herman 2004]   M.A. Herman, W. Richter, H. Sitter, *Epitaxy: Physical Principles and Technical Implementation*, Spinger-Verlag Berlin Heidelberg (2004).

[Holst 2000]   J. Holst, A. Hoffmann1, D. Rudloff, F. Bertram, T. Riemann, J. Christen, T. Frey, D. J. As, D. Schikora, and K. Lischka, *The origin of optical gain in cubic InGaN grown by molecular beam epitaxy*. Appl. Phys. Lett. **76**, 2832 (2000).

[Hong 2011]   J. Hong, Y. Chang, Y. Ding, Z. L. Wang, R. L. Snyder, *growth of GaN films with controlled out-of-plane texture on Si wafers,* thin solid films, **519**, 3608 (2011).

[Horino 1996]   K. Horino, A. Kuramata, K. Domen, R. Soejima, and T. Tanahashi, *Growth of $(1\bar{1}00)$ oriented GaN on $(1\bar{1}00)$ 6H-SiC by metalorganic vapor phase epitaxy,* presented at the Int. Symp. Blue Laser Light Emitting Diodes, Chiba, Japan, We-P32 (1996).

[Hull 1984]   D. Hull and D.J. Bacon, *Introduction to Dislocation*, Pergamon Press, Oxford (1984).

[Imer 2006]   B. Imer, F. Wu, S. P. DenBaars, and J. S. Speck, *Improved quality (11 20) a-plane GaN with sidewall lateral epitaxial overgrowth,* Appl. Phys. Lett. **88,** 061908 (2006).

[Ishikawa 2008]   H. Ishikawa, K. Shimanaka, F. Tokura, Y. Hayashi, Y. Hara, and M. Nakanishi, *MOCVD growth of GaN on porous silicon substrates,* J. of Cryst. Growth, **310**, 4900 (2008).

[Itano 1993]   M. Itano, F. Kern, M. Miyashita and T. Ohmi, *Particle Removal from Silicon Wafer Surface in Wet Cleaning Process*, IEEE Transactions on Semicond. Manufact. **6**, 258 (1993).

[Ivchenko 2005]   E. L. Ivchenko, *Optical Spectroscopy of Semiconductor Nanostructures*, Alpha Science International, Ltd, Harrow, UK, (2005).

[Johnston 2009]   C. F. Johnston, M. J. Kappers, M. A. Moram, J. L. Hollander and C. J. Humphreys, *Assessment of defect reduction methods for nonpolar a-plane GaN grown on r-plane sapphire* J. Cryst. Growth, **311**, 3295–9 (2009).

[Kaplan 1982]   R. Kaplan, Surface Science, *LEED investigation of the Si (112) surface structure,* **116**, 104 (1982).

[Khan 1991] M. Asif Khan, J.M. Van Hove, J.N. Kuznia, and D.T. Olson, *High Electron Mobility GaN/Al$_x$Ga$_{1-x}$N Heterostructures grown by LPMOCVD,* Appl. Phys. Lett. **58**, 2408 (1991).

[Klug 1974] H. P. Klug and L. E. Alexander, X-*ray diffraction procedures for polycrystallineand amorphous materials*, Wiley, New York, (1974).

[Krost 1996] A. Krost, G. Bauer, and J. Woitok, *High resolution x-ray diffraction in Optical characterization of epitaxial semiconductor layers,* Springer-Verlag, Berlin, Heidelberg (1996).

[Krost 2002] A. Krost and A. Dadgar, *GaN-Based Devices on Si,* phys. stat. sol. (a) **194**, 361 (2002).

[Kwon 2002] M. K. Kwon, Y. H. Jeong, E. H. Shin, J. W. Yang, K. Y. Lim, J. I. Roh and K. S. Nahm, *Effect of an Al Pre-seeded AlN Buffer on GaN Films Grown on Si(111) Substrates by Using SiC Intermediate Layers*, J. Korean Physical Society **41** (6), 880 (2002).

[Langer 1999] R. Langer, J. Simon, V. Ortiz, N. T. Pelekanos, A. Barski, R. Andre, and M. Godlewski, *Giant electric fields in unstrained GaN single quantum wells*, Appl. Phys. Lett. **74**, 3827 (1999).

[Lefebvre 2001] P. Lefebvre, A. Morel, M. Gallart, T. Taliercio, J. All`egre, B. Gil, H. Mathieu, B. Damilano, N. Grandjean, and J. Massies, *High internal electric field in a graded-width InGaN/GaN quantum well: Accurate determination by time-resolved photoluminescence spectroscopy,* Appl. Phys. Lett. **78**, 1252 (2001).

[Levinshtein 2001] M. Levinshtein, S. Rumyantsev, M. Shur, *Properties of advanced Semiconductor Materials,* Wiley-IEEE, New York, Chap. **2**, 31 (2001).

[Li 2013] Hongjian Li, Panpan Li, Junjie Kang, Zhi Li, Yiyun Zhang, Zhicong Li, Jing Li, Xiaoyan Yi, Jinmin Li and Guohong Wang, *Quantum Efficiency Enhancement of 530 nm InGaN Green Light-Emitting Diodes with Shallow Quantum Well*, Appl. Phys. Express **6**, 052102 (2013).

[Liu 2005]   R. Liu, A. Bell, F. A. Ponce, C. Q. Chen, J. W. Yang, and M. A. Khan, *Luminescence from stacking faults in gallium nitride*, Appl. Phys. Lett. **86**, 021908 (2005).

[Lin 2010]   J. Lin, H. Jiang, and N. Sawaki, *New technology approaches in III–V compound semiconductor: integration with silicon-based microelectronics, edited by* T. Li, M. Mastro, and A. Dadgar (CRC Press, Boca Raton, FL, 2010).

[Markurt 2012]   T. Markurt, Private communication (2012).

[Masui 2005]   H. Masui, A. Chakraborty, B. A. Haskell, U. K. Mishra, J. S. Speck, S. Nakamura, and S. P. Den Baars, *Polarized Light Emission from Nonpolar InGaN Light-Emitting Diodes Grown on a Bulk m-Plane GaN Substrate, Japan*. J. Appl. Phys. **44**, L1329 (2005).

[Matthews 1970] J. W. Matthews, S. Mader, and T. B. Light, *Accommodation of Misfit Across the Interface Between Crystals of Semiconducting Elements or Compounds*, J Appl. Phys. **41**, 3800 (1970).

[Matthews 1974] J. W. Matthews and A. E. Blakeslee, J. Cryst. Growth, **27**, 118 (1974).

[Miller 1984]   D. A. Miller, D. S. Chemla, T. C. Damen, A. C. Gossard, W. Wiegmann, T. H. Wood and C. A. Burrus, *Band-edge electroabsorption in quantum well structures: The quantum-confined Stark effect,* Phys. Rev. Lett. **53**, 2173 (1984).

[Miyoshi 2009]   T. Miyoshi, S. Masui, T. Okada, T. Yanamoto, T. Kozaki, S. I. Nagahama and T. Mukai, *510–515 nm InGaN-based green laser diodes on c-plane GaN substrate*, Appl. Phys. Express **2**, 062201 (2009).

[Morkoc 2005]   Michael A. Reshchikova and Hadis Morkoc, *Luminescence properties of defects in GaN*, J. Appl. Phys. **97**, 061301 (2005).

[Morkoc 2008]   H. Morkoc, *Handbook of nitrides semiconductors and devices volume 1: materials properties, physics and growth*, Wiley-VCH Verlag, Weinheim (2008).

[Moram 2009]   M. A. Moram, C. F. Johnston, J. L. Hollander, M. J. Kappers and C. J. Humphreys, *Understanding x-ray diffraction of nonpolar gallium nitride films,* J. Appl. Phys. **105,** 113501(2009).

[Müller 2006]   A. Müller, D. Neculoiu, D. Vasilache, D. Dascalu, G. Konstantinidis, A. Kosopoulos, A. Adikimenakis, A. Georgakilas, K. Mutamba, C. Sydlo, H.L. Hartnagel, A. Dadgar, *GaN micromachined FBAR structures for microwave applications,"* *Superlattices and Microstructures,* **40**, no. 4-6, 426 (2006).

[Müller 2010]   M. Müller, Belegarbeit, *Otto-von-Guericke-Universität Magdeburg FNW/IEP/AHE* (2010).

[Nakamura 1992]   S. Nakamura and T. Mukai, *High-quality InGaN films grown on GaN films*, Japan. J. Appl. Phys. **31**, no. 10B, L1 457 (1992).

[Nakamura 1994]   S. Nakamura, *Growth of InGaN compound semiconductors and high-power InGaN/AlGaN heterostructure violet-light-emitting diodes*, Microelectron J. **25**, no. 8, 651 (1994).

[Nakamura 1995a]   S. Nakamura, M. Senoh, N. Iwasa, and S. Nagahama, *High brightness InGaN blue, green and yellow light-emitting diodes with quantum well structures*, Jpn. J. Appl. Phys. **34**, no. 7A, L797 (1995).

[Nakamura 1995b]   S. Nakamura, M. Senoh, N. Iwasa, S. Nagahama, T. Yamada, and T. Mukai, *Superbright green InGaN single-quantum-well-structure light-emitting diodes*, Jpn. J. Appl. Phys. **34**, no. 10B, L1332 (1995).

[Nakamura 2000]   S. Nakamura, S. Pearton, and G. Fasol, *The Blue Laser Diode: The Complete Story, 2nd ed.,* Berlin, Germany, Springer-Verlag, Chap. **9** (2000).

[Narukawa 2010]   Y. Narukawa, M. Ichikawa, D. Sanga, M. Sano and T. Mukai, *White light emitting diodes with super-high luminous efficacy*, *J. Phys. D, Appl. Phys.* **43,** 354002 (2010).

[Neudeck 2002]   P. G. Neudeck, R. S. Okojie, and L. Y. Chen, H*igh-Temperature Electronics-A Role for Wide Band gap Semiconductors?*, Proceeding of the IEEE, **90**, 6 (2002).

[Ng 2002]	H. M. Ng, *Molecular-beam epitaxy of GaN/AlxGa1−xN multiple quantum wells on R-plane (10math2) sapphire substrates,* Appl. Phys. Lett. **80**, 4369 (2002).
[Ni 2009]	X. Ni, M. Wu, J. Lee, X. Li, A. A. Baski, Ü. Özgür, and H. Morkoç, *Nonpolar m-plane GaN on patterned Si(112) substrates by metalorganic chemical vapor deposition,* Appl. Phys. Lett. **95**, 111102 (2009).
[Nikkei1993]	Nikkei Sangyo Shimbun, Nov. **30**, (in Japanese) (1993).
[Nye 1985]	J. E. Nye, Physical properties of crystals, Oxford University Press, New York, (1985).
[Omara 1990]	W.C. O'Mara, R. B. Herring, and L. P. Hunt, *Handbook semiconductor silicon technology*, Noyes Publications, New Jersey (1990).
[Onumal 2005]	T. Onuma1, A. Chakraborty, B. A. Haskell, S. Keller, S. P. DenBaars, J. S. Speck, S. Nakamura, U. K. Mishra, T. Sota, and S. F. Chichibu, *Localized exciton dynamics in nonpolar (11.hivin.20) InxGa1-xN multiple quantum wells grown on GaN templates prepared by lateral epitaxial overgrowth,* Appl. Phys. Lett. **86**, 151918 (2005).
[Paskova 2008]	T. Paskova, *Nitrides with Nonpolar Surfaces: Growth, Properties and Devices,* Weinheim: Wiley-VCH (2008).
[Patent Nr. 10 2009 042 349]	R. Ravash, A. Dadgar, A. Krost, Semipolar wurtzitische Gruppe-III-Nitrid basierte Halbleiterschichten und darauf basierende Halbleiterbauelemente (2009).
[Patent Nr. 10 2011 011 043.7]	A. Dadgar, A. Krost, P. Veit, R. Ravash, Halbleiterschicht oder Halbleiterschichtsystem mit einer semipolaren oder m-planaren Gruppe-III-Nitrid Schicht (2011).
[Pearton 1999]	S. J. Pearton, J. C. Zolper, R. J. Shul, and F. Ren, *GaN: Processing, defects, and devices*, J. Appl. Phys. **86**, no.1, 1 (1999).
[People 1985]	R. People, and J. C. Bean, *Calculation of critical layer thickness versus lattice mismatch for $Ge_xSi_{1−x}$/Si strained layer heterostructures* Appl. Phys. Lett. **47**, 322 (1985).

[Pierret 1987]   R. F. Pierret, *Advanced Semiconductor Fundamentals. Reading*, MA: Addison-Wesley, **6**, Ch. 4, 91 (1987).

[Porowski 1996]   S. Porowski, *High pressure growth of GaN-new propects for blue lasers,* J. of Cryst. Growth **166**, 583 (1996).

[Porowski 1997]   S. Porowski, *Growth and properties of single crystalline GaN substrates and homoepitaxial layers*, Mater. Sci. Eng., B, **44**, 407 (1997).

[Rajan 2004]   S. Rajan, H. Xing, S. DenBaars, and U. K. Mishra, *AlGaN/GaN polarization-doped field-effect transistor for microwave power applications,* Appl. Phys. Lett. **84**, 1591 (2004).

[Ravash 2011]   R. Ravash, Juergen Blaesing, Thomas Hempel, Martin Noltemeyer, Armin Dadgar, Juergen Christen, and Alois Krost, *Impact of AlN seeding layer growth rate in MOVPE growth of semi-polar gallium nitride structures on high index silicon,* Phys. Stat. Sol. B **248**, 594 (2011).

[Ravash 2012]   R. Ravash, P. Veit, M. Müller, G. Schmidt, A. Dempewolf, T. Hempel, J. Bläsing, F. Bertram, A. Dadgar, J. Christen, and A. Krost, *Growth and stacking fault reduction in semi-polar GaN films on planar Si(112) and Si(113),* Phys. Stat. Sol. C 9, No. 3–4, 507 (2012).

[Reiher 2008]   F. Reiher, *Wachstum Galliumnitrid-basierten Bauelementen auf Silizium (100)–Substraten mittels metallorganischer Gasphasenepitaxie*, Dissertation, Otto-von-Guericke-Universität Magdeburg FNW/IEP/AHE (2008).

[Reiher 2009]   F. Reiher, A. Dadgar, J. Bläsing, M. Wieneke, M. Müller, A. Franke, L. Reißmann, J. Christen, and A. Krost, *InGaN/GaN light-emitting diodes on Si(110) substrates grown by metalorganic vapour phase epitaxy*, Journal of Physics D: Applied Physics **42**, 055107 (2009).

[Reiher 2010]   F. Reiher, A. Dadgar, J. Bläsing, M. Wieneke and A. Krost, *Metalorganic vapor-phase epitaxy of GaN layers on Si substrates*

with Si(110) and other high-index surfaces J. of Cryst. Growth. **312**, 180 (2010).

[Romano 1997]   L. T. Romano, B. S. Krusor and R. J. Molnar, *Structure of GaN films grown by hydride vapor phase epitaxy*, Appl. Phys. Lett. 71, 2283 (1997).

[Romanov 2006]   A. E. Romanov, T. J. Baker, S. Nakamura, and J. S. Speck, *Strain-induced polarization in wurtzite III-nitride semipolar layers,* J. Appl. Phys. **100**, 023522 (2006).

[Round 1907]   H. J. Round, *A note on carborundum,* Electron World, **19**, 309 (1907).

[Sawaki 2009]   N. Sawaki, T. Hikosaka, N. Koide, S. Tanaka, Y. Honda, and M. Yamaguchi, *Growth and properties of semi-polar GaN on a patterned silicon substrat*e, J. of Cryst. Growth, **311**, 2867 (2009).

[Sawaki 2010]   N. Sawaki, Y. Honda, Science China, Technolcal Sciences, **54**, 38–41, DOI: 10.1007/s 11431-010-4182-2 (2010).

[Schulze 04]   F. Schulze, J. Bläsing, A. Dadgar, and A. Krost, *Influence of buffer layers on MOVPE grown GaN on Si(001),* Appl. Phys. Lett. **84**, 4747 (2004).

[Schulze 2006]   F. Schulze, A. Dadgar, J. Bläsing, T. Hempel, A. Diez, J. Christen, and A. Krost, *Growth of single-domain GaN layers on Si(0 0 1) by metalorganic vapor-phase epitaxy,* J. of Cryst. Growth **289**, 485 (2006).

[Schmidt 2011]   G. Schmidt, *In-situ Kathodolumineszenzspektroskopie an photonischen Halbleiterheterostrukturen im Rastertransmissionselektronenmikroskop*, Diplomarbeit, Otto-von-Guericke-Universität Magdeburg FNW/IEP/AFP (2011).

[Scholz 2012]   F. Scholz, *Semipolar GaN grown on foreign substrates: a review,* Semicond. Sci. Technol. **27**, 024002 (2012).

[Speck 2009]   J. S. Speck J S and S. F. Chichibu, *Nonpolar and semipolar group III nitride based materials*, MRS Bull, **34,** 304 (2009).

[Spieß 2005]   L. Spieß, R. Schwarzer, H. Behnken, G. Teichert, Moderne Röntgenbeugung, B. G. Teubner Verlag, Wiesbaden (2005).

[Stampfl 1998]   C. Stampfl and Chris G. Van de Walle, *Energetics and electronic structure of stacking faults in AlN, GaN, and InN*, Phys. Rev. B **57**, R15052 (1998).

[Steven 1982]   Steven L. Wright, Masanori Inada, and Herbert Kroemer, J. Vac. Sci. Technol. **21**, 534 (1982).

[Strauss 2011]   U. Strauss, A. Avramescu, T. Lermer, D. Queren, A. Gomez Iglesias, C. Eichler, J. Müller, G. Brüderl, and S. Lutgen, *Pros and cons of green InGaN laser on c-plane GaN,* Phys. Status Sol. b, **248**, 652 (2011).

[Stringfellow 1989]   G. B. Stringfellow, *Organometallic Vapor-Phase Epitaxy: theory and practice,* 2nd edition, Academic Press, San Diego, California (1989).

[Sunkara 2001]   M.K. Sunkara, S. Sharma, R. Miranda, G. Lian, and E. C. Dickey*, Bulk synthesis of silicon nanowires using a low-temperature vapor–liquid–solid method***,** Appl. Phys. Lett. **79**, 1546 (2001).

[Sze 1981]   S. M. Sze, Physics of Semiconductor Devices, 2nd ed. New York: Wiley, (1981).

[Takeuchi 1997]   T. Takeuchi, S. Sota, M. Katsuragawa, M. Komori, H. Takeuchi, H. Amano and I. Akasaki, *Quantum-confined Stark effect due to piezoelectric fields in GaInN strained quantum wells.* Jpn J. Appl. Phys. 2, **36**, L382–L385 (1997).

[Tanikawa 2008]   T. Tanikawa, T. Hikosaka, Y. Honda, M. Yamaguchi and N. Sawaki, *Growth of semi-polar (11-22)GaN on a (113)Si substrate by selective MOVPE,* Phys. Status Solidi (c) **5**, no. 9, 2966 (2008).

[Tanner 2004]   B. K. Tanner, T. P. A. Hase, T. A. Lafford and M. S. Goorsky, grazing incidence in-plane X-ray diffraction in the laboratory*,* International Centre for Diffraction Data 2004, Advances in X-ray Analysis, **47** (2004).

[Ueda 1985]   K. Ueda and M. Inoue, Surf. Sci., *a study of surface defect of Si(511) by REEED and LEED,* **161**, L578 (1985).

[Van der Merwe 1963] J. H. van der Merwe, *Crystal Interfaces. Part I. SemiInfinite Crystals,* J. Appl. Phys. **34**, 117 (1963).

[Wang 2001] K. Wang and R. Reeber, *Thermal expansion and elastic properties of InN* Appl. Phys. Lett.**79**, 1602 (2001).

[Wieneke 2009] M. Wieneke, *MOVPE Wachstum und strukturelle Eigenschaften von polarisationsreduzierten GaN Schichten, Diplomarbeit, Otto-von-Guericke-Universität Magdeburg FNW/IEP/AHE* (2008).

[Wieneke 2009] M. Wieneke, J. Bläsing, A. Dadgar, P. Veit, S. Metzner, F. Bertram, J. Christen, and A. Krost, *Micro-structural anisotropy of a-plane GaN analyzed by high resolution X-ray diffraction,* Phys. Status Solidi C **6**, S498 (2009).

[Waltereit 2000] P. Waltereit, O. Brandt, A. Trampert, H. T. Grahn, J. Menniger, M. Ramsteiner, M. Reiche, and K. H. Ploog, *Nitride semiconductors free of electrostatic fields for efficient white light-emitting diodes,* Nature, **406**, no. 6798, 865 (2000).

[Wright 1982] S. L. Wright, M. Inada, and H. Kroemer, *Polar‑on‑nonpolar epitaxy: Sublattice ordering in the nucleation and growth of GaP on Si(211) surfaces,* J. Vac. Sci. Technol. **21**, 534 (1982).

[Wu 1996] X. H. Wu, L. M. Brown, D. Kapolnek, S. Keller, B. Keller, S. P. Den Baars and J. S. Speck, *Defect structure of metal organic chemical vapor deposition‑grown epitaxial (0001) GaN/Al2O3,* J. Appl. Phys. **80**, 3228 (1996).

[Wu 2011] Z. H. Wu, T. Tanikawa, T. Murase, Y.-Y. Fang, C. Q. Chen, Y. Honda, M. Yamaguchi, H. Amano, and N. Sawaki, *partial strain relaxation by stacking fault generation in InGaN multiple quantum wells grown on* $(1\bar{1}01)$*semi-polar GaN*, Appl. Phys. Lett**. 98**, 051902 (2011).

[Wunderer 2011] T. Wunderer, M. Feneberg, F. Lipski, J. Wang, R. A. R. Leute, S. Schwaiger, K. Thonke, A. Chuvilin, U. Kaiser, S. Metzner, F. Bertram, J. Christen, G. J. Beirne, M. Jetter, P. Michler, L. Schade, C. Vierheilig, U. T. Schwarz, A. D. Dräger, A. Hangleiter, and F.

Scholz, *Three-dimensional GaN for semipolar light emitters,* Phys. Status Solidi b, **248,** 549 (2011).

[Yang 2009]   M. Yang, H. S. Ahn, T. Tanikawa, Y. Honda, M. Yamaguchi, and N. Sawaki, *Maskless selective growth of semi-polar (1 1-2 2)GaN on Si (3 1 1) substrate by metal organic vapor phase epitaxy,* J. of Cryst. Growth, **311**, 2914 (2009).

[Yoshizumi 2009]   Y. Yoshizumi, M. Adachi, Y. Enya, T. Kyono, S. Tokuyama, T. Sumitomo, K. Akita, T. Ikegami, M. Ueno, K. Katayama, and T. Nakamura , *Continuous-wave operation of 520 nm green InGaN-based laser diodes on semi-polar {20-21} GaN substrates*, Appl. Phys. Express **2,** 092101 (2009).

[Zakharov 2005]   D. N. Zakharov and Z. Liliental-Weber, B. Wagner, Z. J. Reitmeier, E. A. Preble, and R. F. Davis, *Structural TEM study of nonpolar a-plane gallium nitride grown on (11-20) 4H-SiC by organometallic vapor phase epitaxy*, Phys. Rev. B **71,** 235334 (2005).

[Zhang 2007]   B. Zhang, H. Liang, Y. Wang, Z. Feng, K. W. Ng, K. M. Lau, *High-performance IIInitride blue LEDs grown and fabricated on patterned Si substrates*, J. of Cryst. Growth, **298**, 725 (2007).

[Zoroddu 2001]   A. Zoroddu, F. Bernardini, P. Ruggerone and V. Fiorentini, *First-principles prediction of structure, energetics, formation enthalpy, elastic constants, polarization, and piezoelectric constants of AlN, GaN, and InN: Comparison of local and gradient-corrected density-functional theory,* Phys. Rev. B **64**, 045208 (2001).

Appendix

TEM images of the GaN structures grown on Si(117)

The cross sectional TEM-images of sample (MD5170) grown on Si(117) with the LT-AlN seeding layer nominal thickness of 80 nm (20 min) are shown in Fig. 1. At the Si/AlN interface, nominally 2 nm thick AlN shows a high amount of misoriented or amorphous structure consisting of very small crystallites a few nanometers long. After that, AlN consists of polycrystalline structures, where by ~ 20 nm of them form a compact system. With AlN structures increasing in size, a porous system can be made. The vacant spaces were marked with circles. As shown in Fig.2, in Si/AlN interface we observed hollow spaces, which were placed nearly 60 nm from each another and were ~ 18 nm in diameter with a depth of ~ 10 nm. Their origin is not yet clear but it could be related to melt-back etching [Takemoto 2006]. As shown in Fig. 2, the threefold HT-GaN / LT-AlN interlayer (the bright lines show an AlN layer) was not grown evenly and consistently. It was observed on top of the LT-AlN seeding layer with a few nanometers as a total structure, in comparison to the area with ~ 500 nm HT-GaN / LT-AlN interlayers. TEM images showed the size of the GaN structures was heavily dependent on their growth direction and they varied from a few nanometers to several micrometers and there were observed hollows between GaN crystallites.
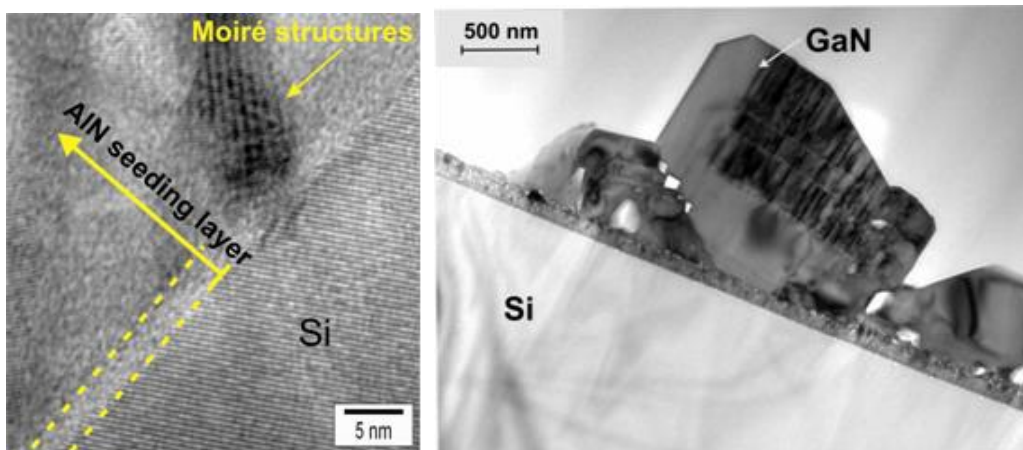
Fig. 1: *Cross sectional High-resolution transmission electron microscopy (HRTEM) image of LT-AlN SL (on the left side), whereas ~ 2 nm of Si/AlN interlayer region consists a high amount of amorphous AlN followed by a polycrystalline region with Moiré-structures (overlapping several crystallites), (on the right side) GaN structures with several hollows between them were observed. This image demonstrates that there are different growth rates according to the crystallite orientation.*
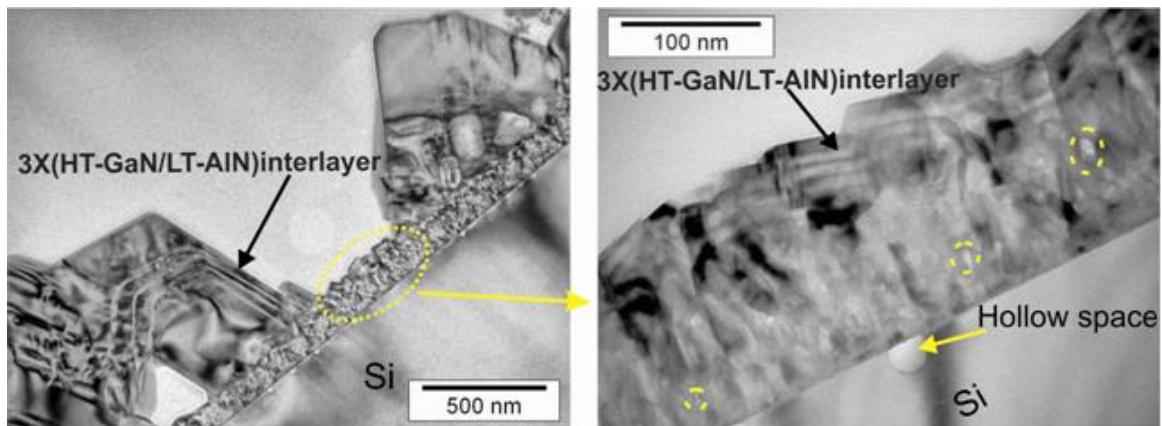
Fig. 2: *Cross-sectional TEM images, (left) an image of total structure consists of the seeding layer, a threefold (HT-GaN / LT–AlN) interlayer and a GaN main layer above them, whereas the size of the GaN structures is heavily dependent of GaN crystallite growth direction. The three dimensional growth of GaN crystallites was observed and a region with very fine GaN crystallites is magnified in the right image.*

The wurtzite (hexagonal crystal) structure

Fig 3: $\vec{b}$ *is a Burgers-vector.*

Normalized intensity of Bragg Brentano measurements

Fig 4: *Intensity is normalized to the total measured intensity and the theoretical intensity of the powder-sample.*

Table 1: *Growth parameters*

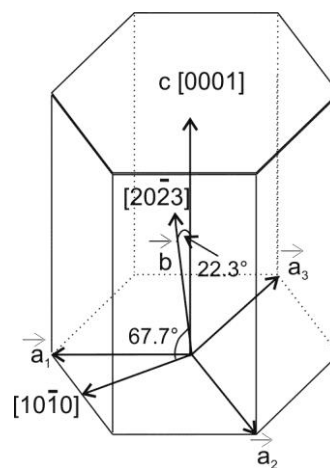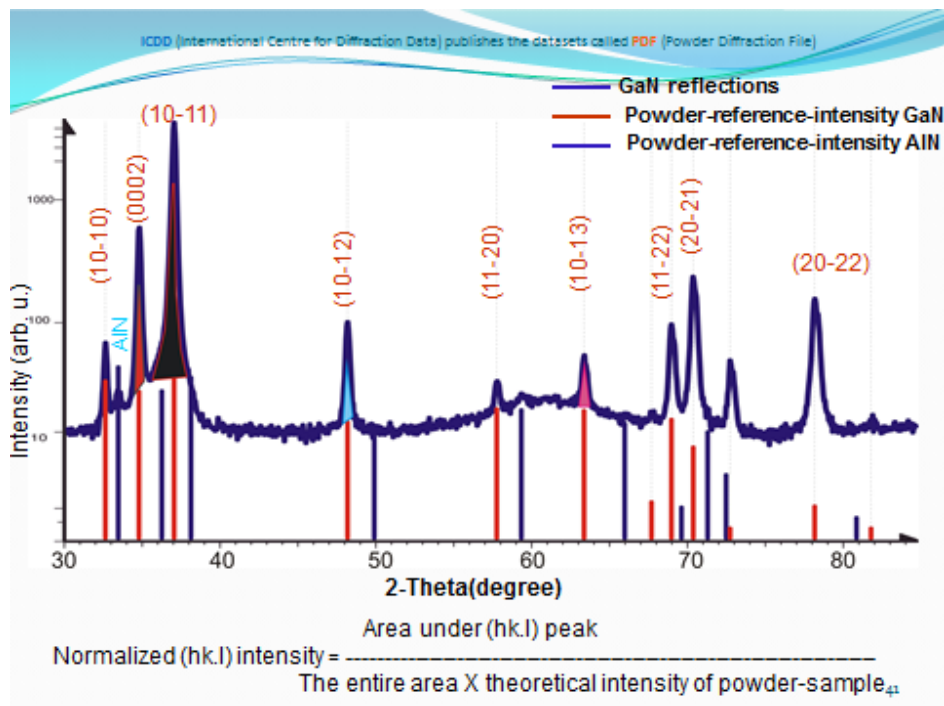| Series α on Si(117) Series β on Si(410)	Seeding layer	Next layer	GaN layer
MD5151, Si (117) MD5151, Si (410)	2min (8 nm), 680°, $p_{(reactor)}$=100mbar, TMAl-flow = 20 sccm	3x(HT-GaN/LT-AlN)	600 nm, $p_{(reactor)}$=200mbar,1145°
MD5154, Si (117) MD5149, Si (410)	4min (16 nm), 680°, $p_{(reactor)}$=100mbar, TMAl-flow = 20 sccm	3x(HT-GaN/LT-AlN)	600 nm $p_{(reactor)}$=200mbar,1145°
MD5155, Si (117) MD5153, Si (410)	6min (24 nm), 680°, $p_{(reactor)}$=100mbar, TMAl-flow = 20 sccm	3x(HT-GaN/LT-AlN)	600 nm $p_{(reactor)}$=200mbar,1145°
MD5159, Si (117)	8min (32 nm) ,680°, $p_{(reactor)}$=100mbar, TMAl-flow = 20 sccm	3x(HT-GaN/LT-AlN)	600nm $p_{(reactor)}$=200mbar,1145°
MD5161, Si (117)	10min (40 nm), 680°, $p_{(reactor)}$=100mbar, TMAl-flow = 20 sccm	3x(HT-GaN/LT-AlN)	600 nm $p_{(reactor)}$=200mbar,1145°
MD5165, Si (117)	12min (48 nm), 680°, $p_{(reactor)}$=100mbar, TMAl-flow = 20 sccm	3x(HT-GaN/LT-AlN)	600 nm $p_{(reactor)}$=200mbar,1145°
MD5169, Si (117) MD5169, Si (410)	16min (64 nm), 680°, $p_{(reactor)}$=100mbar, TMAl-flow = 20 sccm	3x(HT-GaN/LT-AlN)	600 nm $p_{(reactor)}$=200mbar,1145°
MD5172, Si (117)	26min (104 nm), 680°, $p_{(reactor)}$=100mbar, TMAl-flow = 20 sccm	3x(HT-GaN/LT-AlN)	600 nm $p_{(reactor)}$=200mbar,1145°

Table 2: *Growth parameters*

Series	Seeding layer	Next layer	GaN layer
Series χ :MD5166, on Si(117), Si(100)+ 4.5 off and Si(410)	10min (40 nm), 680°, $p_{(reactor)}$=100mbar, TMAl-flow = 20 sccm		
Series δ:MD5167, on Si(117), Si(100) and Si(100)+ 4.5 off	10min (40 nm), 680°, $p_{(reactor)}$=100mbar, TMAl-flow = 20 sccm	3x(HT-GaN/LT-AlN) 160 nm/~ 8 nm) $T_{(GaN)}$=1120°C, $T_{(AlN)}$=630 °C	
Series ε: MD5161, on Si(117) and Si(100)+ 4.5 off	10min (40 nm), 680°, $p_{(reactor)}$=100mbar, TMAl-flow = 20 sccm	3x(HT-GaN/LT-AlN) 160 nm/~ 8 nm) $T_{(GaN)}$=1120°C, $T_{(AlN)}$=630 °C	600 nm $p_{(reactor)}$=200mbar,1145°
Series φ: MD5188, On Si(115) and Si(117)	20min (120 nm), 680°, $p_{(reactor)}$=100mbar, TMAl-flow = 80 sccm	3x(HT-GaN/LT-AlN) 160 nm/~ 8 nm) $T_{(GaN)}$=1120°C, $T_{(AlN)}$=630 °C	600 nm $p_{(reactor)}$=200mbar,1145°
Series γ: MD5179, On Si(112)	16min (110 nm), 680°, $p_{(reactor)}$=100mbar, TMAl-flow = 80 sccm	3x(HT-GaN/LT-AlN) 160 nm/~ 8 nm) $T_{(GaN)}$=1120°C, $T_{(AlN)}$=630 °C	600 nm $p_{(reactor)}$=200mbar,1145°
Series η: MD5460, On Si(112) (sample E) and Si(117)	15s (4 nm), 680°, $p_{(reactor)}$=100mbar, TMAl-flow = 80 sccm	3x(HT-GaN/LT-AlN) 160 nm/~ 8 nm) $T_{(GaN)}$=1120°C, $T_{(AlN)}$=630 °C	600 nm $p_{(reactor)}$=200mbar,1145°
MD5637 (sample G) on Si(112)	T=720 °C, $p_{(reactor)}$=100 mbar TMAl-p=1000 mbar TMAl-flow =80 sccm, d=~ 4 nm, t=15 s	HT-GaN / LT-AlN (~ 160 nm/~ 8 nm) $T_{(GaN)}$=1120°C $T_{(AlN)}$=630 °C	T=1145 °C d=~ 1. 6 µm t=45 min $p_{(reactor)}$=200 mbar

Table 3: *Growth parameters*

Samples	AlN seeding layer	Next layer	GaN layer
Group I on Si(112), Si(117) MD5460	T=720 °C, TMAl-*p=1000 mbar* TMAl-flow =*80 sccm,* *d=~ 4 nm, t=15 s,* *p(reactor)=100 mbar*	HT-GaN / LT-AlN (~ 160 nm/~ 8 nm) $T_{(GaN)}$=1120°C, $T_{(AlN)}$=630 °C	T=1145 °C, d=~600 nm, t=15 min *p(reactor)=200 mbar*
Group II On Si(113), Si(114), Si(116) MD5796	T=720 °C, TMAl-*p=800 mbar,* TMAl-flow =*100 sccm,* *d=~ 4 nm, t=15 s,* *p(reactor)=100 mba*r	HT-GaN / LT-AlN (~ 160 nm/~ 8 nm) $T_{(GaN)}$=1120°C, $T_{(AlN)}$=630 °C	T=1120 °C, d=~600 nm, t=15 min *p(reactor)=200 mbar*
Group III On Si(112), Si(113), Si(115) MD5818	T=720 °C, TMAl-*p=800 mbar* TMAl-flow =*100 sccm,* *d=~ 4 nm, t=15 s,* *p(reactor)=100 mbar*	AlGaN=5 min T=1120 °C	T=1080 °C, d=~2 μm, t=50 min *p(reactor)=200 mbar* *+(~8nm)LT-AlN interlayer*

Table 4: *Growth parameters*

Samples	AlN seeding layer	Next layer	GaN layer
Series ι MD6437,MD6434, MD6435, MD6436 on Si(112) and Si(113)	T=720 °C, TMAl-*p=1000 mbar* TMAl-flow=*20 sccm,* *p(reactor)=100 mbar* *Thickness (from 1 bis 10 min) related to growth time (4 bis 40 nm)*	HT-GaN / LT-AlN (~ 160 nm/~ 8 nm) $T_{(GaN)}$=1120°C, $T_{(AlN)}$=630 °C	T=1145 °C, d=~600 nm, t=15 min *p(reactor)=200 mbar*

Table 5: *Growth parameters*

Samples	AlN seeding layer	Next layer	GaN layer	LT-AlN interlayer	GaN layer
MD5818 on Si(112), and Si(113)	T=720 °C, d=~ 4 nm, t=15 s, TMAl-p=800 mbar TMAl-flow=100 sccm, $p_{(reactor)}$=100 mbar	AlGaN d=~ 60 nm, t=5 min T= 1120°C,	T=1080 °C, d=~800 nm, t=20 min $p_{(reactor)}$=200 mbar	T=650 °C d=~ 8 nm, t=2 min,	T=1080 °C, d=~1200 nm, t=30 min $p_{(reactor)}$=200 mbar
MD6677 on Si(113)	T=710 °C, d=~ 12 nm, t=3 min, TMAl-p=1000 mbar TMAl-flow=20 sccm, $p_{(reactor)}$=100 mbar	AlGaN d=~ 60 nm, t=5 min T= 1150°C, $p_{(reactor)}$=70 mbar	T=1140 °C, d=~1600 nm, t=20 min $p_{(reactor)}$=200 mbar carrier gas=H_2	T=900 °C d=~8nm, t=2 min,	T=1080 °C, d=~1300 nm, t=2 h $p_{(reactor)}$=200 mbar carrier gas=N_2

Publications

Parts of this thesis have already been published:

Literature contributions

R. Ravash, A. Dadgar, F. Bertram, A. Dempewolf, S. Metzner, T. Hempel, J. Christen, and A. Krost, *MOVPE growth of semi-polar GaN light-emitting diode structures on planar Si(112) and Si(113) substrates*, Journal of Crystal Growth (2012).

R. Ravash, P. Veit, A. Dadgar, M. Müller, A. Dempewolf, T. Hempel, J. Christen, and A. Krost, *Growth and stacking fault reduction in semi-polar GaN films on planar Si(112) and Si(113)*, Phys. Status Solidi C **9**, 507 (2012).

A. Dadgar, R. Ravash, P. Veit, G. Schmidt, M. Müller, A. Dempewolf, F. Bertram, M. Wieneke, J. Christen, and A. Krost, *Eliminating stacking faults in semi-polar GaN by AlN interlayers,* Appl. Phys. Lett. **99**, 021905 (2011).

R. Ravash, J. Bläsing, T. Hempel, M. Noltemeyer, A. Dadgar, J. Christen, and A. Krost, *Impact of AlN seeding layer growth rate in MOVPE growth of semi-polar gallium nitride structures on high index silicon,* Phys. Status Solidi B **248**, No. 3, 594–599 (2011).

R. Ravash, J. Blaesing, A. Dadgar, and A. Krost, *Semipolar single component GaN on planar high index Si(11h) substrates,* Appl. Phys. Lett. **97**, 142102 (2010).

R. Ravash, J. Bläsing, M. Noltemeyer, T. Hempel, A. Dadgar, J. Christen, and A. Krost, *Metal organic vapor phase epitaxy growth of single crystalline GaN on planar Si(211) substrates,* Appl. Phys. Lett. **95**, 242101 (2009).

Patents

DE 10 2009 042 349, R. Ravash, A. Dadgar, A. Krost, *Semipolar wurtzitische Gruppe-III-Nitrid basierte Halbleiterschichten und darauf basierende Halbleiterbauelemente* (2009).

DE 10 2011 011 043.7, A. Dadgar, A. Krost, P. Veit, R. Ravash, *Halbleiterschicht oderHalbleiterschichtsystem mit einer semipolaren oder m-planaren Gruppe-III-Nitrid Schicht* (2011).

Conference presentations

R. Ravash, A. Dadgar, A. Dempewolf, P. Veit, T. Hempel, J.Bläsing, J. Christen, and A. Krost, *MOVPE growth of semi-polar GaN LED structures on planar Si(112) and Si(113),* ICMOVPE, Busan, Korea, 20-25 May (2012).

R. Ravash, A. Dadgar, A. Dempewolf, P. Veit, T. Hempel, J.Bläsing, J. Christen, and A. Krost, *MOVPE growth of semi-polar GaN LED structures on planar Si(112) and Si(113) substrates*, *DPG Spring Meeting, Berin, Germany, 25-30 March (2012).*

J. Christen**,** F. Bertram, G. Schmidt**,** S. Petzold, P. Veit, R. Ravash, A. Dadgar, and A. Krost, *Cathodoluminescence directly performed in a transmission electron microscope: nanoscale correlation of structural and optical properties,* Microscopy & Microanalysis July 29 - August 2 (2012).

R. Ravash, P. Veit, G. Schmidt, M Müller, A. Dadgar, A. Dempewolf, T. Hempel, J. Bläsing, F. Bertram, J. Christen, and A. Krost, *Reduction of stacking faults in semi-polar GaN grown on planar Si(112) and Si(113) substrates by AlN interlayers*, DGKK, Stuttgard, Germany, 8-9 December (2011).

R. Ravash, P. Veit, G. Schmidt, T. Hempel, M. Müller, A. Dempewolf, F. Bertram, A. Dadgar, J. Bläsing, J. Christen, and A. Krost, *Eliminating stacking faults in semi-polar GaN grown on planar Si(112) and Si(113) substrates by AlN interlayers,* MRS-fall Meeting, Boston, MA,USA, November 28-December 02 (2011).

F. Bertram, G. Schmidt, S. Petzold, P. Veit, R. Ravash, A. Dadgar, A. Krost, and
J. Christen, *Cathodoluminescence directly performed in a transmission electron microscope: nanoscale correlation of structural and optical properties* Microscopy Conference, Kiel, Germany, August 28-September 02 (2011).

A. Dadgar, R. Ravash, P. Veit, G. Schmidt, M. Müller, A. Dempewolf, F. Bertram,
J. Christen, and A. Krost, *Stacking fault elimination in semipolar GaN on Si(112) by LT-AlN interlayers,* SIMC-16,Stockholm, Sweden (2011).

F. Bertram, G. Schmidt, A. Dempewolf, S. Petzold, P. Veit, R. Ravash, A. Dadgar, A. Krost, and J. Christen, *Efficient termination of basal plane stacking faults by a low-temperature AlN interlayer in GaN on Si(211)substrate by (S)TEM-CL,* 9th International Conference on Nitride Semiconductors, ICNS-9, SECC, Glasgow, UK, 10-15 July (2011).

R. Ravash, P. Veit, G. Schmidt, T. Hempel, M. Müller, A. Dempewolf, F. Bertram, A. Dadgar, J. Bläsing, J. Christen, and A. Krost, *Reducing stacking faults in semi-polar GaN layers grown on planar Si(112) substrates,* 9th International Conference on Nitride Semiconductors, ICNS-9, SECC, Glasgow, UK, 10-15 July (2011).

R. Ravash, J. Bläsing, T. Hempel, A. Dadgar, and A. Krost**,** *Impact of the AlN seeding layer growth conditions on semi-polar GaN crystalline properties grown on Si (11h),* XIV-European Workshop on Metalorganic Vapor Phase Epitaxy (EW-MOVPE), Wrocław, Poland, 5-8 June (2011).

R. Ravash, J. Bläsing, A. Dadgar, J. Christen, A. Krost, *MOVPE growth of semi-polar GaN on planar Si(11h) substrates,* EMRS, Nice, France 9-13 May (2011).

R. Ravash, J. Bläsing, A. Dadgar, J. Christen, and A. Krost, *MOVPE-growth of semipolar GaN on planar Si(h11) substrate,* DPG Spring Meeting, Dresden, Germany 13-18 March (2011).

M. Müller, A. Dempewolf, F. Bertram, T. Hempel, J. Christen, R. Ravash, A. Dadgar and A. Krost*, Kathodolumineszenzuntersuchungen an GaN auf Si(211)-und Si(311)-Substraten,* DPG Spring Meeting, Dresden, Germany, 13-18 March (2011).

G. Schmidt, B. Bastek, P. Veit, F. Bertram, R. Ravash, and J. Christen, *Liquid He Temperature Cathodoluminescence Spectroscopy in a Scanning Transmission Electron Microscop*, DPG Spring Meeting. Dresden, Germany, 13-18 March (2011).

R. Ravash, J.Bläsing, A. Dadgar, und A. Krost, *Wachstum von semipolar GaN auf hochindizierten Si(11h) Substraten,* 25. DGKK Meeting, Aachen, Germany, 9-10 December (2010).

R. Ravash, J. Bläsing, A. Dadgar, T. Hempel, P. Veit, J. Christen, A. Krost, *MOVPE growth of semipolar GaN on planar Si(11h) applying LT-AlN seeding layer*, PolarCoN Summer School, Schloss Reisensburg, Günzburg, Germany, 12-14 October (2010).

R. Ravash, J. Bläsing, A. Dadgar, T. Hempel, J. Christen, and A. Krost, *Impact of the AlN seeding layer growth parameters on semipolar GaN on Si(112),* International Workshop on Nitride Semiconductors (IWN), Tampa, Florida, *USA,* 19-24 September (2010)*.*

A. Dempewolf, M. Müller, F. Bertram, T. Hempel, R. Ravash, A. Dadgar, and A. Krost, J. Christen, *Luminescence properties of GaN grown on Si(211) and Si(311) by MOVPE,* International Workshop on Nitride semiconductors IWN, Tampa, USA, 19-24 September (2010) (Poster).

R. Ravash, A. Dadgar, J. Bläsing, and A. Krost, *Semi-polar growth of single crystalline GaN on Si(11h),* International Nano-Optoelectronic Workshop (inow), Peking und Changchun, China, 30.07.-14.08(2010) (Poster).

R. Ravash, J. Bläsing, A. Dadgar, T. Hempel, J. Christen, and A. Krost, *MOVPE-growth of semipolar GaN on high index Si substrate,*.15th International Conference on Metal Organic Vapor Phase Epitaxy, Lake Tahoe, Nevada, USA, 23-28 May (2010).

R. Ravash, J. Bläsing, A. Dadgar, T. Hempel, P. Veit, J. Christen, and A. Krost, *MOVPE-growth of semipolar GaN on Si(211) substrate*, DPG Spring Meeting, Regensburg, Germany, 21-26 March (2010).

R. Ravash, J. Bläsing, A. Dadgar, T. Hempel, P. Veit, A. Krost, *MOVPE-growth of semi-polar GaN on Si(711) and Si(100), 4.5° off substrates,* 24. DGKK Meeting, Jerusalemskirche in Berlin, Germany, 10-11 December (2009).

R. Ravash, J. Bläsing, A. Dadgar, T. Hempel, J. Christen, A. Krost, *MOVPE grown GaN on (711)- and (410)-Si substrates*, International Nano-Optoelectronic Workshop(inow) Stockholm, Sweden, Berlin, Germany, 2-15 August (2009) (Poster).

R. Ravash, J. Bläsing, T. Hempel, J. Christen, A. Dadgar, and A. Krost, *MOVPE growth of GaN on high index Si-substrates,* European Workshop on Metalorganic Vapor Phase Epitaxy (EWMOVPE), Ulm, Germany, 07-10 June (2009) (Poster).

R. Ravash, J. Bläsing, A. Dadgar, and A. Krost, *MOVPE Wachstum von GaN auf hochindizierten Silizium-Substraten,* DPG Spring Meeting, Dresden, Germany, 22-27 March (2009).

R. Ravash, J. Bläsing, M. Wieneke, A. Dadgar, and A. Krost, *Wachstum von GaN auf hochindizierten Silizium-Substraten,* 23. DGKK Meeting, Braunschweig, Germany, 04-05 December (2008):

Curriculum Vitae

Personal data

Family name	Ravash
First name	Roghaiyeh
Date of birth	1st September, 1975
Place of birth	Oromiyeh (Iran)
Nationality	German / Iranian
Correspondece address	Karl-Marx-Allee 70 f
	10243, Berlin
	Telefon: +49-30 76745692,
	Mobil: +49-176 62219469,
	E-Mail: Ravash_r@yahoo.com

Education

13.02.2014	Defense of my Dissetation
Since 04.2008	PHD-student, Otto-von-Guericke-Universität Magdeburg, Semiconductor Epitaxy Department, Prof. Krost
09.2004 – 12.2007	University of Regensburg, Regensburg, Germany Academic degree: Diploma-physics (grade=1.3) thesis „Terahertz photocurrents in density modulated electron gases"
09.2003 – 07.2004	German course, University of Regensburg, Regensburg, Germany Academic degree: DSH
01.03.2003	Entered Germany with my family
17.7.2000	Birth of my daughter
09.1994 – 09.1998	University of Uromiyeh, Oromiyeh, Iran Academic degree: Bachelor
06.1993	High school diploma, Oromiyeh, Iran Mathematics and Physics

Work experience

04.2008 – 11.2012	Research assistant, Otto-von-Guericke-Universität Magdeburg, Semiconductor Epitaxy Department, Prof. Krost
01.2008 – 03.2008	Research assistant, University of Regensburg, Semiconducting Nanostructures Department, Prof. Weiss
01.2005 – 12.2007	Student assistant, University of Regensburg
03.1999 – 12.1999	Advisor in a high school

Dipl.-Phys. Roghaiyeh Ravash

Karl-Marx-Allee 70F

10243 Berlin

Erklärung

Hiermit erkläre ich, dass ich die von mir eingereichte Dissertation zu dem Thema

Growth of semi-polar GaN on high index silicon (11h) substrates by metal organic vapor phase epitaxy

Selbstständig verfasst, nicht schon als Dissertation verwendet habe und die benutzten Hilfsmittel und Quellen vollständig angegeben wurden.

Weiterhin erkläre, dass ich weder diese noch eine andere Arbeit zur Erlangung des akademischen Grades doctor rerum naturalium (Dr. rer. nat.) an anderen Einrichtungen eingereicht habe.

Dipl.-Phys. Roghaiyeh Ravash

Berlin, den 29.09.2013